

## AN ABSTRACT OF THE DISSERTATION OF

Shawn R. Decker for the degree of Doctor of Philosophy in Chemistry presented on June 15, 2017.

Title: On the Properties and Characteristics of Solution Processed Hafnium Based Thin-Films from Aqueous Precursors

Abstract approved: \_\_\_\_\_

Douglas A. Keszler

Aqueous hydroxo Hf nanoclusters enable studies to identify and codify steps in the deposition of Hf-based oxide thin films from solution precursors.  $\text{HfOCl}_2$  reacts with combinations of  $\text{H}_2\text{O}_2(\text{aq})$ , acids, and TMAH to produce polymetal species at high pH and low pH. X-ray scattering and spectroscopic methods reveal the nature of these species in solution, while temperature-programmed desorption coupled with a suite spectroscopic techniques detail their chemical changes as they transition to condensed thin films. Three precursors were studied in this work:

- hafnium peroxide hydroxide nitrate  $\text{Hf}(\text{O}_2)_{0.5}(\text{OH})_{1.8}(\text{NO}_3)_{1.2}$  (HafNO<sub>x</sub>)
- the photoresist  $\text{Hf}(\text{O}_2)_{0.5}(\text{OH})_{1.6}(\text{SO}_4)_{0.7}$  (HafSO<sub>x</sub>)
- the hexameric cluster  $((\text{CH}_3)_4\text{N})_6\text{Hf}_6(\text{O}_2)_6(\text{OH})_{18}$  (TMAHfO<sub>x</sub>).

©Copyright by Shawn R. Decker

June 15, 2017

All Rights Reserved

On the Properties and Characteristics of Solution Processed Hafnium Based Thin Films  
from Aqueous Precursors

by

Shawn R. Decker

A DISSERTATION

submitted to

Oregon State University

in partial fulfillment of  
the requirements for the  
degree of

Doctor of Philosophy

Presented June 15,2017

Commencement June 2017

Doctor of Philosophy dissertation of Shawn R. Decker presented on June 15, 2017

APPROVED:

---

Major Professor, representing Chemistry

---

Chair of the Department of Chemistry

---

Dean of the Graduate School

I understand that my dissertation will become part of the permanent collection of Oregon State University libraries. My signature below authorizes release of my dissertation to any reader upon request.

---

Shawn R. Decker, Author

## ACKNOWLEDGMENTS

First and foremost I want to acknowledge my wonderful wife Heather and our two boys Gabe and James. Their love, support, patience and understanding during these years was greatly needed and words cannot express my gratitude. You keep me grounded, you keep me sane, and you remind me of what is truly important in the world.

Next I would like to express my deepest thanks to the professors of Oregon State University. Their willingness to help me grow and guide me through this journey was instrumental in my growth as a student and a professional. I would like to thank Professor Doug Keszler especially for his patience and guidance through the years. The opportunities and professional as well as academic development that he has provided have helped to shape many aspects of my outlook on science and the importance of collaborative research in the world. I would also like to thank Professors May Nyman, Michelle Dolgos, and Paul Cheong whose guidance and feedback on a wide array of matters helped me to gain a more balanced perspective in countless matters.

Thank you to the many friends, colleagues and collaborators that have been a part of my graduate school experience. Without you all this would have been an insurmountable task. Josh Flynn and Lyndsay Wills especially for all the late study sessions and continued discussion of research over meals, or drinks. I also must thank the Keszler research group both past and present Ryan Mansergh, Deok Hie Park, Vasily Gouliouk, Jenn Amador, and Alan Telecky. Your willingness to discuss ideas and give feedback and perspective is greatly appreciated.

## ACKNOWLEDGMENTS (CONTINUED)

I also want to acknowledge the support of my friend and mentor Dr. Cory Perkins. Without you many of these projects would not have come to fruition. I thank you.

I would also like to acknowledge the Center for Sustainable Materials Chemistry for funding this work during these last years and providing an avenue of professional development that, I feel, is unmatched in any other doctoral program. The resources and people that make the center possible have my deepest gratitude, specifically the efforts of Dr. Bettye Maddux, Sharron Betterton, and Amanda Polley.

And my deepest thank you to the OSU Electron Microscopy facility and Teresa Sawyer and Pete Eschbach. The training and assistance that you provided were absolutely instrumental during my time here.

Finally I want to acknowledge the support of my parents Vic and Patricia, and my brothers Troy and Josh and my sister Melanie and Danylle as well as their spouses and gaggles of children. I also must acknowledge my two brothers from another mother Justin and Patrick. You guys have been there for me in some of my hardest times and helped me in more ways than you can possibly know.

For all of those acknowledged here and the host of others that I couldn't begin to name, thank you.

## CONTRIBUTION OF AUTHORS

As the nature of this effort has been extremely collaborative, there are many others who have contributed to this body of work. Deok Hie Park collected TPD and TGA Mass Spec that appears in chapters 2, 3, and 5 and aided in the interpretation of these data. Aaron Dangerfield and Charith Nanayakkara under the tutelage of Yves Chabal at UT Dallas collected thin –film FTIR in chapters 2 and 5 respectively. Dr. Cory Perkins collected IR data appearing in chapter 2 and facilitated a collaborative environment and provided significant intellectual contributions to the work in Chapter 5. Daniel Huchison under the guidance of Professor May Nyman collected SAXS data in chapter 3. Ryan Mansergh prepared samples for and gathered TEM images in chapter 5. Dr. John Donovan at University of Oregon aided in prepping gathering and interpreting EPMA data at the CAMCOR facility. Jenn Amador collected Raman spectroscopy data for chapters 6 and 8. Richard Oleksak under the instruction of Professor Greg Herman collected TEM and STEM EDS for chapter 7 and 8. Feixiang Luo with Professor Rick Garfunkel at Rutgers University collected XPS in chapters 7 and 8. Milton Jackson collected DLS for chapter 8. Rose Ruther collected QCM and AFM in chapter 8. Professor Doug Keszler suggested a great deal of the experiments and provided guidance and feedback on the interpretation of experimental data and facilitated a collaborative and multidisciplinary effort.

## TABLE OF CONTENTS

	<u>Page</u>
Chapter 1: Introduction.....	1
References.....	4
Chapter 2: Annealing and Atmosphere Effect on the Decomposition of Hafnium Peroxide Hydroxide Nitrates: A Thin Film Study.....	5
Abstract.....	6
Introduction.....	7
Results and Discussion.....	8
Thermal Gravimetric Analysis.....	8
ATR on Bulk Powder.....	11
Difference Infrared Spectroscopy.....	11
TPD-MS; Films Annealed in Air.....	16
Argon Annealing.....	26
Pure Oxygen Annealing.....	29
Neutralization and Steam Annealing.....	29
Conclusions.....	38
Methods.....	38
Solution and Sample Prep.....	38
Thermogravimetric Analysis.....	39
ATR Analysis.....	39
FTIR Analysis.....	39
Temperature Programmed Desorption.....	40
References.....	41

## TABLE OF CONTENTS (Continued)

	<u>Page</u>
Chapter 3: Hafnia Films from an Alkaline Precursor.....	42
Introduction.....	42
Results and Discussion.....	42
Solution Characterization.....	42
Small Angle X-ray Scattering.....	44
Film Characterization.....	47
Temperature Programmed Desorption.....	49
Methods.....	52
Solution Synthesis.....	52
Film Synthesis.....	54
Small Angle X-ray Scattering.....	54
Film Characterization.....	54
Temperature Programmed Desorption.....	55
Conclusions.....	55
References.....	56
 Chapter 4: Addition of M <sup>3+</sup> and M <sup>4+</sup> Cations to Aqueous Hafnia Precursors.	 57
Introduction.....	57
Results and Discussion.....	57
Electron Probe Microanalysis.....	57
Yttrium in HafNO <sub>x</sub> .....	60
Aluminum in HafNO <sub>x</sub> .....	62
Silicon in TMA Hafnia Precursor.....	65
Germanium in TMA Hafnia Precursor.....	68

## TABLE OF CONTENTS (Continued)

	<u>Page</u>
Methods.....	68
Precursor Synthesis.....	68
Film Synthesis.....	70
Electron Probe Microanalysis.....	70
Grazing incidence X-ray Diffraction.....	71
Conclusions.....	71
References.....	72
Chapter 5:    Aqueous Processes to Limit Hydration of Thin-Film Inorganic Dielectrics.....	73
Abstract.....	74
Introduction.....	75
Results and Discussion.....	76
AlPO Dehydration.....	76
AlPO Rehydration.....	83
In-Situ Transmission Electron Microscopy.....	88
Conclusions.....	91
Experimental Section.....	92
References.....	96
Chapter 6:    Patterning Chemistry of HafSO <sub>x</sub> .....	97
Abstract.....	98
Introduction.....	99
Methodology.....	100
ICP-OES.....	100

## TABLE OF CONTENTS (Continued)

	<u>Page</u>
Titration.....	101
Raman Measurements.....	101
Results and Discussion.....	102
Conclusions.....	105
References.....	109
Chapter 7: Chemical and Structural Investigation of High-Resolution	
Patterning with HafSO <sub>x</sub> .....	110
Abstract.....	111
Introduction.....	112
Experimental.....	114
Results and Discussion.....	115
Conclusions.....	123
References.....	124
Chapter 8: Patterning Mechanisms of Hafnium Polyoxometalate Thin Films	126
Abstract.....	127
Introduction.....	128
Experimental.....	131
Solution Precursor Preparation.....	131
Film Deposition.....	131
Dynamic Light Scattering (DLS).....	132
Microscopy.....	132
Raman Spectroscopy.....	132

## TABLE OF CONTENTS (Continued)

	<u>Page</u>
Quartz Crystal Microbalance.....	133
X-ray Photoelectron Spectroscopy (XPS).....	133
Peroxide Analysis.....	133
Results and Discussion.....	134
Conclusions.....	146
References.....	147
Conclusions.....	150
Bibliography.....	151
Appendix.....	159

## LIST OF FIGURES

<u>Figure</u>	<u>Page</u>
2.1 TGA-TDA-MS data collected on ground glass from hafnia precursor....	8
2.2 ATR data for bulk $\text{HafNO}_x$ .....	12
2.3 In situ difference FTIR data for an as deposited film referenced to blank substrate.....	13
2.4 In situ difference FTIR data for an as deposited film referenced to as deposited film.....	14
2.5 In situ difference FTIR data for an as deposited film referenced to previous spectra.....	15
2.6 TPD-MS response for mass 30, $\text{NO}_{(g)}$ .....	17
2.7 XRD for films annealed at various ramp rates.....	19
2.8 TPD-MS response for mass 32 $\text{O}_2$ .....	21
2.9 TPD mass response corresponding to water for films annealed in air.....	23
2.10 Peak fitting analysis for mass 18 TPD spectra on film annealed for 1 hour at 250 °C.....	25

## LIST OF FIGURES (Continued)

<u>Figure</u>	<u>Page</u>
2.11 TPD-MS response for mass 30 NO <sub>(g)</sub> from films annealed in argon .....	27
2.12 TPD-MS response for mass 18 water from films annealed in argon .....	28
2.13 TPD-MS response for mass 32 O <sub>2(g)</sub> from films annealed in argon .....	30
2.14 TPD-MS data for films annealed in pure oxygen.....	31
2.15 TPD-MS data for neutralized films.....	33
2.16 TPD-MS data for films annealed in steam.....	34
2.17 Integrated TPD data showing residual nitrate.....	36
2.18 Integrated TPD data showing residual water.....	37
3.1 Pourbaix diagram for hafnium in water.....	43
3.2 SAXS data for high pH hafnia solutions.....	45
3.3 SAXS data for aged high pH hafnia solution.....	46
3.4 Thin film XRD on films made from TMA Hf precursor heated to various temperatures.....	48

## LIST OF FIGURES (Continued)

<u>Figure</u>		<u>Page</u>
3.5	TPD showing water (mass 18) loss as a function of temperature.....	50
3.6	TPD response for the decomposition products of TMAH.....	51
3.7	TPD data showing the decomposition products of TMAH in the presence of chloride.....	53
4.1	Unit cells for the four known phases of hafnium oxide.....	58
4.2	XRD of various Y:HfO <sub>2</sub> compositions heated to 500 °C.....	61
4.3	XRD of 7% Al:HfO <sub>2</sub> thin films heated to various temperatures.....	63
4.4	XRD of 10% Al:HfO <sub>2</sub> thin films heated to various temperatures.....	64
4.5	XRD of 7% Si:HfO <sub>2</sub> thin films heated to various temperatures.....	66
4.6	XRD of 10% Si:HfO <sub>2</sub> thin films heated to various temperatures.....	67
4.7	XRD of 10% Ge:HfO <sub>2</sub> thin films heated to various temperatures.....	69
5.1	TEM micrograph of AlPO-HfO <sub>2</sub> bilayer heated to 550 °C.....	77

## LIST OF FIGURES (Continued)

<u>Figure</u>	<u>Page</u>
5.2 FTIR absorption spectra for 120-nm AlPO, 20-nm HfO <sub>2</sub> , and 20-nm HfO <sub>2</sub> -capped 120-nm AlPO films after stepwise annealing to 350 °C.....	78
5.3 H <sub>2</sub> O TPD spectra for AlPO and HfO <sub>2</sub> -AlPO thin films.....	81
5.4 FTIR difference spectra between 80 and 350 °C for HfO <sub>2</sub> capped films...	82
5.5 H <sub>2</sub> O TPD spectra for AlPO and HfO <sub>2</sub> -capped AlPO thin films after heating to 550 °C, then resting in air for 25 days.....	85
5.6 H <sub>2</sub> O TPD spectra for a 1- $\mu$ m AlPO film capped by an 11-nm HfO <sub>2</sub> layer..	87
5.7 In-situ heated TEM micrographs of a 143-nm AlPO film capped by 31 nm of HfO <sub>2</sub> .....	89
5.8 TEM micrographs of 140-nm AlPO film capped by 11-nm HfO <sub>2</sub> films..	90
6.1 Raman spectra of HafSO <sub>x</sub> solutions with selected O <sub>2</sub> <sup>2-</sup> :Hf ratios.....	104
6.2 Raman spectra for HafSO <sub>x</sub> films after exposure with a 30-kV electron Beam.....	106

## LIST OF FIGURES (Continued)

<u>Figure</u>	<u>Page</u>
6.3 Raman signal as a function of electron-beam exposure dose and Solubility characteristics.....	107
7.1 Cross-sectional TEM images of unexposed HafSO <sub>x</sub> film annealed at 300 °C and STEM-EDS line scan.....	116
7.2 TEM cross sectional images of HafSO <sub>x</sub> film exposed at 800 μC/cm <sup>2</sup> , soaked in 25% TMAH, and hard baked at 300 °C and STEM-EDS line scan.....	118
7.3 Hf 4f, O 1s, and S 2p XPS spectra of HafSO <sub>x</sub> films under selected process conditions.....	119
7.4 TEM cross sectional image of an electron-beam patterned HafSO <sub>x</sub> film after 800 μC/cm <sup>2</sup> exposure and development in 25% TMAH, HR-TEM image of single line and fast Fourier transform.....	121
8.1 (a) Structure of hafnium tetramer. (b) DLS size analysis for a 150 mM HafSO <sub>x</sub> solution as a function of solution age. (c) TEM image of hafnium sulfate clusters. (d) Cross-sectional TEM image of a spin-coated HafSO <sub>x</sub> film.....	130
8.2 Raman spectra of hydrogen peroxide, sulfuric acid, the HafSO <sub>x</sub> precursor solution, and HafSO <sub>x</sub> films made with and without peroxide.....	136

## LIST OF FIGURES (Continued)

<u>Figure</u>	<u>Page</u>
8.3 Selected XPS O1s spectra of a HafSO <sub>x</sub> .....	139
8.4 QCM measurements of the dissolution of HafSO <sub>x</sub> .....	141
8.5 SEM images of contrast arrays generated by patterning films with Increasing electron beam exposure doses and contrast curve generated from AFM.....	143
S1 FTIR difference spectra obtained for as-synthesized AlPO film after annealing to 150 °C.....	159
S2 FTIR difference spectra obtained for a 120 nm AlPO film, after annealing to 350 °C.....	161
S3 FTIR difference spectra obtained for 20 nm HfO <sub>2</sub> -capped 120 nm AlPO film, after annealing to 350 °C.....	162
S4 FTIR difference spectra of 82 nm AlPO, after stepwise annealing to 350 °C.....	163
S5 Integrated area of bidentate phosphate gain for 82 nm AlPO film as a function of integrated area of OH/H <sub>2</sub> O loss.....	164

## LIST OF FIGURES (Continued)

<u>Figure</u>		<u>Page</u>
S6	TPD spectra for HfO <sub>2</sub> control experiments. Both the thick and thin HfO <sub>2</sub> film did not show signs of resorption after the 14 day period after being heated to 550 °C.....	165
S7	TPD data for each of the HfO <sub>2</sub> -capped AlPO films.....	166
S8	TPD data for water loss of AlPO films.....	167

## LIST OF TABLES

<u>Table</u>		<u>Page</u>
4.1	Mole fractions for solutions based on concentrations of precursors and films based on EPMA.....	59
5.1	Percent water remaining from integrated area analysis of each absorption spectra between 3740–3000 cm <sup>-1</sup> for each film.....	80
5.2	Increase in bidentate phosphate absorbance from bands at 1249 and 1101 cm <sup>-1</sup> .....	84
8.1	Normalized atomic percent of Hf, O, S for HafSO <sub>x</sub> films with increasing sulfate:Hf molar ratios from XPS analysis.....	145

## Chapter 1: Introduction

With ever increasing costs in both dollars and climate damage, the need for sustainable approaches to materials processing has never been greater, particularly in the thin films application. A number of methods have been appropriated to answer the demand in the form of spray coating and various techniques requiring solvated and aqueous precursors.[1–3] As this field grows and expands, the commonly used pourbaix diagram has served as a basal starting point. The problem arises when metals are complexed with various counter ions and pH and concentration effects cause oligomerization to occur.[4,5] Because of the high degree of control that is needed to create and process materials for modern applications, a keen understanding of these effects must be understood, and large gaps exist in the knowledge base.

As mentioned, the need for new precursory materials that extend beyond common solubility rules is desperately needed to fully utilize these new techniques. However, simple salt solutions do not always yield quality films. Though existing solution based precursors made using sol-gel methods can yield full coverage of a substrate, [6–17] the resulting films often have low density with respect to bulk material. This stems from the nature of sol-gel chemistry consisting of polydispersed nano-particles encapsulated by organic capping agents and surfactants.[18] Coupling this with the need to remove the capping agents, traditionally through thermal means, and the method leaves room for improvement.

Next generation aqueous precursors are synthesized using non stoichiometric ratios of metals and counter ions and precisely controlling pH to partially drive condensation in

solution to a self-regulating equilibrium by the formation of clusters such as polyoxometalates[19,20] or other such metal hydroxide clusters like the flat aluminum 13. [21,22] The synthesis of the flat Al 13 cluster has been noted as a function of pH and metal counter ion ratio alone, while others such as polyoxoniobate is synthesized by a reflux of a monomeric peroxy-niobate.[1] In this contribution, we focus on the behavior of hafnium in its most stable oxidation state.

Once a precursor compound is synthesized, an in-depth understanding of the chemistry regarding the journey from aqueous solution to gel and finally metal oxide film is essential if there is any hope to bring this technology to industry. For these precursors, small inorganic ligands such as peroxide, nitrate, and sulfate are used. Utilizing these ligands provides for an easy way to control pH, solubility and charge balance while being small enough and easy enough to remove either thermally or through ion exchange. The resulting condensation process for these precursors leads to smooth, high quality thin films.

In recent years, significant progress has been made in the synthesis of cluster based aqueous metal precursors. For this contribution the focus is understanding various chemistries for three systems, all of which are hafnium based. The first system developed by Kai Jiang [23] has been shown to make smooth, dense hafnium oxide films. What is not known about this system is the intricacies of the chemistry as we go from precursor to gel to oxide thin film. Chapter 2 of this work examines how this process occurs in oxygen and argon environments as well as the effect high humidity has on the process. Finally a neutralization process is examined as a potential aid alteration to the process. Chapter 3 investigates a new alkaline hafnia precursor based on the TMA hexameric hafnium cluster

first reported by Goberna-Feron. Chapter 4 will focus on the effects of incorporating various metal cations into these two solutions and the effect it has on the crystallization behavior. Chapter 5 will focus on one application for hafnium films as a capping layer and moisture barrier for non-stoichiometric aluminum phosphate thin films. Chapters 6-8 will focus on various aspects of the hafnium peroxide sulfate photoresist  $\text{HfSO}_x$ , and the chemical processes and characteristics of the material through synthesis and lithography.

Though this body of work primarily examines the fundamental chemistries associated with these precursors, there is potential for significant broader impacts. As basic science is fundamental for developing tools for other disciplines, this work has the potential to impact fields such as electrical engineering, material science, computer science and much more.

Since its discovery in 1923 and subsequent isolation in 1925, Hafnium has found an ever increasing use in varying applications. From control rods in nuclear reactors [24] to catalysts for polymerization [25] and insulators in electronics [26] as an oxide, the chemistry of hafnium has contributed to many of the technological advances of the last century. Coupling this with hafnium's low toxicity and an ever increasing demand for new materials and we have a very attractive candidate for the sustainability conscious mindset behind many of the scientific and industrial advancements being made today.

## References

- [1] Hou, Y.; Fast, D. B.; Ruther, R. E.; Amador, J. M.; Fullmer, L. B.; Decker, S. R.; Zakharov, L. N.; Dolgos, M. R.; Nyman, M. *J. Solid State Chem.* **2015**, *221*, 418–425.
- [2] Morris, J. E. **2012**, 1–27.
- [3] Murari, N. M.; Mansergh, R. H.; Huang, Y.; Kast, M. G.; Keszler, D. A.; Conley, J. F. *J. Mater. Res.* **2016**, *31*, 3303–3312.
- [4] Tang, H.; Xiao, F.; Wang, D. *Adv. Colloid Interface Sci.* **2015**, *226*, 78–85.
- [5] Rauwel, P.; Rauwel, E.; Persson, C.; Sunding, M. F.; Galeckas, A.; Rauwel, P.; Rauwel, E.; Persson, C.; Sunding, M. F.; Galeckas, A. **2014**, 104107.
- [6] Choi, J. H.; Mao, Y.; Chang, J. P. *Mater. Sci. Eng. R Reports* **2011**, *72*, 97–136.
- [7] Park, S. *Science (80-. )*. **2002**, *297*, 65–65.
- [8] Gálvez-barboza, S.; González, L. A.; Puente-urbina, B. A.; Saucedo-salazar, E. M.; García-cerda, L. A. **2015**, *643*, 62–66.
- [9] Kanazhevskii, V. V.; Kotsarenko, N. S.; Kolomiichuk, V. N. **2011**, *52*, 80–87.
- [10] Hu, M. Z.-C.; Harris, M. T.; Byers, C. H. *J. Colloid Interface Sci.* **1998**, *198*, 87–99.
- [11] Kakihana, M.; Kobayashi, M.; Tomita, K.; Petrykin, V. *Bull. Chem. Soc. Jpn.* **2010**, *83*, 1285–1308.
- [12] Southon, P.; Bartlett, J. *Chem. ...* **2002**, 4313–4319.
- [13] Zhang, F.; Liu, G.; Liu, A.; Shin, B.; Shan, F. *Ceram. Int.* **2015**, *41*, 13218–13223.
- [14] Henry, M.; Jolivet, J. P.; Livage, J. *Chem. Spectrosc. Appl. Sol-Gel Glas.* **1992**, *77*, 153–206.
- [15] Banger, K. K.; Yamashita, Y.; Mori, K.; Peterson, R. L.; Leedham, T.; Rickard, J.; Siringhaus, H. *Nat. Mater.* **2011**, *10*, 45–50.
- [16] Bartlett, J.; Woolfrey, J.; Percy, M. *J. Sol-Gel ...* **1994**, *220*, 215–220.
- [17] Tang, J.; Fabbri, J.; Robinson, R. *Chem. Mater.* **2004**, 1336–1342.
- [18] Danek, M.; Jensen, K. F.; Murray, C. B.; Bawendi, M. G. *Chem. Mater.* **1996**, *8*, 173–180.
- [19] Nyman, M.; Burns, P. C. *Chem. Soc. Rev.* **2012**, *41*, 7354.
- [20] Pope, M. T.; Müller, A. *Angew. Chem. Int. Ed. Engl.* **1991**, *30*, 34–48.
- [21] Wang, W.; Wentz, K.; Hayes, S. *Inorg. ...* **2011**, *13*, 9–11.
- [22] Wang, W.; Liu, W.; Chang, I.-Y.; Wills, L. A.; Zakharov, L. N.; Boettcher, S. W.; Cheong, P. H.-Y.; Fang, C.; Keszler, D. A. *Proc. Natl. Acad. Sci.* **2013**, *110*, 18397–18401.
- [23] Jiang, K.; Anderson, J. T.; Hoshino, K.; Li, D.; Wager, J. F.; Keszler, D. a. *Chem. Mater.* **2011**, *23*, 945–952.
- [24] Risovanyi, V. D.; Klochkov, E. P.; Varlashova, E. E. *At. Energy* **1996**, *81*, 764–769.
- [25] Heiland, K.; Kaminsky, W. *Makromol. Chem.* **1992**, *193*, 601–610.
- [26] Lin, Y. S.; Puthenkovilakam, R.; Chang, J. P. *Appl. Phys. Lett.* **2002**, *81*, 2041–2043.

## Chapter 2

### Annealing and Atmosphere Effect on the Decomposition of Hafnium Peroxide Hydroxide Nitrates: A Thin Film Study

**Shawn R. Decker**, Deok-Hie Park, Dylan B. Fast, Aaron Dangerfield, Cory Perkins  
Michelle Dolgos, Yves Chabal and Douglas A. Keszler

To be submitted for publication.

**Abstract**

The thermal decomposition and dehydration pathway for an aqueous hafnium hydroxo-peroxo-nitrate thin film precursor was studied in bulk and thin film forms under various atmospheric conditions. Nitrate is removed in most cases by 400 °C and residual water was found to persist in the films as hydroxide until between 350 and 450 °C depending on the annealing environment. The presence of water either as a neutralizing medium or in the form of high humidity or steam during annealing was found to greatly reduce the amount of residual nitrate present in the films.

## **Introduction**

This contribution covers the thermal decomposition profile and effect of ambient annealing environment on the decomposition and removal of nitrate and peroxide as well as the removal of water and hydroxide in hafnium oxide thin films made from nitrate containing aqueous precursor first reported by Jiang et al.[1] As this method has been shown to produce atomically smooth films with a density up to 86% of bulk, the processing temperature remains between 450 – 500 °C.[1] This takes the material out of the realm of low temperature processing which is commonly limited to 100 °C for some plastics.[2] Additionally, processing up to this temperature leaves a polycrystalline film. This may be less desirable for certain electronic applications such as a dielectric in a transistor as polycrystalline films tend to suffer from a higher leakage current and an amorphous film may be desirable.[3,4] Furthermore, understanding what the final barriers are that prevent realizing higher density films from this precursor is essential to creating better quality films that are necessary to broadening applications for this technique.

## **Results and Discussion**

### **Thermal Gravimetric Analysis**

Thermal Gravimetric Analysis Differential Thermal Analysis Mass Spectroscopy (TGA-DTA-MS) was conducted on bulk powder. [Figure 2.1a, 2.1b] These data show water loss occurring over the range of 30 to 475 °C. There are three local maxima at 120 °C, 155 °C and 325 °C. [Figure 2.1b] Oxygen is detected in 3 ranges from approximately 120-220 °C with a peak at 160 °C, 260-400 °C with a peak at approximately 335 °C, and

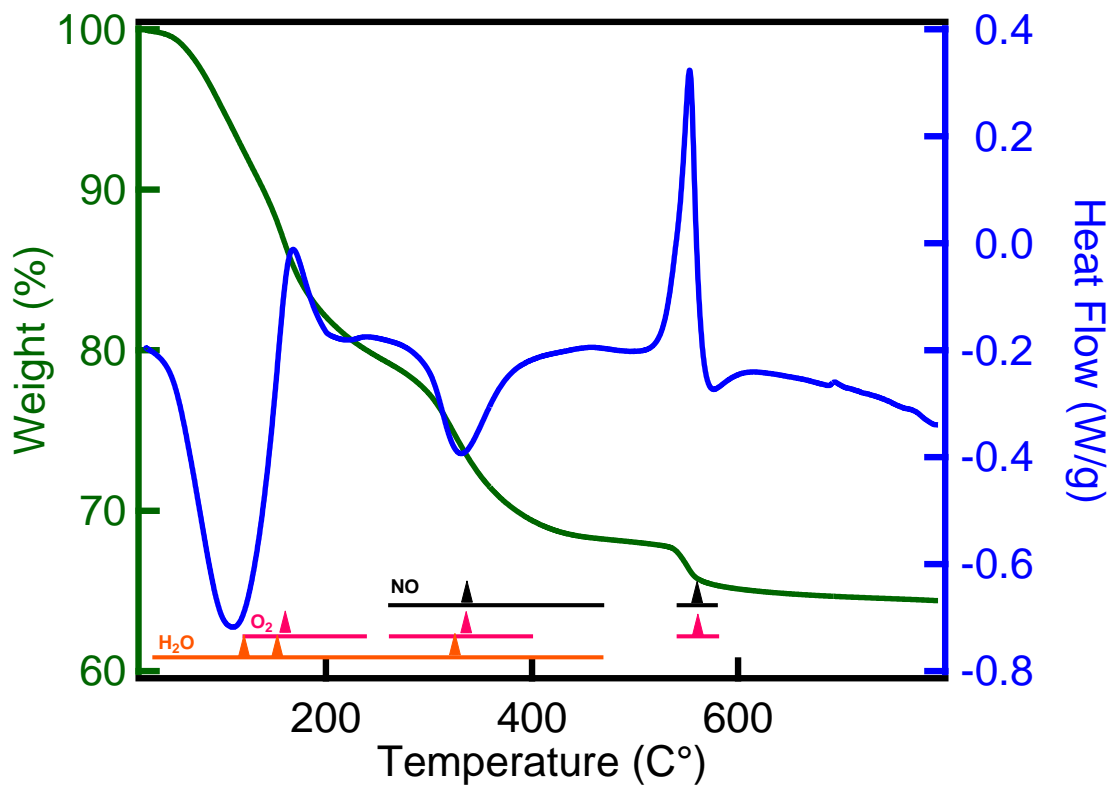


Figure 2.1a) TGA-TDA-MS data collected on ground glass from hafnia precursor. The green line depicts mass loss as a function of temperature. The blue line depicts heat flow. The orange, pink, and black lines represent the ranges where masses associated with water, oxygen gas, and nitric oxide gas were detected respectively. Arrows on the mass lines depict peaks or local maxima.

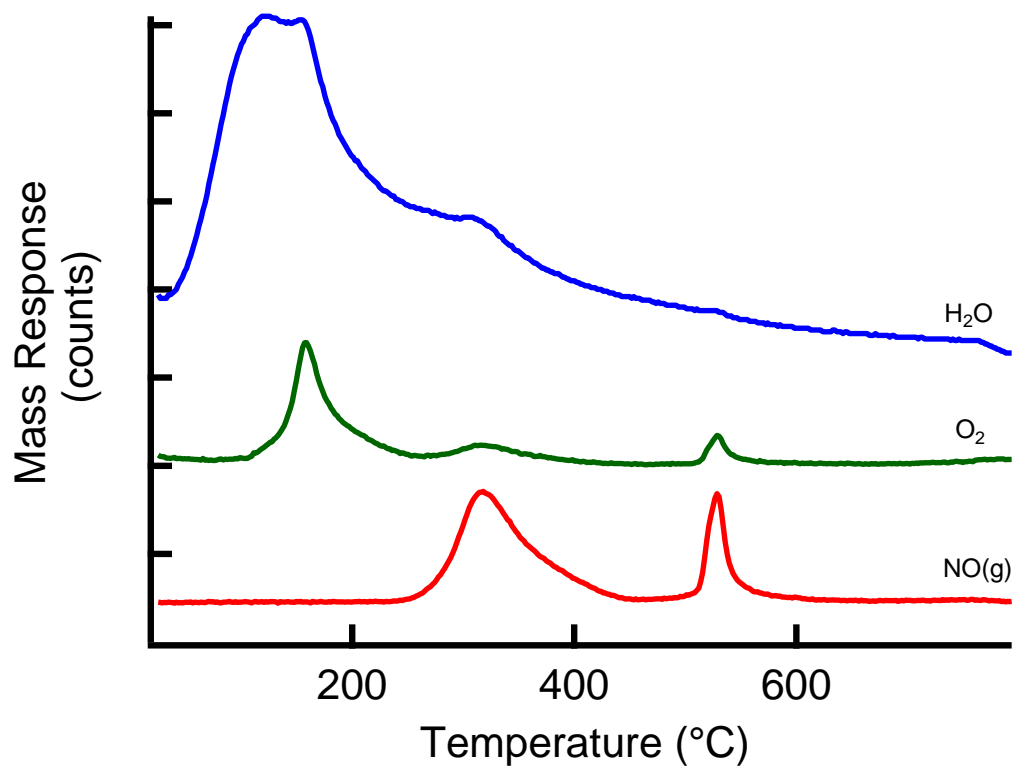


Figure 2.1b) raw mass spec data from TGA-MS for O<sub>2</sub> (green), NO (red) and H<sub>2</sub>O (blue)

540-580 °C with a peak at 560 °C. NO is detected as mass 30 in two ranges. The ranges are from 260-475 °C and 540-580 °C with peaks at 335 °C and 560 °C, respectively. The first range does encompass a previously reported decomposition temperature for  $\text{ZrO}(\text{NO}_3)_2$  which was reported to be 465 °C in air.[5]

The lower temperature region for water is associated with the loss of constitutional water. [Figure 2.1a] These water molecules comprise the inner and outer spheres of solvation for the hafnium species in the films, which likely contribute to network via hydrogen bonding. The higher temperature range for water loss is associated with the decomposition of hydroxides to form oxide and water. This reaction may occur more readily for hydroxides with an adjacent hydroxide, but less so for isolated hydroxides as such a reaction requires proton migration through the solid.

The first peak for the detection of oxygen is associated with the thermal decomposition of peroxide to form bridging oxides and  $\text{O}_2$  gas. The next two peaks correlate with the detection of NO gas. The nitrate breaks down to form oxygen gas and nitrogen dioxide which further decomposes to make nitric oxide and more oxygen.

The DTA data show an endothermic event occurs on initial heating followed by an exothermic event that peaks near 175 °C. The endothermic event is consistent with the evaporation of constitutional water, while the exothermic event overlaps peroxide decomposition, indicating that Hf – O bond formation associated with cluster crosslinking occurs. Next, a small endothermic event appears near 325 °C and a sharp exothermic event at 550 °C. The endothermic event is consistent with the loss of NO and  $\text{O}_2$  as nitrate decomposes. The final exothermic event is due to crystallization of the powder at 550 °C. A corresponding mass loss of NO and  $\text{O}_2$  are seen as crystallization occurs. This desorption

points to one of two possibilities, either a small amount of nitrate is persisting to this temperature and is preventing crystallization of the solid, or  $\text{NO}_{(\text{g})}$  is kinetically trapped. This gas escapes rapidly along grain boundaries once crystallization commences.

### **ATR on Bulk Powder**

Figure 2.2 shows transmission IR data collected on a non-heated bulk gel sample, a sample that had been heated to 450 °C for approximately 1 minute and the same heated sample after sitting in air for 4 days. The peaks near 1560, 1370 and 1300  $\text{cm}^{-1}$  are attributed to non-solvated bidentate nitrate, solvated nitrate, and non-solvated nitrate in the matrix respectively. This data shows that after heating rapidly and for a short period of time, as is seen in the TGA experiment, nitrate does persist in some capacity in the bulk sample above 450 °C. Furthermore, the spectra on the aged sample shows no changes relative to the non-aged heated sample indicating no detectable loss of trapped gasses dissipating over time. This observation tells us that the final barrier to crystallization upon heating at this high rate of temperature is residual nitrate persisting to higher temperatures.

### **Difference Infrared Spectroscopy**

In-situ IR conducted on films while heating monitors chemical changes in the film as a function of temperature. This technique allows for a comparison of collected spectra to a reference spectra of either a blank substrate, [Figure 2.3] an as deposited film, [Figure 2.4] or the previous spectra collected [Figure 2.5]. The spectra reveal absorption for nitrate at 1605, 1560, 1373, and 1305  $\text{cm}^{-1}$ . These frequencies are associated with non-solvated bridging nitrate, non-solvated bidentate nitrate, solvated nitrate, and non-solvated matrix nitrate, respectively. As films are heated, the peaks at 1605 and 1560  $\text{cm}^{-1}$  increase in intensity and blue shift to 1620 and 1584  $\text{cm}^{-1}$  respectively.[Figure 2.4 and 2.5] These

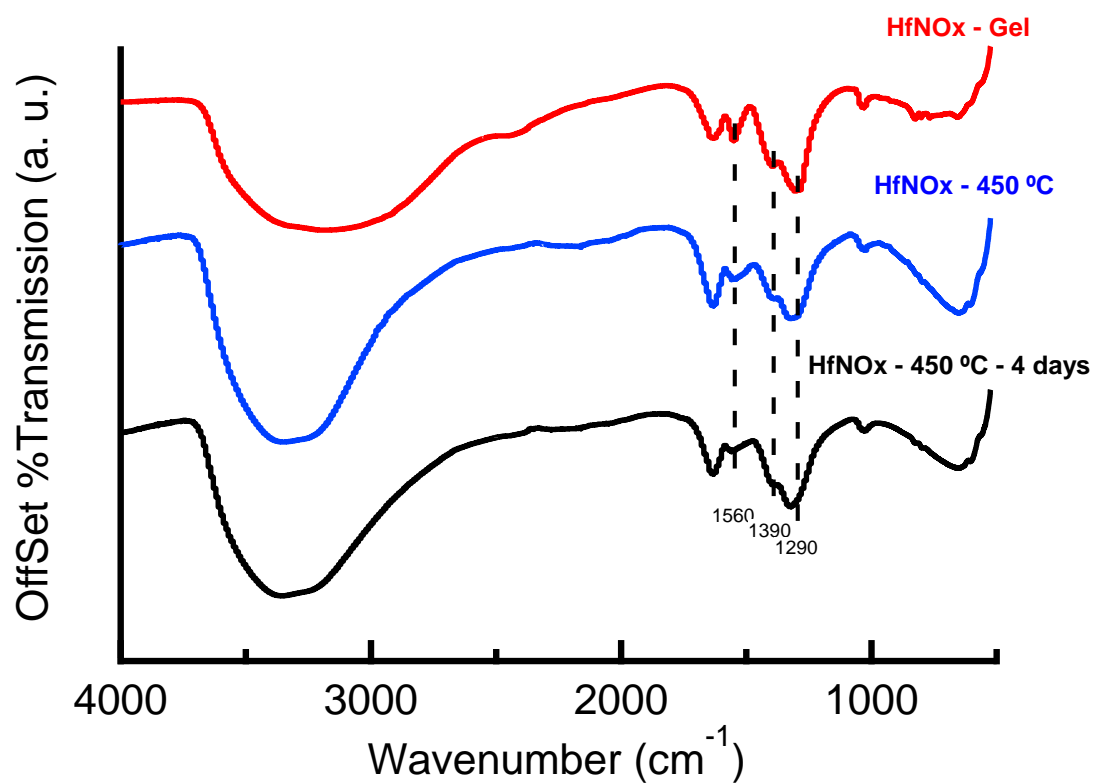


Figure 2.2: ATR data for bulk HafNO<sub>x</sub> gel (red) HafNO<sub>x</sub> gel heated to 450 °C (blue) and HafNO<sub>x</sub> gel heated to 450 °C and aged 4 days (black).

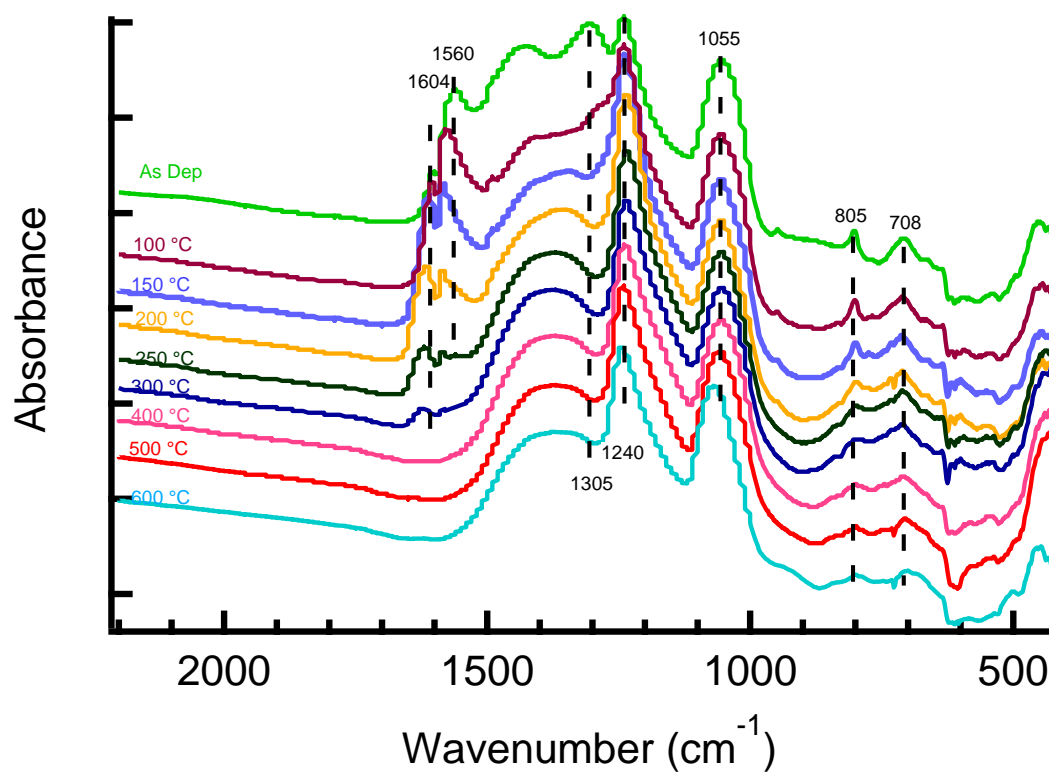


Figure 2.3: In situ difference FTIR data for an as deposited film (light green), and films heated to 100 °C (purple), 150 °C (light blue), 200 °C (yellow), 250 °C (dark green), 300 °C (dark blue), 400 °C (pink), 500 °C (red), and 600 °C (cyan). All spectra are referenced to a blank silicon substrate.

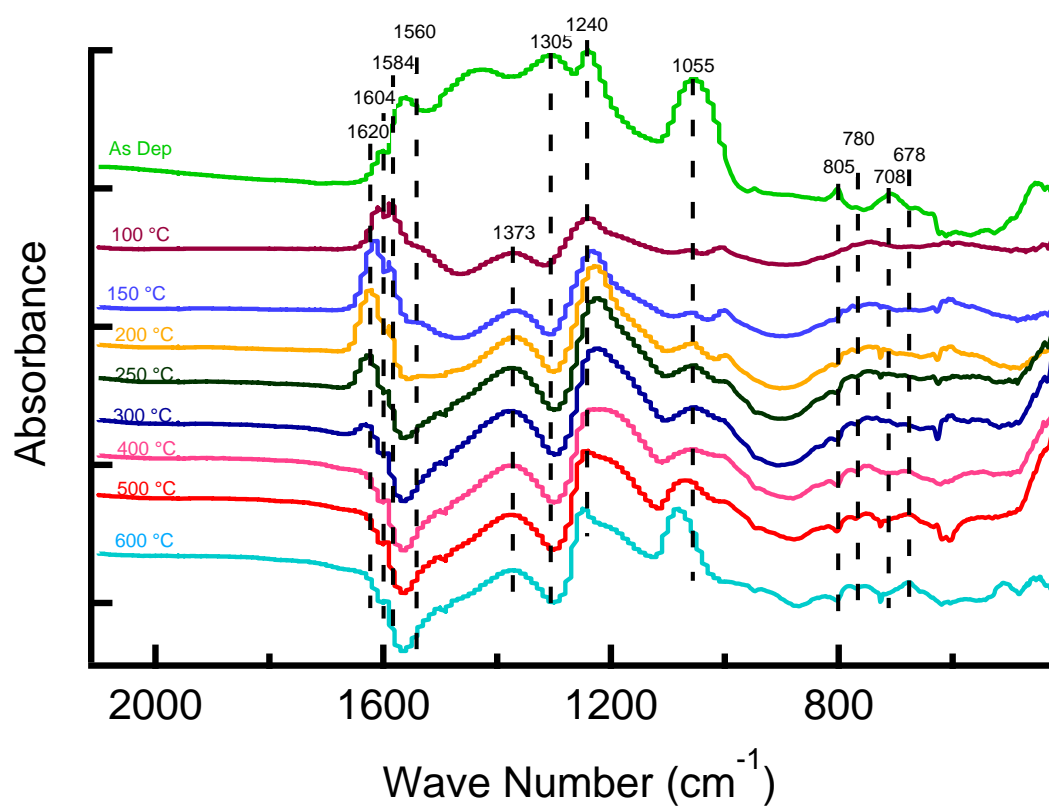


Figure 2.4: In situ difference FTIR data for an as deposited film (light green), and films heated to 100 °C (purple), 150 °C (light blue), 200 °C (yellow), 250 °C (dark green), 300 °C (dark blue), 400 °C (pink), 500 °C (red), and 600 °C (cyan). All heated spectra are referenced to the as deposited film.

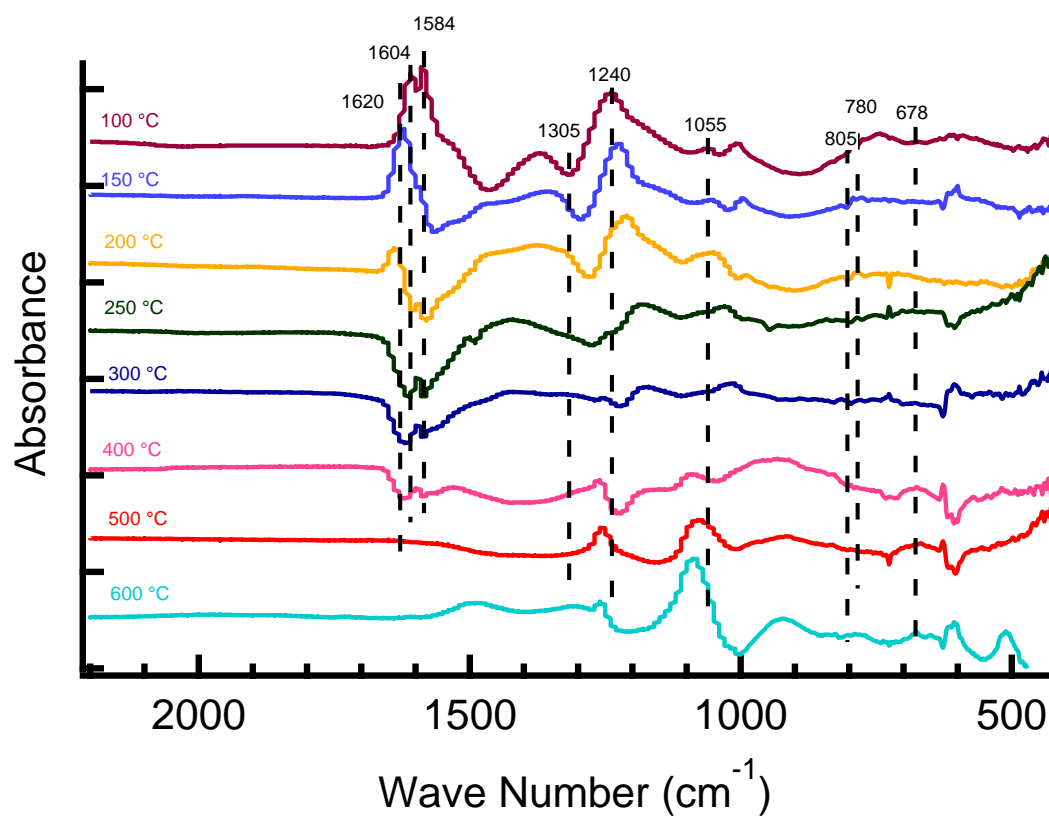


Figure 2.5: In situ difference FTIR data for films heated to 100 °C (purple), 150 °C (light blue), 200 °C (yellow), 250 °C (dark green), 300 °C (dark blue), 400 °C (pink), 500 °C (red), and 600 °C (cyan). All heated spectra are referenced to the previous temperature.

shifts are consistent with a decrease in solvation and increase in association of nitrate to hafnium as water loss occurs. A corresponding decrease in the  $1373\text{ cm}^{-1}$  peak, seen in figure 2.5, coincides with changes in the peaks at  $1605$  and  $1560\text{ cm}^{-1}$  indicating a decrease in solvated nitrate. These changes can point to both an increase in nitrate bridging and loss of nitrate as a water-nitric acid azeotrope. Above  $400\text{ }^{\circ}\text{C}$ , nitrate is no longer detected in the films.

Peaks at  $780$  and  $678\text{ cm}^{-1}$  correspond to monoclinic and amorphous hafnium oxide, respectively.[Figure 2.5] These stretches likely have small intensities because the films are very thin (approx.  $20\text{-}25\text{ nm}$ ). The peak at  $678\text{ cm}^{-1}$  starts to grow between  $250$  and  $300\text{ }^{\circ}\text{C}$ . [Figure 2.5] This is consistent with the formation of bridging oxide due to a loss of peroxide water and nitrate. Upon comparison to the as deposited film, no appreciable growth in the peak at  $780\text{ cm}^{-1}$  associated with the formation of monoclinic  $\text{HfO}_2$  is noted. [Figure 2.4] This may be due to the rate at which the films were heated being faster than what the films crystallize at in the given environment, or the low thickness of the film.

Peaks at  $1055$  and  $1240\text{ cm}^{-1}$  are associated with possible  $\text{SiO}_2$  growth. The presence of the peaks in the as deposited spectra in figures 2.3 and 2.4 show that the solution oxidizes the bare silicon wafer after deposition. This is expected since the solution contains nitrate, peroxide and water. The continued presence of peaks at these wavenumbers in figure 2.5 as the sample is heated shows an overall increase in the intensity of these peaks from each spectra to the next, suggesting possible  $\text{SiO}_2$  growth.

### **TPD-MS; Films Annealed in Air**

Temperature Programmed Desorption (TPD) Mass Spectroscopy analysis shows significant nitrate remains in films annealed below  $250\text{ }^{\circ}\text{C}$ . [Figure 2.6] From films

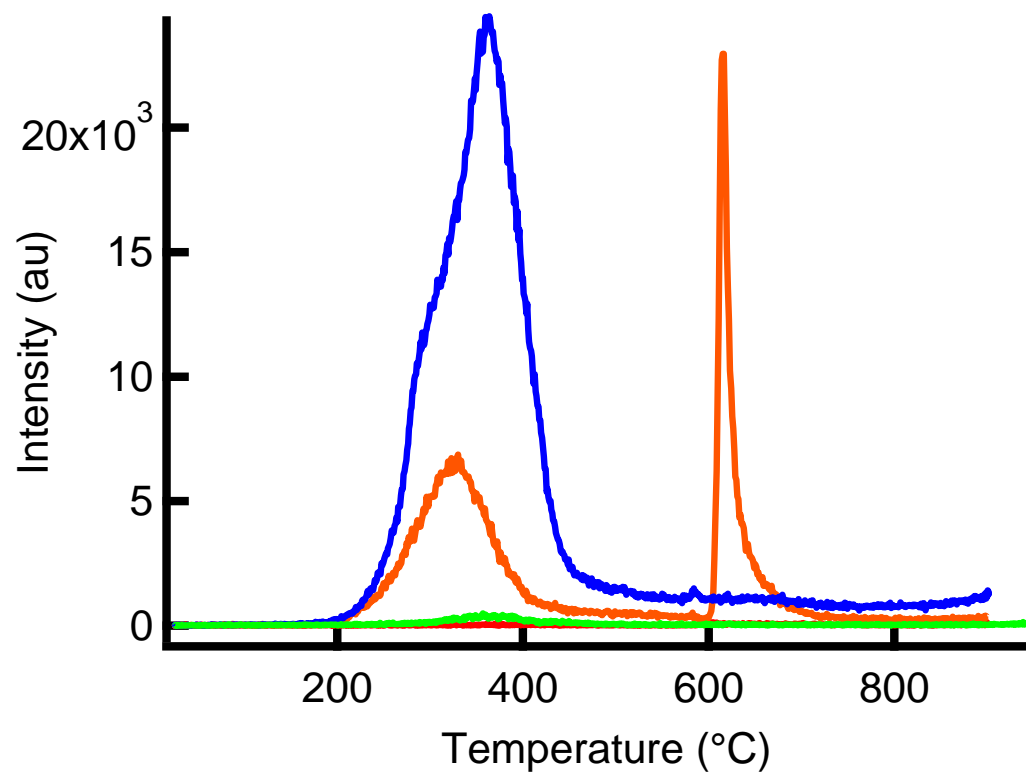


Figure 2.6: TPD-MS response for mass 30, NO<sub>(g)</sub>. Blue – 175 °C, 1 min; orange – 250 °C 1 min; green – 250 °C 1 hour; red – 350 °C 1 hour.

annealed for one min at 175 °C, decomposition product detected as NO (mass 30), are seen from 200 to approximately 475 °C with a peak maximum at just under 400 °C. Films annealed for one minute at 250 °C show nitrate removal occurring over two ranges, i.e., 200 - 400 °C, then 600 - 700 °C. The lower range is where the bulk of the nitrate decomposes as is consistent with in-situ IR data and TPD data for the 175 °C annealed film. The higher nitrate range, which is also seen in the bulk by TGA, is either residual nitrate that survives to a higher temperature due to the high ramp rate of 30 °C/min, or associated with NO gas that becomes kinetically trapped in the films after decomposition and is released rapidly upon crystallization of the films. This latter explanation is supported by in-situ IR of the films showing that no nitrate remains at temperatures above 400 °C. [Figure 2.4] While films from this system have been shown to crystallize at 500 °C, those films were heated and left to dwell at that temperature for 1 hour. [1] Films analyzed in TPD were heated at a ramp rate of 30 °C/ minute with no dwell time. This high ramp rate causes the films to survive in the amorphous state to a higher temperature due to slower kinetics of crystallization as can be seen in figure 2.7. Films heated to 500 °C in the TPD are amorphous. Crystallize occurs at 600 °C and films are polycrystalline. This allows for the nitrate decomposition products to diffuse a shorter rout to grain boundaries where they can escape the films more rapidly rather than diffuse through the film causing the sharp peak in the TPD at 600 °C seen in figure 2.6.

Films annealed in air at 250 °C for 1 h show very little nitrate remains. Samples annealed in air at 350 °C and above show no NO<sub>(g)</sub> detected.

Comparing the ranges of NO<sub>(g)</sub> desorption with those for the detection of O<sub>2</sub> and there is an expected commonality. For samples heated at 175 °C, O<sub>2</sub> desorbs from the films in

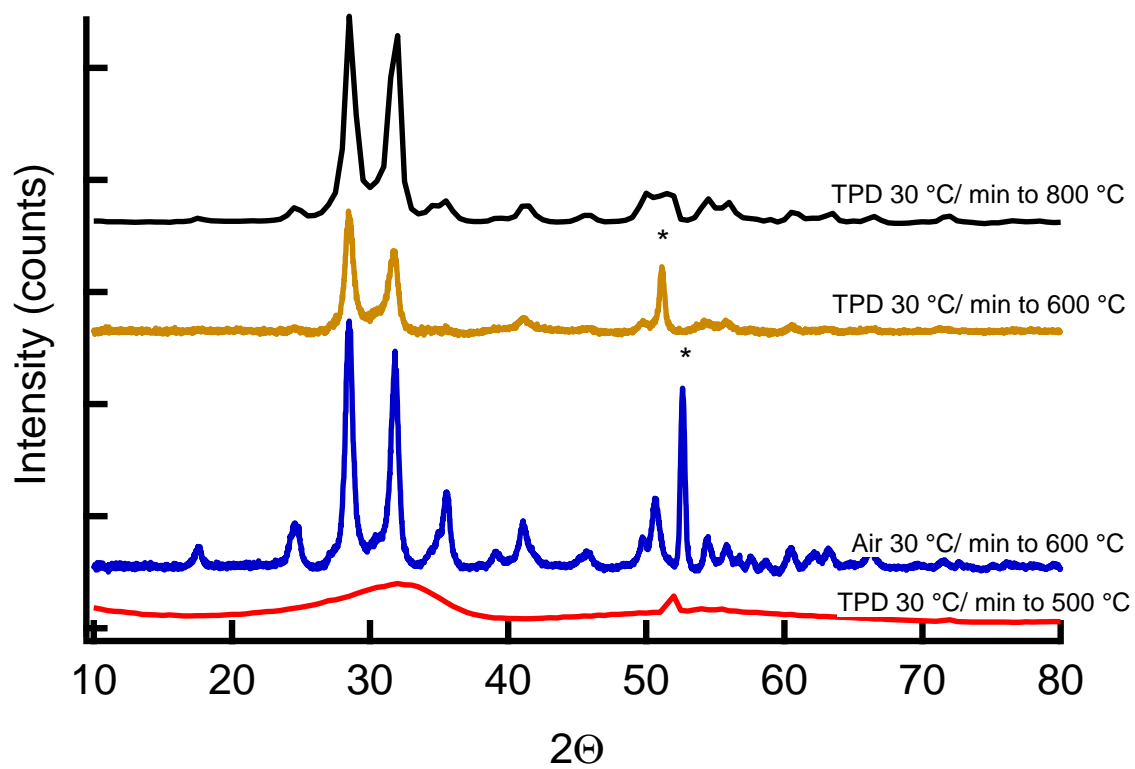
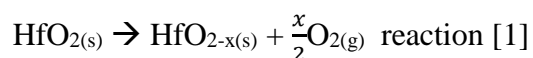


Figure 2.7: XRD for films annealed at a ramp rate of 30 °C/min in TPD to 500 °C (red), 600 °C (gold), 800 °C (black) and in air to 600 °C (blue). Substrate peaks denoted with a star.

three overlapping ranges from 50 to 450 °C then again at temperatures above 600 °C.[Figure 2.8] The lowest temperature oxygen peak is associated with peroxide decomposition. The next two smaller peaks are associated with nitrate decomposition. The higher temperature oxygen aside from the sharp onset in the 250 °C 1 min annealed sample is not associated with any other known reaction or the detection of any other species in the mass spec. The sharp peak for the spectra of the 250 °C 1 min annealed film setting in at 600 °C is associated with a similar sharp peak in the NO spectra, however the remaining oxygen signal has no corresponding NO<sub>(g)</sub> detected in the same range. With a gradual onset and sudden drop off, this molecular oxygen does not appear trapped in the films as the NO gas is. The evolution of this gas is not associated with any phase change as crystalline films before and after the evolution of O<sub>2</sub> are polycrystalline monoclinic. [Figure 2.7] And unlike NO which is not detected in films that no longer contain nitrate, high temperature O<sub>2</sub> is detected in all films with the exception of those annealed in argon above 450 °C. This leaves three possible sources of high temperature O<sub>2</sub>. The first possible source is the creation of oxygen vacancies per reaction [1]. In the high vacuum environment of the TPD at this temperature this would be a thermodynamically favored process.



The second possible source is a reaction at the interface. This has been seen to occur in films deposited by ALD and heated under high vacuum though not until temperatures above 850 °C.[6] The third possibility is residual O<sub>2</sub> from the decomposition of nitrate that is kinetically trapped or intercalated into the films. A similar phenomenon was noted by Qixi et al with small amounts of N<sub>2</sub> intercalating into WO<sub>3</sub> lattice.[7] This residual O<sub>2</sub> could also explain why densities of these films first reported by Jiang et al only reached a

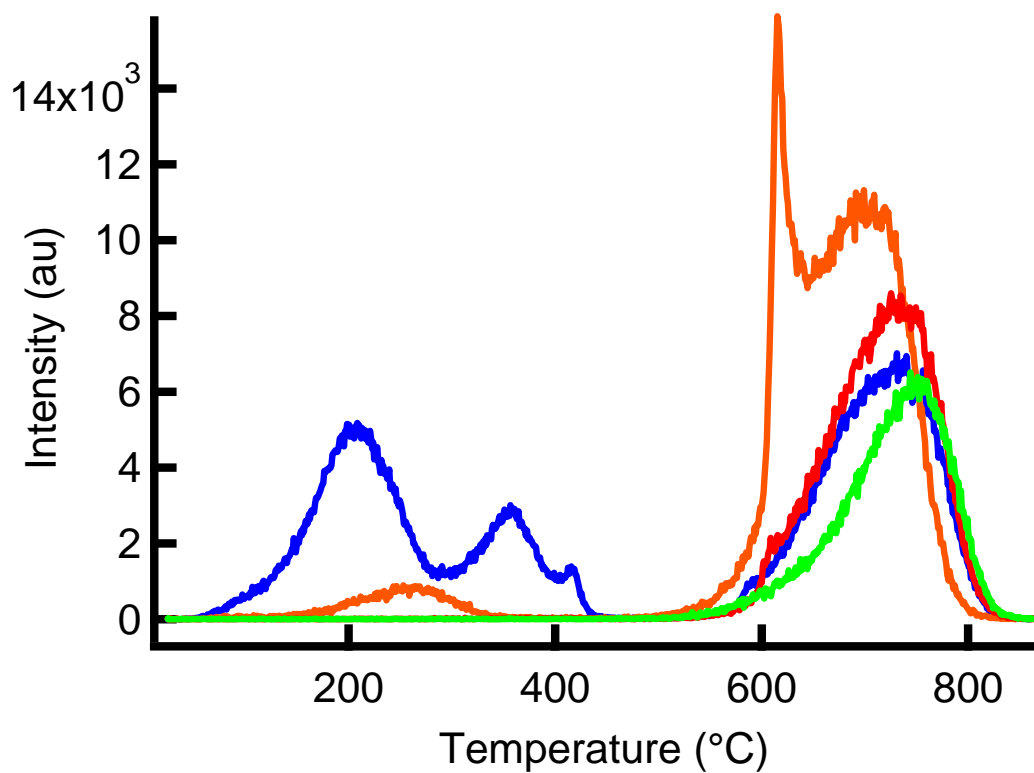


Figure 2.8: TPD-MS response for mass 32 O<sub>2</sub>. Samples are from the hafnium precursor and soft baked 175 °C (blue), soft baked 250 °C (orange), air annealed for 1 hour 250 °C (green) and air annealed 350 °C 1 hour (red).

maximum of 86%. Density does not increase once the O<sub>2</sub> leaves the film as heating to the higher temperature promotes larger grain growth and film roughening. Residual O<sub>2</sub> though possible is less likely as we would expect to see this high temperature O<sub>2</sub> in the TGA in figure 2.1, but don't. This means the phenomenon is most likely due to some interaction with the substrate and or high vacuum environment.

The difference in how the nitrate is lost in the 175 °C versus the 250 °C films annealed for one min can be attributed to crust formation at the higher temperature due to loss of peroxide and partial loss of constitutional water and nitrate at the surface. Figure 2.8 shows O<sub>2</sub> desorption begin near 100 °C and figure 2.6 shows NO desorption begin at 200 °C for films annealed at the lower temperature. For films annealed at the higher temperature these processes have already been partially completed and the films have undergone a greater degree of densification. Films annealed at the lower temperature have a lower degree of cross-linkage between hafnium species that allows the films to remain at a lower density throughout while NO diffuses out of the film. This is consistent with a top down process for nitrate and water loss and has been noted in other aqueous hafnium based precursors.[8]

TPD on films annealed at 250 °C for 1 h show the majority of nitrate is removed and there is no high temperature nitrate detected. Films annealed in air at 350 °C and above show no detectable NO, however the broad high temperature O<sub>2</sub> remains.

Water is detected from 60-450 °C in films that have been annealed for 1 minute at 175 and 250 °C and films annealed for an hour at 175 and 250 °C.[Figure 2.9] The shapes and relative intensities of these curves show that films annealed for 1 minute contain less constitutional water than their hour long annealed counterparts. This is most likely do to films being annealed for longer times being more dense and preventing the high vacuum

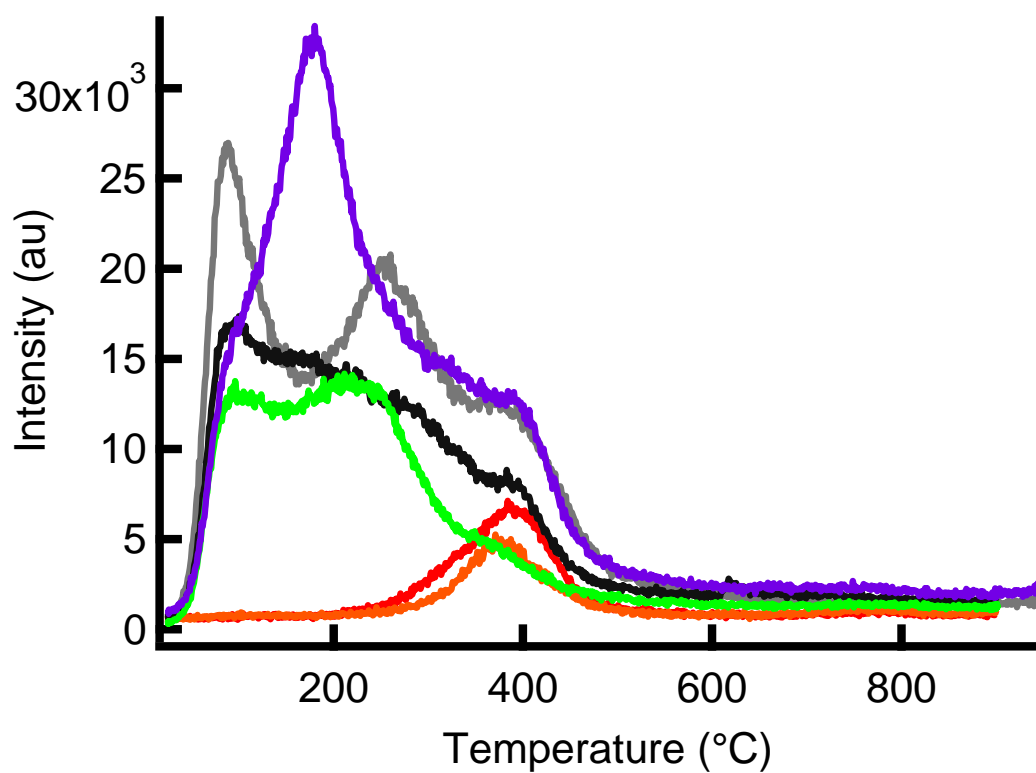


Figure 2.9: TPD mass response corresponding to water for films annealed for 1 min at 175 °C (green), 250 °C (black), and 1 hour at 175 °C (purple), 250 °C (gray), 350 °C (red) and 450 °C (orange).

environment of the TPD from removing most of the water. Also comparing the shapes of the two films annealed for 1 hour shows larger amounts of higher temperature constitutional water for the 175 °C annealed film compared to the 250 °C film. This suggests that the lower temperature annealed film contains more waters that are closely associated with the inner solvation spheres for the Hf species in solution. For films annealed at 250 °C these waters are removed to a greater degree, yet the large amount of water and continued presence of nitrate in the films causes them to readily reabsorb water from the atmosphere that is detected as the lower temperature water. For films annealed at 350 and 450 °C for 1 hr water is only detected over a small range centered at 400 °C.

Peak fitting analysis for a selected mass 18 spectra shows that water leaves these films in four ways: low temperature adsorbed water centered near 90 °C, higher temperature constitutional water centered near 130 °C, non-isolated hydroxides centered around 230 °C, and isolated hydroxides around 400 °C. [Figure 2.10] The presence of water in these films both as constitutional water and hydroxide bonds may also be affected by the presence of nitrate. Films annealed at temperatures below 350 °C and times less than 1 hour that still contain nitrate also uptake water from the surrounding atmosphere. This is seen in the TPD as low temperature water that desorbs almost immediately and is fully removed by approximately 200 °C.

The next two peaks in figure 2.10 are associated with hydroxide, the higher of which is associated with isolated hydroxide bonds that require proton migration to another hydroxide to release as water. This condensation follows a metal hydroxide condensation reaction resulting in a metal-oxygen-metal bridge and the evolution of water.

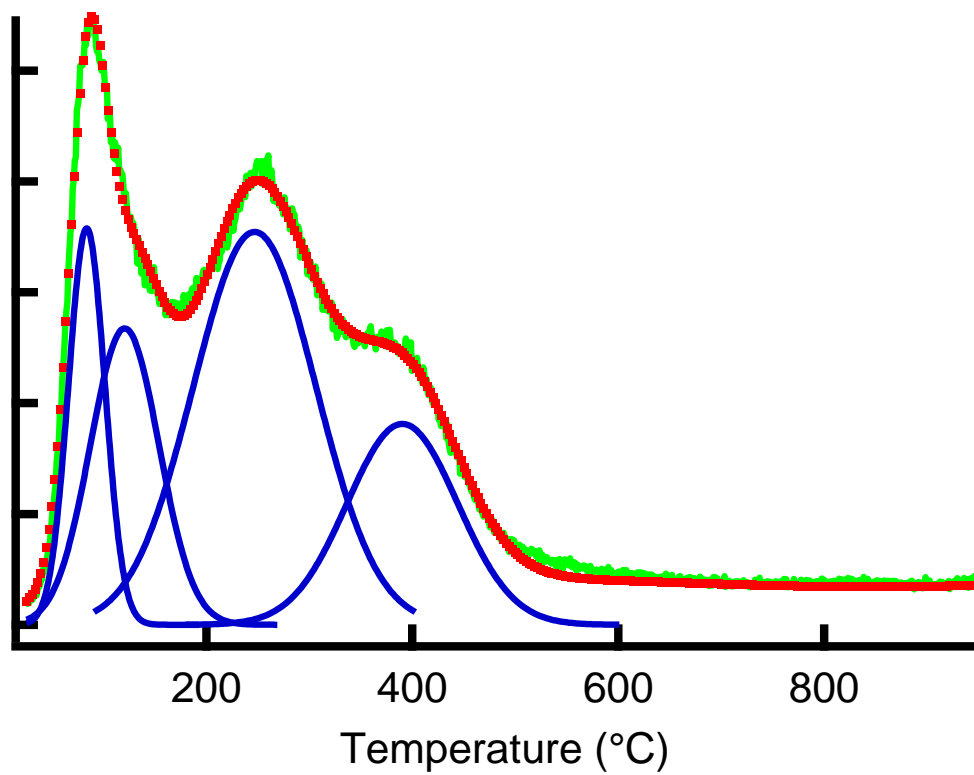


Figure 2.10: Peak fitting analysis for mass 18 TPD spectra on film annealed for 1 hour at 250 °C. Green is the raw spectra, blue are the individual Gaussian peaks and red is the sum of the individual peaks.

Films annealed at 350 and 450 °C for one hour show only one peak in TPD at 400 °C.[Figure 2.9] Films annealed in the TPD for 1 h at 450 °C that are then brought out of vacuum and allowed to sit in air for 1 week show no desorption water peak at 400 °C. This observation suggests water resorption is not the source of the 400 °C water desorption in the air-annealed films. The water peaks are most likely associated with isolated hydroxides; then removal is aided by the high-vacuum TPD environment.

### **Argon Annealing**

Annealing in an argon atmosphere had an effect on the way nitrate and water are removed relative to ambient air conditions. Films annealed in argon at 350 °C for 1 h had marginally more NO detected than those annealed in air at the same temperature. However all NO was detected at the higher 600 °C mark and exhibited similar behavior as the high temperature nitrate in lower temperature air annealed films.[Figure 2.11] Considering this result in the context of the residual water in the films, TPD shows a fraction of the water present as hydroxide bonds in the films. This may indicate a greater degree of condensation and therefore higher density in the films. This increased densification could prevent the release of NO until the films crystallized at 600 °C in the TPD experiment. Films annealed at 450 °C had no detected NO gas and therefore no remaining nitrate.

Water was only detected at the higher temperature range associated with isolated hydroxide. [Figure 2.12] Peak integration of these data puts the amount of detected water for the 350 °C film at 3 % of the total amount detected in the films annealed in air at 175 °C for 1 hour. The 450 and 500 °C film are less than 1 %.

Of particular note is the presence of high temperature O<sub>2</sub>. Films annealed at 350 °C in argon still contained high temperature O<sub>2</sub> that desorbs beginning at 600 °C, while films

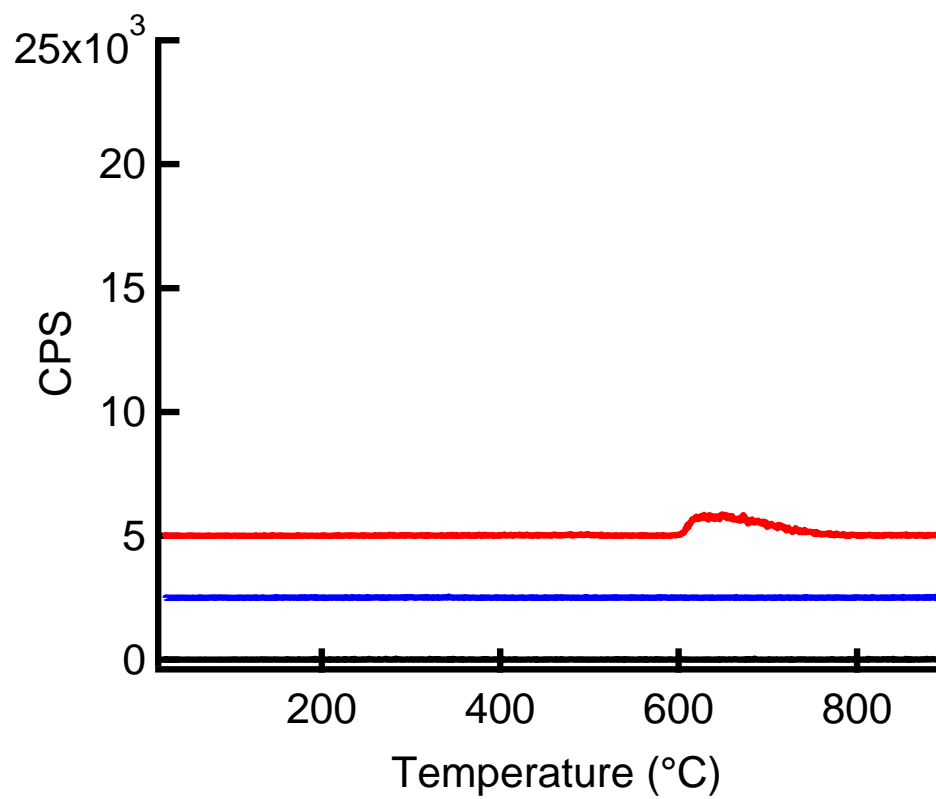


Figure 2.11: TPD-MS data for NO (mass 30) on films annealed in argon atmosphere for 1 hour at temperatures of 350 °C (red), 450 °C (blue) and 500 °C (black).

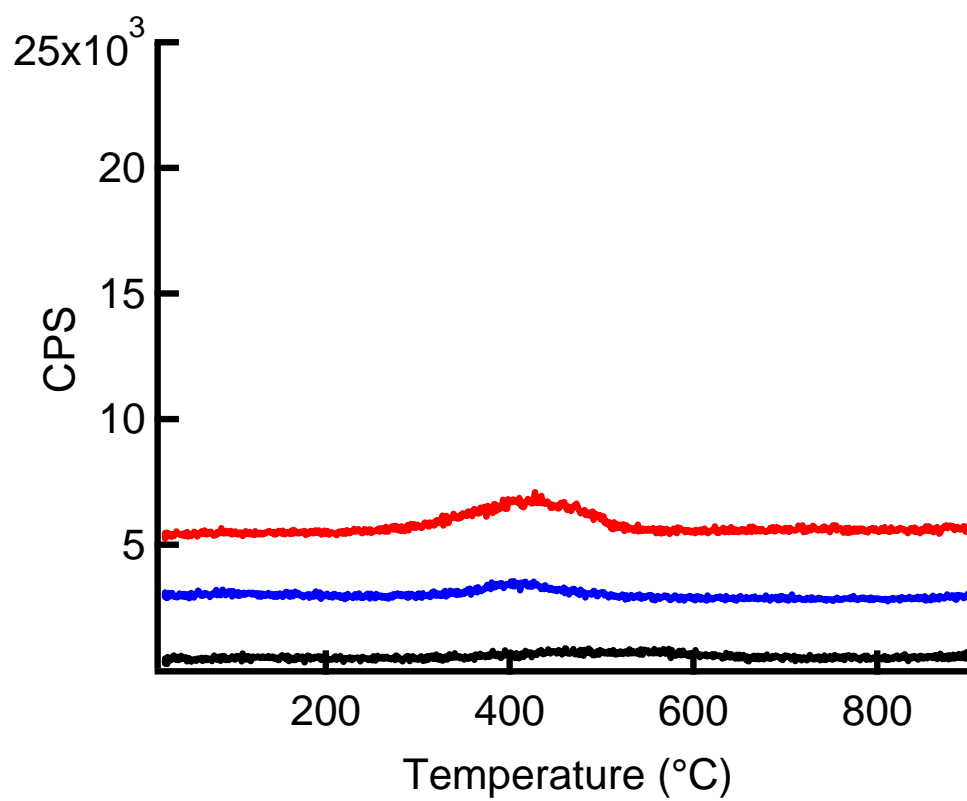


Figure 2.12: TPD MS data for water (mass 18) on films annealed in argon atmosphere for 1 hour at temperatures of 350 °C (red), 450 °C (blue) and 500 °C (black).

annealed to 450 °C did not.[Figure 2.13] These data indicate that the lack of oxygen in the annealing environment drives desorption of oxygen from the films at lower temperatures, but delays the thermal decomposition of nitrate to some degree.

### **Pure Oxygen Annealing**

Annealing in pure O<sub>2</sub> had no major effect on nitrate loss compared to annealing in air. After annealing to a temperature of 350 °C for 1 h almost no NO was detected via TPD. There was however a large difference in residual water/hydroxide compared to argon anneals at 350 °C. [Figure 2.14] Like samples annealed in other environments, nearly all residual water evolved in the temperature range associated with isolated hydroxide. In pure O<sub>2</sub>, however, there was a significantly large increase in the mass signal compared to the argon anneal. Since this was also a dry environment like the argon anneals, this shows us that lower humidity does not promote hydroxide loss on its own.

When we consider the residual oxygen in the films that are present in the pure O<sub>2</sub> annealed samples, a trend begins to emerge. All films that are found to give a high temperature O<sub>2</sub> signal also contain considerable residual hydroxide after annealing to 350 °C. This observation points to molecular O<sub>2</sub> in the films as an inhibitor condensation and water loss.

### **Neutralization and Steam Annealing**

Nitrate can be removed before the annealing step from multi-coat films in samples that have undergone a one minute anneal at 175 °C. Films soaked in water for 10 minutes show a large decrease in the amount of nitrate present and are on par with films annealed for 1



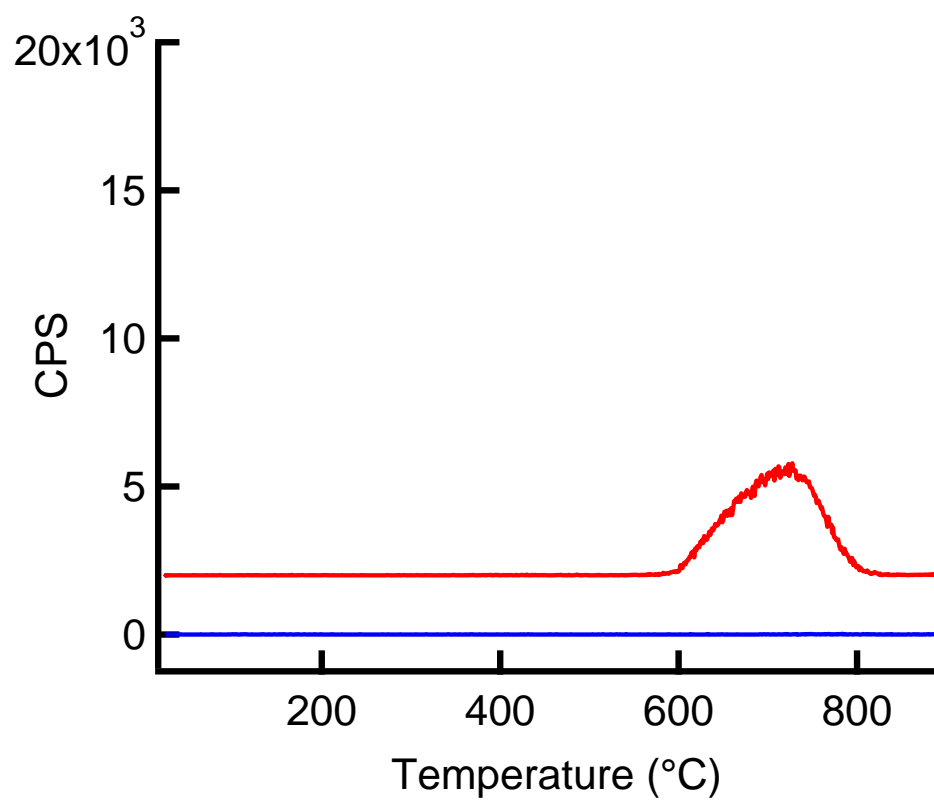


Figure 2.13: TPD mass response for molecular oxygen (mass 32) for films annealed in argon for 1 hour at 350 °C (red) and 450 °C (blue).

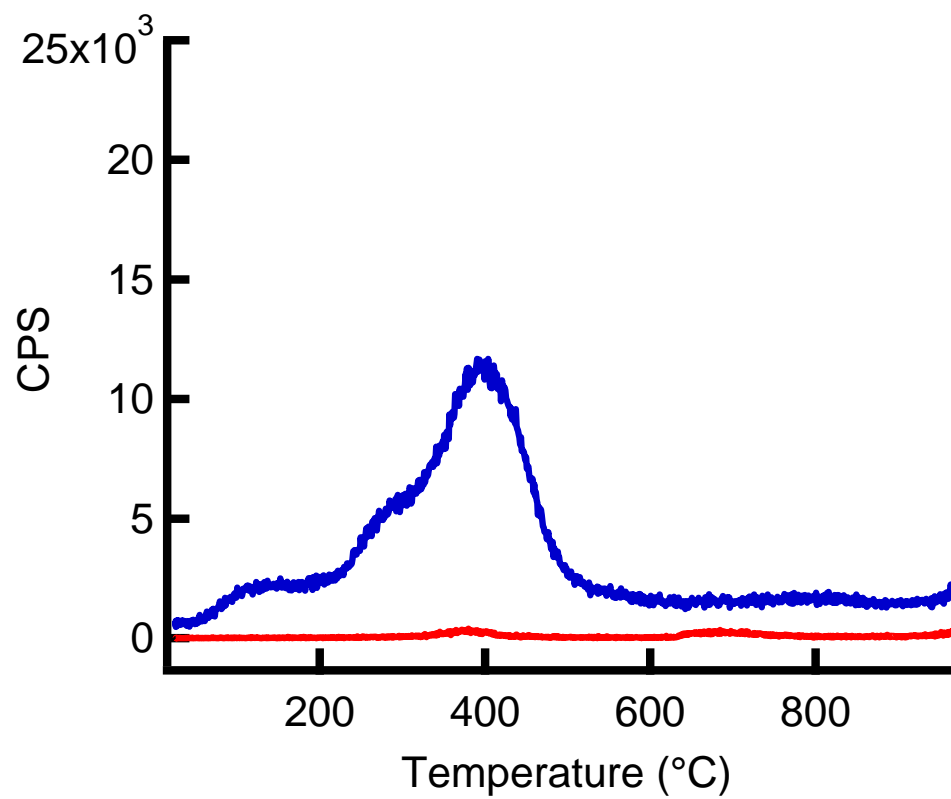


Figure 2.14: TPD mass response for water or mass 18 (blue) and NO or mass 30 (red) for films annealed in pure  $O_2$  for 1 hour at 350 °C.

hour at 175 °C.[Figure 2.15] This loss of nitrate occurs by an acid base neutralization. When submerged, water solvates the nitrate ligand. In doing so, the nitrate ligand deprotonates a water ligand associated with an  $\text{Hf}^{4+}$  and leaves the film as nitric acid leaving behind a hydroxide ligand.(eq 1) This dangling hydroxide is then free to undergo a condensation event with an adjacent Hf-OH or Hf-H<sub>2</sub>O.[9] In the case of two adjacent Hf-OH groups, this would lead to a double hydroxide bridging scheme to form the same -OH bridges seen in the hafnium tetrameric cluster.[10,11] In the case of a condensation between an Hf-OH and Hf-H<sub>2</sub>O, this would lead to a single hydroxide bridge and more isolated hydroxides in the films which can be seen in Figure 2.15. The detection of nitrate decomposition products in these films however points to a finite penetration of water into the film. As films for TPD analysis have to be at least 40 nm in thickness, it stands to reason that thinner films such as those used for a thin film transistor or tunneling based device would likely have all nitrate removed in this method. [Figure 2.15] Additional support for this explanation comes from the fact that almost all NO is detected at the higher temperature and exits sharply upon crystallization. This is consistent with densification at the top as the neutralization occurs in only a finite depth of the film.

Increasing the humidity of the annealing environment has a significant effect on nitrate loss as well. Water in the form of steam aids in the loss of nitrate in these films by solvating the nitrate and removing it as a nitric acid/water azeotrope which has a boiling point of 120 °C. [Figure 2.16] The amount of nitrate remaining in the films is comparable to films annealed at 350 °C in argon despite these films being annealed at 125 °C. This marks a 225 °C reduction in the temperature required to remove nitrate. As with the neutralization,

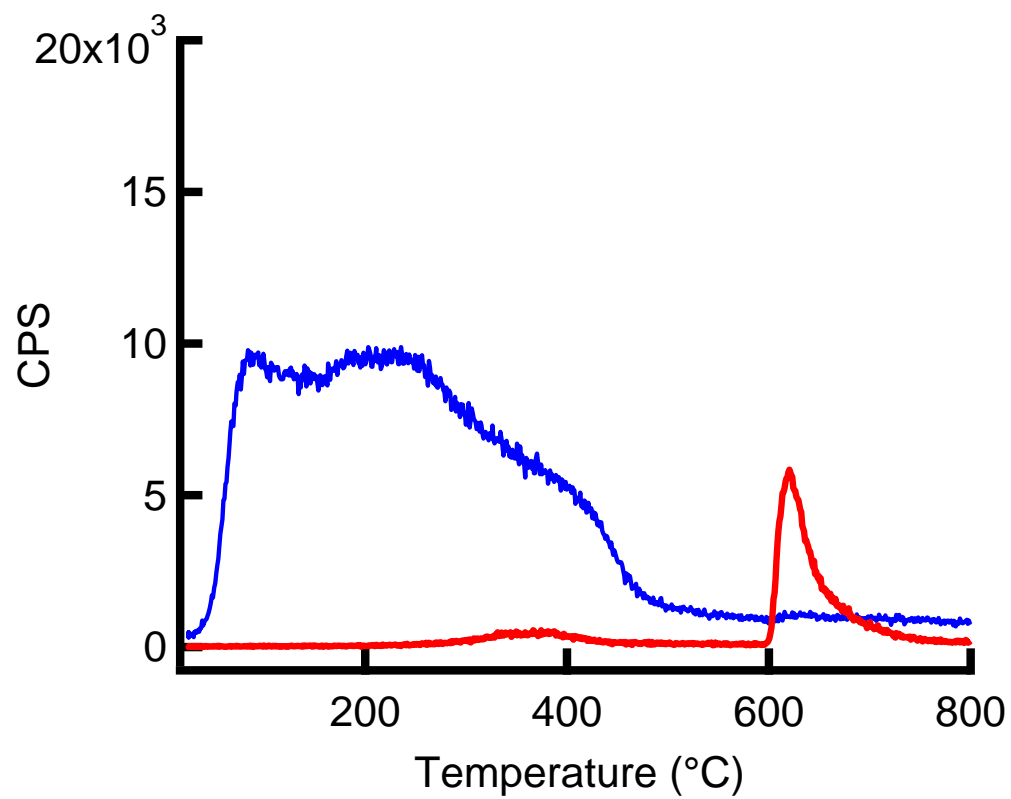


Figure 2.15: TPD mass response for water or mass 18 (blue) and NO or mass 30 (red) for films neutralized in a water bath for 10 minutes.

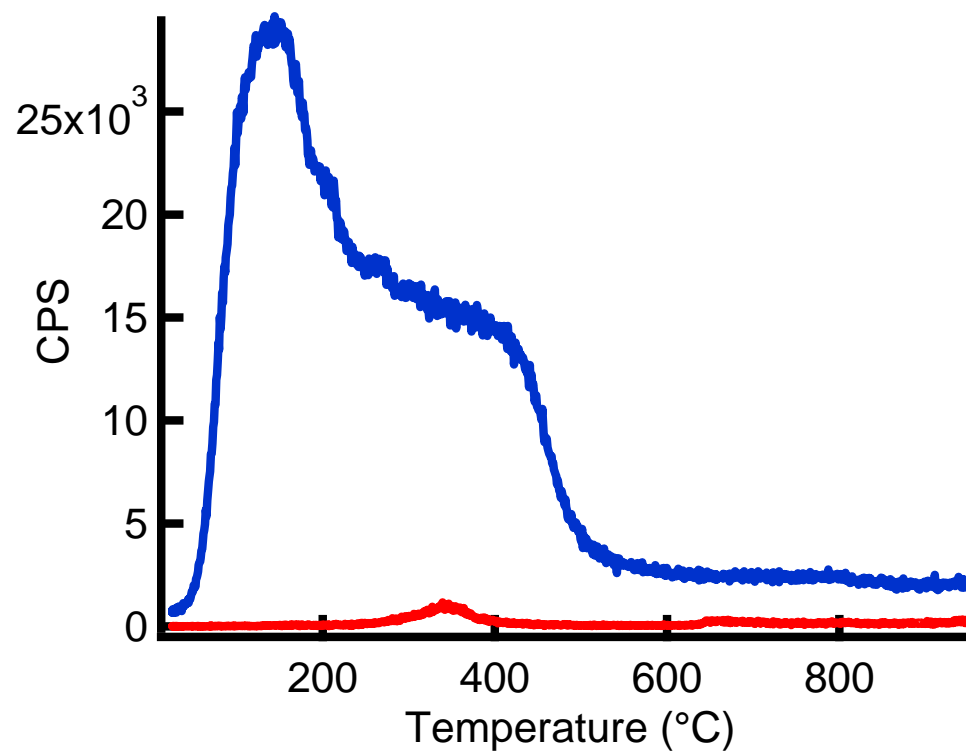


Figure 2.16: TPD mass response for water or mass 18 (blue) and NO or mass 30 (red) for films annealed in steam for 1 hour at 125 °C.

it stands to reason that there is a finite distance that the steam can penetrate into the film to remove nitrate, and this technique would remove all nitrate from thinner films.

Examining the residual water in the steam annealed films shows a large increase in the amount of water present. This increase suggests that excess water enters the film as the partial pressure of water vapor increases in the annealing environment and then becomes trapped in the films as condensation due to nitrate loss occurs. [Figure 2.16]

Relative amounts of residual nitrate and water that remains in the films show that air annealing at 350 °C is the minimum temperature that is require to remove all nitrate thermally from thicker films, though in thinner films nitrate can be removed chemically in a steam anneal at 125 °C. [Figure 2.17] Normalizing all data to the 1 minute anneal in air at 175 °C and integrating the curve data we can compare the amounts of residual nitrate remaining in the films. The best performer at low temperatures is the steam anneal with just under 4% of the nitrate remaining compared to the 1 minute anneal at 175 °C. However the lowest temperature treatment to fully remove nitrate from the films is at 350 °C for 1 hour. An elevated steam anneal was not performed as crust formation at the elevated temperatures may hinder steam penetration into the films.

The residual water data are normalized to the 1 h long anneal at 175 °C. The removal of water is different from nitrate and a comparison of relative amounts of residual water show that steam annealing is the poorest performer while annealing at 350 °C in argon is the lowest temperature that all water can be removed. [Figure 2.18]

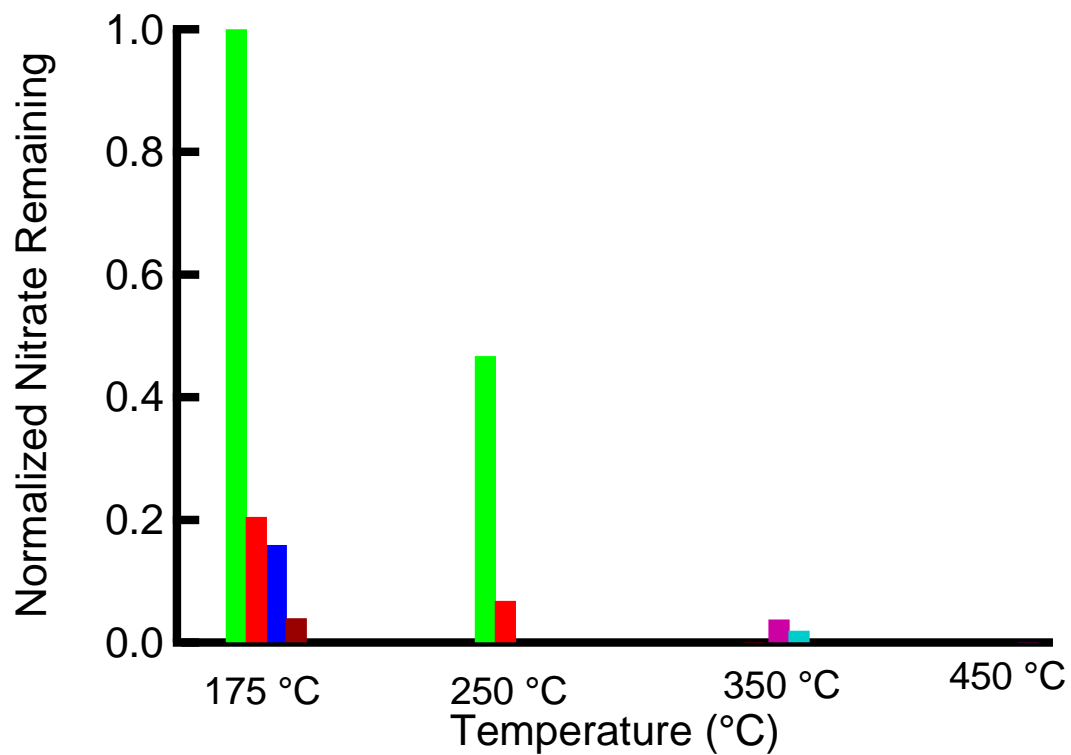


Figure 2.17: Integrated TPD data showing residual nitrate normalized to the 175 °C 1 minute annealed film. Green are 1 minute anneals, red are 1 hour long anneals dark blue is neutralized films, brown is steam annealed at 125 °C but set baked at 175 °C for 1 minute, pink is annealed in argon for 1 hour, and cyan is annealed in pure O<sub>2</sub> for 1 hour.

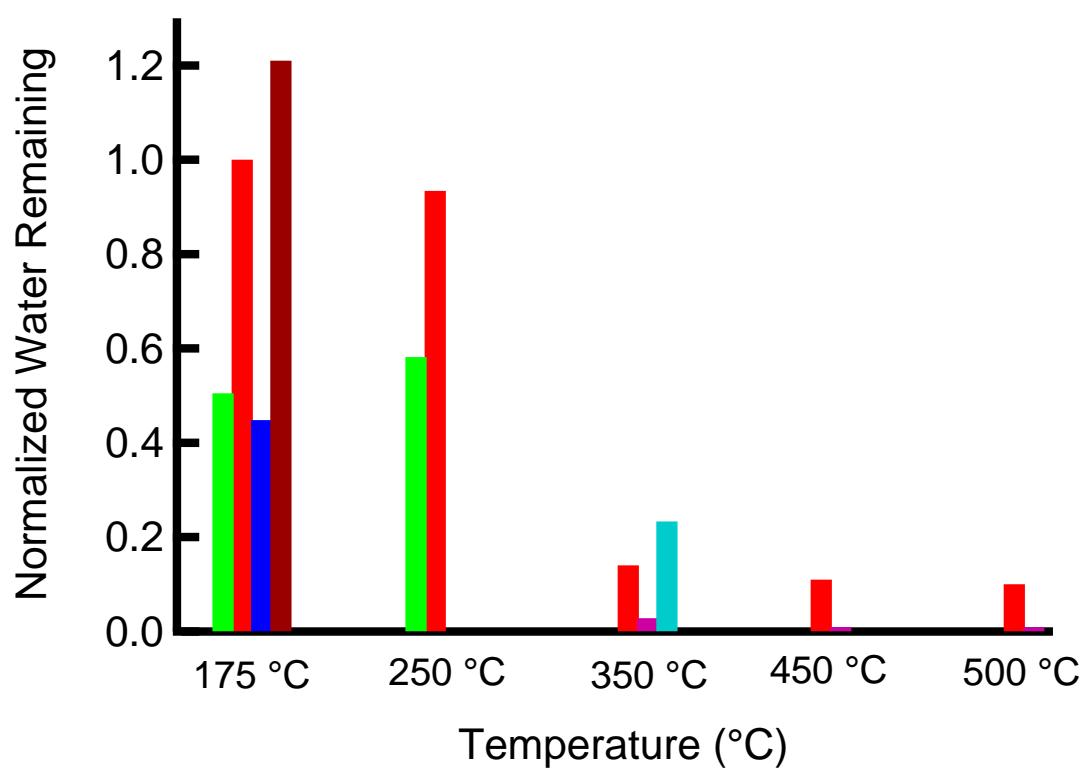


Figure 2.18: Integrated TPD data showing residual water normalized to the 175 °C 1 hour annealed film. Green are 1 minute anneals, red are 1 hour long anneals dark blue is neutralized films, brown is steam annealed at 125 °C but set baked at 175 °C for 1 minute, pink is annealed in argon for 1 hour, and cyan is annealed in pure O<sub>2</sub> for 1 hour.

## Conclusions

The hafnium hydroxo-peroxo-nitrate precursor annealing temperature profile shows that individual species can be removed thermally by changing annealing conditions, but ultimately a lower temperature cannot be realized through thermal means alone. Neutralization either by submerging in water or through steam annealing shows promise, but should ultimately be investigated with other means of removing water such as pulsed laser annealing or pulsed microwave annealing. Congruently, in order to achieve higher densities with this precursor a means for removing oxygen from the system at a lower temperature should be explored. Other alternatives would require the possible replacement of nitrate with a non-oxoanionic species.

## Methods

### Solution and Sample Preparation

The hafnia film precursor,  $\text{HafNO}_x$ , was made from a previously reported method, with a resultant solution concentration of 0.4 M with respect to hafnium.[1] Thin films were spun-coated at 3000 rpm for 30 seconds on 100 nm thermally grown  $\text{SiO}_2$  on Si, cleaved into 2.5 cm<sup>2</sup> squares. The films were multicoated to build thickness. (3 coats in every case) and annealed at either 175 or 250 °C after every coat. Substrates were made hydrophilic by sonication in a Contrad 70 bath at 45 °C for 60 minutes. Post deposition soft bakes were conducted at either 175 °C for 1 minute on all samples annealed at 175 °C or lower and 250 °C for one minute for all samples annealed at 250 °C or higher. A Neytech Qex furnace was used to anneal the films in air. Films annealed in argon and pure  $\text{O}_2$  were annealed in a tube furnace under a low flow of the respective gas. For heating in the Neytech and tub furnaces a ramp rate of 10 °C/ minute was used. Steam annealing was conducted on a hotplate set to 125 °C for one h. The sample was placed under a large beaker along with a smaller beaker of boiling water with boiling stones added.

### **Thermogravimetric Analysis**

TGA-DT-MS was performed under argon (Ar) atmosphere using TA Instruments Q600 equipped with a Hiden Analytical HPR-20 quadrupole mass analyzer. Samples (~30 mg) were heated at a rate of 10 °C min<sup>-1</sup> under argon (flow rate: 100 mL min<sup>-1</sup>) in alumina sample pans. Electron impact (EI) mass spectra were acquired with a 70 eV ionization energy and 100 μA emission current. Selected mass-to-charge (m/z) ratios for each sample were monitored in multiple ion detection (MID) mode with a dwell time of 500 ms and a settle time of 50 ms. The sample for this analysis was prepared by allowing an aliquot of the hafnia precursor to evaporate and form a glass. The glass was then ground to a powder for analysis.

### **ATR Analysis**

FTIR data was collected on a Thermo Fischer Scientific Nicolet 6700 FTIR equipped with a diamond ATR. The spectra was scanned from 4000 – 500 cm<sup>-1</sup> at a resolution of 8 cm<sup>-1</sup>.

### **FTIR Analysis**

In-situ FTIR spectroscopy studies were carried out using a nitrogen-purged home-built ALD reactor with a Thermo Nicolet 6700 infrared spectrometer equipped with a liquid nitrogen-cooled broadband mercury cadmium telluride (MCT-B) detector.[12] After heating to a selected set point in flowing N<sub>2</sub>(g), the films were cooled to 80 °C for data collection. A single-pass transmission at Brewster incidence angle of 74° was used to minimize the substrate phonon absorption in the range <1000 cm<sup>-1</sup> and to increase detection sensitivity of all film chemical components. A K-type thermocouple spot-welded onto a tantalum clip was attached at the center of the long edge of the substrate to monitor the sample temperature. Two gate valves were used to isolate the KBr windows used in the analysis chamber for IR transmission during annealing.

### **Temperature Programmed Desorption**

TPD measurements were performed on a Hiden Analytical TPD workstation with a quadrupole mass analyzer (3F PIC). The measurement was performed with a temperature ramp rate of 30 °C/min and under ultra-high vacuum at a base pressure  $< 5 \times 10^{-9}$  Torr. Spectra were obtained with a 70 eV ionization potential and 20- $\mu$ A emission current. Thin-film samples (2.5 x 2.5 cm<sup>2</sup>) were cleaved into 1 x 1 cm<sup>2</sup> squares for the analysis.

### **Author Information**

#### **Corresponding Author**

\*D. A. Keszler, 153 Gilbert Hall, Oregon State University, Corvallis, Oregon 97331,  
Douglas.Keszler@oregonstate.edu Present Addresses

#### **Funding Sources**

This work was supported by the National Science Foundation Center for Sustainable Materials Chemistry, grant CHE-1102637.

## References

- [1] Jiang, K.; Anderson, J. T.; Hoshino, K.; Li, D.; Wager, J. F.; Keszler, D. a. *Chem. Mater.* **2011**, *23*, 945–952.
- [2] Montaudo, G.; Puglisi, C.; Samperi, F. *Polym. Degrad. Stab.* **1993**, *42*, 13–28.
- [3] Lupina, G.; Kozlowski, G.; Dudek, P.; Dabrowski, J.; Wenger, C.; Lippert, G.; Müssig, H. J. *ULIS 2008 - 9th Int. Conf. Ultim. Integr. Silicon* **2008**, 159–162.
- [4] Li, F. M.; Bayer, B. C.; Hofmann, S.; Dutson, J. D.; Wakeham, S. J.; Thwaites, M. J.; Milne, W. I.; Flewitt, A. J.; Li, F. M.; Bayer, B. C.; Hofmann, S.; Dutson, J. D.; Wakeham, S. J.; Thwaites, M. J.; Milne, W. I.; Flewitt, A. J. **2012**, 252903.
- [5] Yuvaraj, S.; Lin, F. Y.; Chang, T. H.; Yeh, C. T. *J. Phys. Chem. B* **2003**, *107*, 1044–1047.
- [6] Sayan, S.; Garfunkel, E.; Nishimura, T.; Schulte, W. H.; Gustafsson, T.; Wilk, G. D. *J. Appl. Phys.* **2003**, *94*, 928.
- [7] Mi, Q.; Ping, Y.; Li, Y.; Cao, B.; Brunshwig, B. S.; Khalifah, P. G.; Galli, G. a; Gray, H. B.; Lewis, N. S. *J. Am. Chem. Soc.* **2012**, *134*, 18318–18324.
- [8] Fairley, K. C.; Merrill, D. R.; Woods, K. N.; Ditto, J.; Xu, C.; Oleksak, R. P.; Gustafsson, T.; Johnson, D. W.; Garfunkel, E. L.; Herman, G. S.; Johnson, D. C.; Page, C. J. *ACS Appl. Mater. Interfaces* **2016**, *8*, 667–672.
- [9] Henry, M.; Jolivet, J. P.; Livage, J. *Chem. Spectrosc. Appl. Sol-Gel Glas.* **1992**, *77*, 153–206.
- [10] Hagfeldt, C.; Kessler, V.; Persson, I. *R. Soc. Chem.* **2004**.
- [11] Aberg, M.; Glaser, J. *Inorganica Chim. Acta* **1993**, *206*, 53–61.
- [12] Kwon, J.; Dai, M.; Halls, M. D.; Langereis, E.; Chabal, Y. J.; Gordon, R. G. **2009**, 654–660.

## Chapter 3: Hafnia Films from an Alkaline pH Precursor

### **Introduction**

Hafnium oxide has shown a great deal of interest in recent years as a replacement for  $\text{SiO}_2$  as a dielectric material.[1–3] With the push for sustainability, techniques involving solution processing have gained interest as a means of innovation.[4–9] Though hafnium in solution has been explored for decades these have been predominantly in the low pH region.[10–12][Figure 3.1] Recently, a polyoxometalate species of hafnium has been realized by Goberna-Feron et al.[13] The structure of this cluster is a six membered hafnium ring with bridging peroxide and hydroxide species. This allows for hafnium to be used in basic conditions and provides a new realm of possible uses. In this contribution, the first findings regarding a basic hafnium oxide precursor for thin film applications are discussed.

### **Results and Discussion**

#### **Solution Characteristics**

The synthesis route outlined in this contribution produces a usable solution with a longer shelf life than dissolving the crystalline  $\text{TMA}_6\text{Hf}_6(\text{O}_2)_6\text{OH}_{18}$  first reported on by Goberna-Feron et al.[13] Crystals of the hexameric cluster readily dissolve in solution but turn cloudy and the solution begins to solidify into a gel a few hours after dissolution. Solutions synthesized by the single pot method outlined here stay clear and liquid for up to 4 weeks. After first synthesizing the precursor, the solution is a faint yellow color. This is due to residual chlorine left behind from the  $\text{HfOCl}_2$  starting material which undergoes oxidation

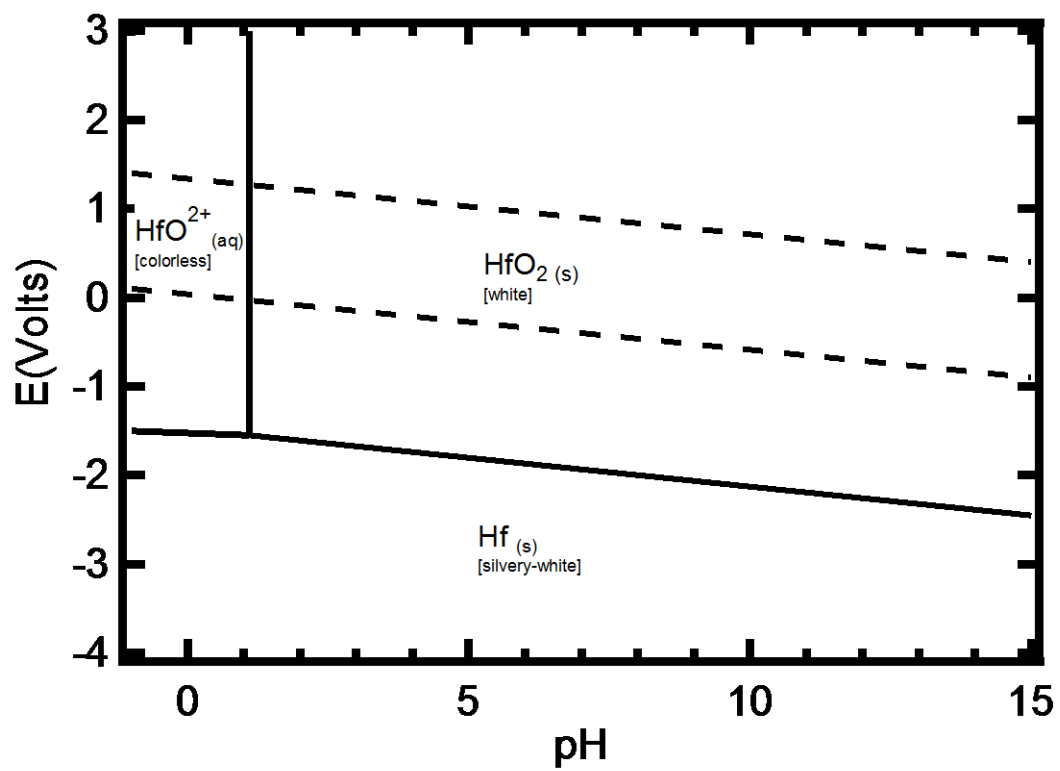


Figure 3.1: Pourbaix diagram of Hf in water.

to become elemental chlorine dissolved in solution. Analogs were also made from a hafnium peroxide nitrate starting material and were colorless after synthesis. After 4 days to two weeks the chlorine containing solution becomes colorless as the chlorine reacts to form hypochlorous acid and hydrochloric acid. An additional two to three weeks after the color has faded, the solution solidifies into a soft gel-like glass that does not appear cloudy.

The final pH of the solution is near 12 as measured by litmus paper and does not change as solutions become colorless. Below this pH the hafnium peroxide hydroxide does not fully re-dissolve. The consequence of this is that the solution winds up TMA rich at a ratio between 0.5-0.6 (Hf:TMA).

### **Small Angle X-Ray Scattering**

Small angle X-ray scattering (SAXS) was done on a solution of freshly made TMA hafnia precursor from  $\text{HfOCl}_2$  [Figure 3.2] and the same solution aged after the yellow color dissipated.[Figure 3.3] Comparing the model of the main scattering species in this solution to the  $[\text{Hf}_6(\text{O}_2)_6(\text{OH})_{18}]^{6-}$  cluster shows good agreement in the Guinier region.[Figure 3.2] The radius of gyration ( $R_g$ ) for  $\text{Hf}_6$  cluster was determined to be 3.56 Å while the scattering species in the fresh solution is determined to be 3.48 Å. This is a strong indication that the  $\text{Hf}_6$  cluster is present in the fresh solution. However, SAXS data for the fresh solution shows a dip in the low q region. This is consistent with significant cluster repulsion. The distance between clusters in solution was determined to be 21.99 Å. This repulsion in solution accounts for the increase in longevity of solutions made from this method. The cause for this repulsion is yet unknown, but may be linked to the presence of chlorine that may sit in or near the center of the hexamer preventing hydrogen bonding between species.

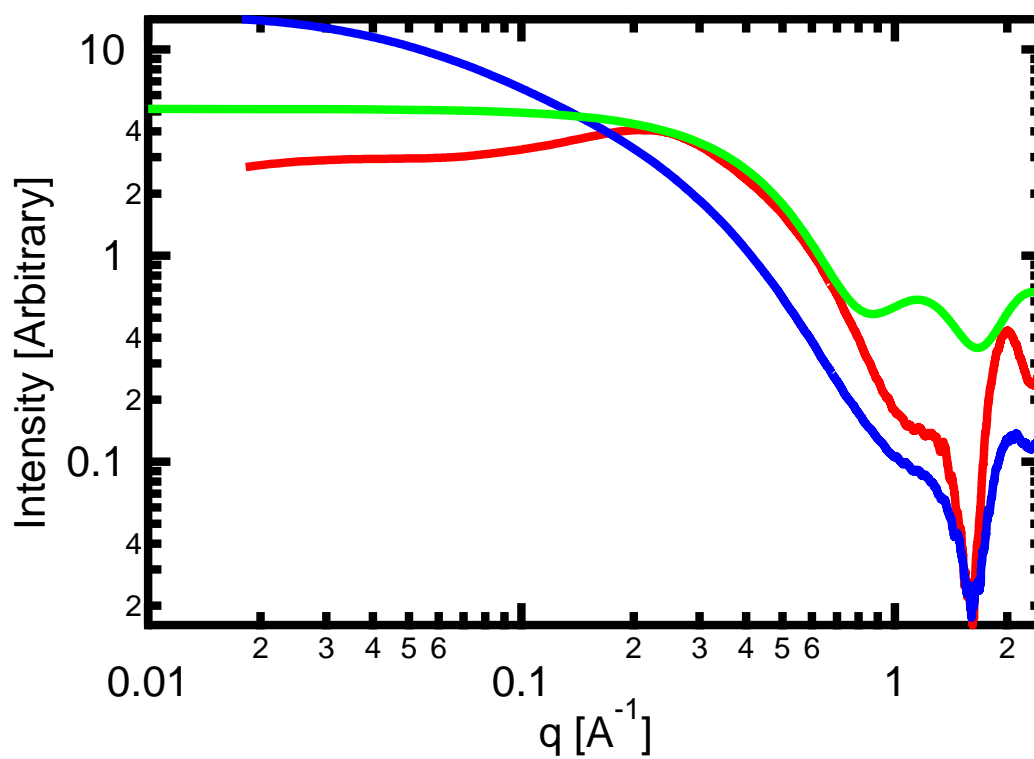


Figure 3.2: SAXS data comparing high pH hafnia precursor (red) with the solution the hafnium hexamer crystallizes from (blue) and the model of the hafnium hexamer (green).

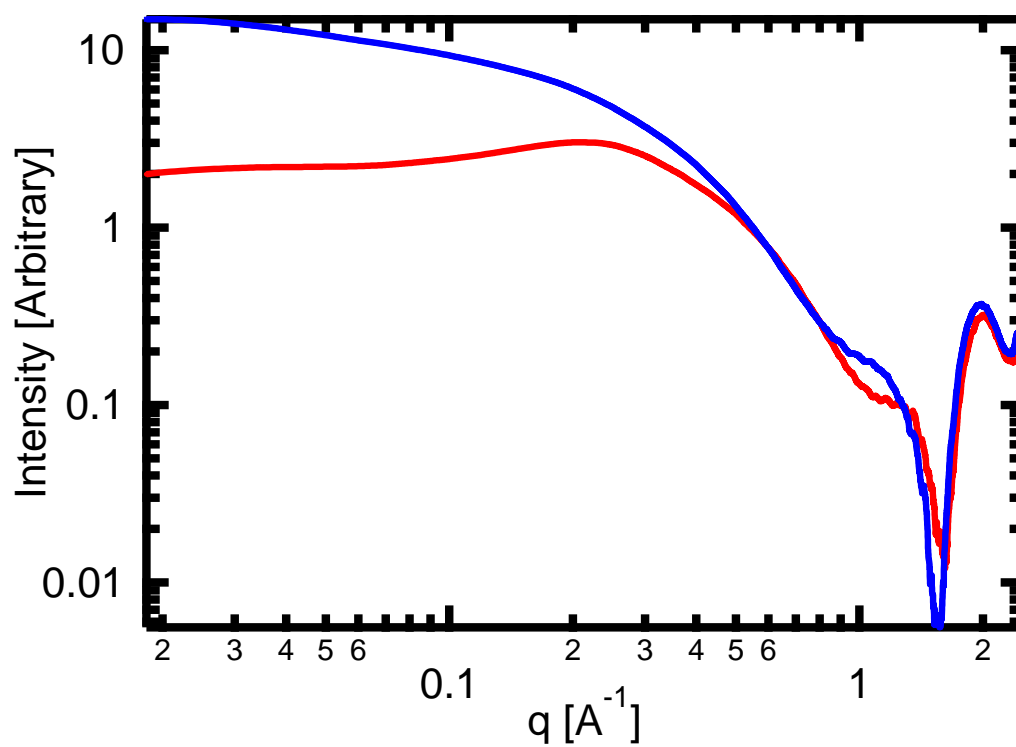


Figure 3.3: SAXS data comparing high pH hafnia precursor freshly made (red) and aged until colorless (blue)

After becoming colorless, SAXS data shows a steep upward slope in the low  $q$  region. This is consistent with aggregation as the solutions begins to gel. Modeling of the scatterer in this solution shows a dramatic increase in  $R_g$  from 3.48 Å to 16.9 Å. This may be associated with the dissolution of elemental chlorine and it being displaced from the hexamer, freeing the cluster to hydrogen bond with other clusters and aggregate.

### **Film Characterization**

Grazing Incidence X-Ray Diffraction was collected on the films over a range of temperatures.[Figure 3.4] Films are deposited amorphous and begin to crystallize at 600 °C. The delay in crystallization compared to films made from lower pH analogs is most likely associated with the structure of the cluster that is present. The lower pH clusters have the well-known tetramer[10] or aggregates of the tetramer, which is essentially a hafnium oxide molecule with all oxygens protonated. In the hexamer, the hafnium species must undergo significant rearrangement to form the stable monoclinic structure despite hafnium being 8 coordinate with oxygen as either hydroxide, water or peroxide in both precursors.

Increasing the annealing temperature to 700 °C does improve crystallinity and peaks associated with the  $11\bar{1}$  and 111 planes shift to lower values of  $2\theta$  by nearly 0.5°. This indicates a slight decrease in density though grain size doesn't change much. Annealing for 24 hours at 700 °C had no discernable differences from annealing at the same temperature for 1 hour. Grain sizes for the three temperatures were calculated using the Scherrer equation and determined to be 3.8 nm, 3.95 nm and 3.9 nm respectively. Comparison of peak intensity also indicate a preferred orientation in the 111 plane.

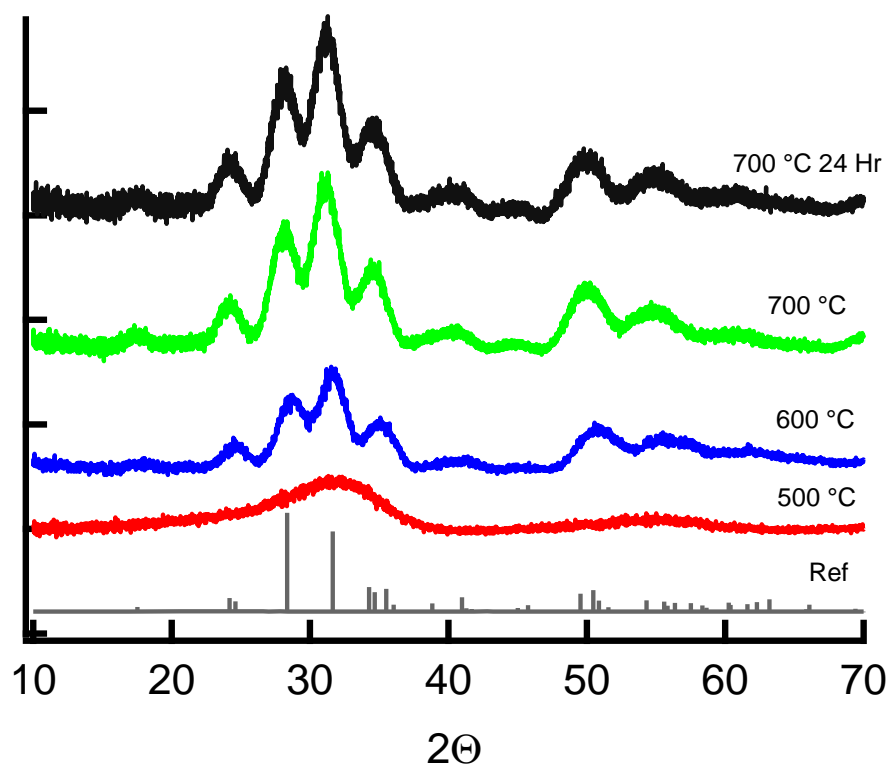


Figure 3.4: Thin film XRD on films made from TMA Hf precursor heated for one hour at 500 °C (red), 600 °C (blue), 700 °C (green), and for 24 hours at 700 °C (black), and a monoclinic reference spectra (gray).

Film thickness was determined by spectroscopic ellipsometry. Films were determined to build thickness at a rate of approximately 16 nm/coat after heating above 500 °C for solutions with a concentration of around 0.3 M. The index of refraction was determined to be 1.7-1.8 at  $\lambda=550$  nm. This is equivalent to films synthesized from previously reported aqueous based methods.[4]

### **Temperature Programmed Desorption**

TPD performed on films spun from the high pH Hf precursor show total loss of water by 450 °C.[Figure 3.5] This is similar to the water profile in the lower pH precursor first reported on by Jiang et al [4] and outlined in chapter 2. As with the lower pH nitrate precursor water comes off from these films as low temperature constitutional water followed by two hydroxide species, the higher of which is more isolated hydroxides.

Figure 3.6 is mass data from TPD tracking the decomposition products for the TMA counter ion. Here we see that TMA decomposes and leaves the film by approximately 425 °C. Though CO<sub>2</sub> is seen at lower temperatures, this could be acquired from ambient conditions. Tracking masses 28, 30, 32, 58, and 59 which correlate to CO, NH<sub>2</sub>CH<sub>2</sub>, CH<sub>3</sub>OH, (CH<sub>3</sub>)<sub>2</sub>(CH<sub>2</sub>)N<sup>+</sup>, and (CH<sub>3</sub>)<sub>3</sub>N respectively, shows that TMA begins to decompose near 200 °C and is completely decomposed by 425 °C. This is consistent with films from other transition metal TMA clusters [14]. Of particular note is the mass 32 spectra which would detect the evolution of molecular oxygen aside from methanol. In the low pH nitrate precursor outlined in chapter 2, molecular oxygen is noted evolving in the range of 600-800 °C. As both of these precursors contain peroxide and are deposited on 100 nm thermally grown oxide, the only difference is the pH of the precursor and presence of

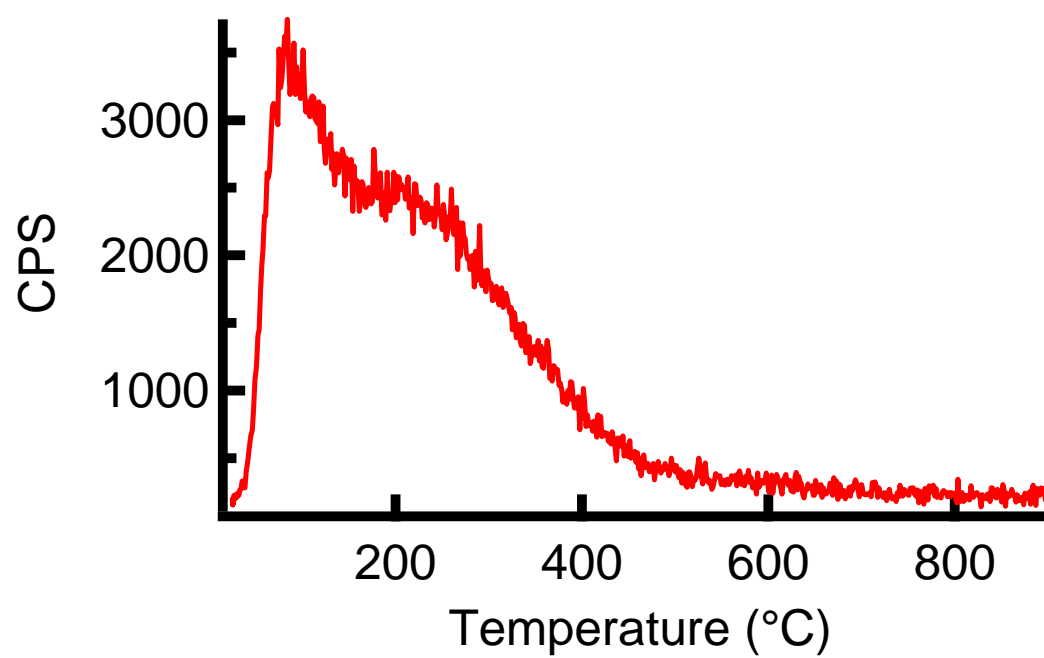


Figure 3.5: TPD showing water (mass 18) loss as a function of temperature.

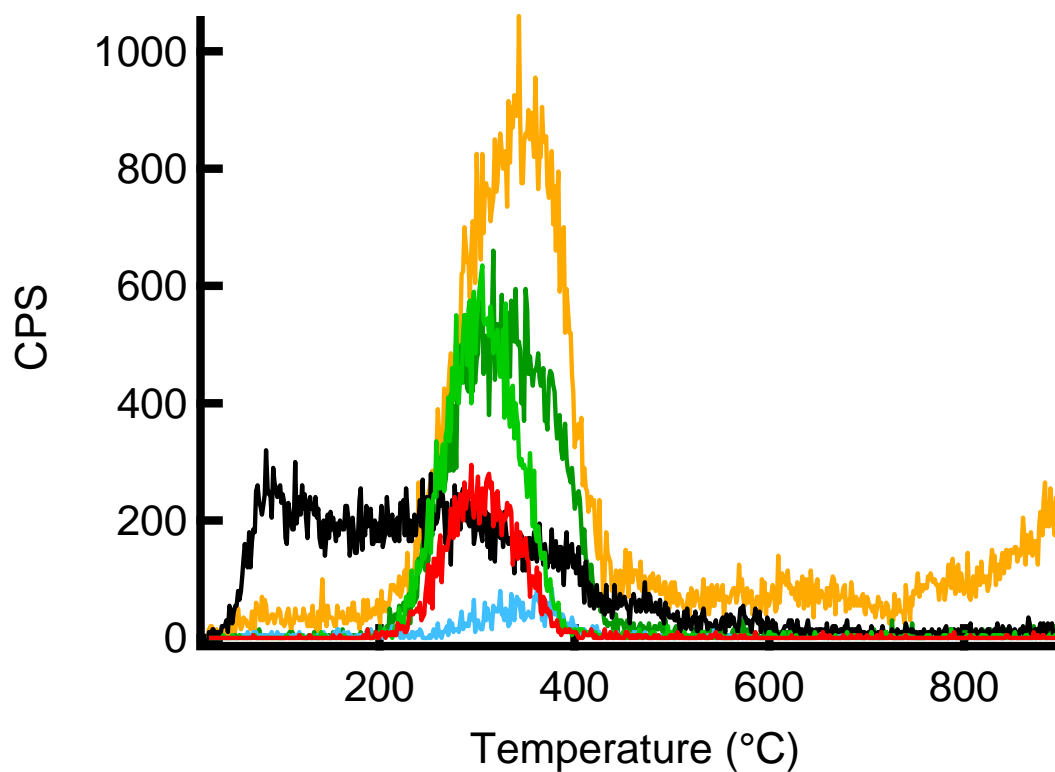


Figure 3.6: TPD response for the decomposition products of TMAH as CO (mass 28, yellow),  $\text{NH}_2\text{CH}_2$  (mass 30, dark green),  $\text{CH}_3\text{OH}$  (mass 32, blue),  $\text{CO}_2$  (mass 44, black),  $(\text{CH}_3)_2(\text{CH}_2)\text{N}^+$  (mass 58, light green), and  $(\text{CH}_3)_3\text{N}$  (mass 59, red).

nitrate. It stands to reason that the lack of high temperature oxygen evolution from these samples stems from a lack of nitrate in the precursor.

Figure 3.7 depicts TPD data for chloride containing products. Mass 35 for chloride and masses 50 and 52 which are seen in mass spectra for methyl chloride show there is a non-trivial amount of residual chloride remaining in the solution from the  $\text{HfOCl}_2$  starting material.

## **Method**

### **Solution Synthesis**

A solution of  $\text{HfOCl}_2$  was prepared by dissolving an amount of 98%  $\text{HfOCl}_2 \cdot 8\text{H}_2\text{O}$  (Alpha Aesar) in 18.2 M $\Omega$  Millipore water to a concentration of 0.968 standardized by calcination. An aliquot of 5 mL was combined with 1.5 mL of 30% hydrogen peroxide (ACS grade Millipore). To the mixture was added  $\sim 1$  M  $\text{NH}_4\text{OH}$  with vigorous shaking until the pH was between 7 and 7.5 as measured by litmus paper. At this point the solution solidified into a powdery wet gel. The gel was then transferred to a Buchner funnel and rinsed several times with high purity Millipore water to remove residual ammonium and chloride. The gel was then transferred to a 20 mL scintillation vial and 2 mL of 25% w/w tetramethylammonium hydroxide (TMAH) (Alpha Aesar) was added. The solution became faintly yellow almost immediately and was allowed to stir over night then filtered. The concentration was measure to be approximately 0.3 M with respect to hafnium via calcination to 800 °C.

A nitrate analog was also prepared using the hafnium peroxide nitrate precursor first reported by Jiang et al [4] in lieu of  $\text{HfOCl}_2$ . Solutions from this method were colorless upon addition of TMAH and were clear after filtration.

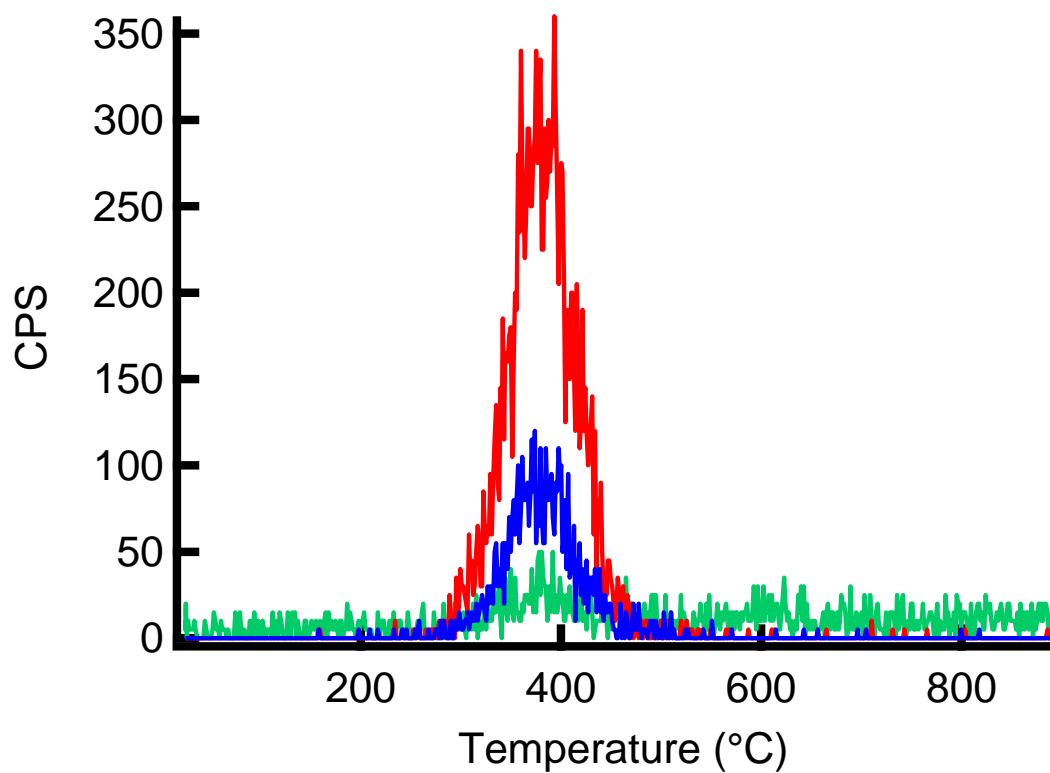


Figure 3.7: TPD data showing the decomposition products of TMAH in the presence of chloride. Signatures are Cl<sup>-</sup> (mass 35, green), and peaks associated with CH<sub>3</sub>Cl at mass 50 (red) and 52 (blue).

## **Film Synthesis**

Silicon wafers with 100 nm thermally grown oxide were prepared for deposition by sonication for 60 minutes at 45 °C in a Contrad 70 bath. Thin films were spin-coated from both solutions at 3000 rpms for 30 seconds. Films were set with a temperature of 260 °C for one minute after each layer and 1 to 3 layers were deposited succinctly. Films from the nitrate derived solution were cloudy and uneven. No further experiments were conducted on them. Films from the chloride derived precursor appeared visually smooth, uniform and defect free. These films were used for temperature programmed desorption analysis and X-ray diffraction.

## **Small Angle X-ray Scattering**

Small Angle X-ray Scattering (SAXS) data were collected on an Anton Paar SAXSess instrument with Cu-K $\alpha$  radiation and slit collimation in the  $q$ -range of  $\sim 0.1\text{--}7\text{ nm}^{-1}$ . Solutions of TMA hafnium peroxide hydroxide were analyzed as synthesized and contained in a reusable 1.5 mm diameter quartz capillary tube for SAXS measurements. Scattering was measured for 30 min. After background subtraction and desmearing, the data were analyzed to determine size, size distribution, structure factors and PDDF (pair distance distribution function) using the IRENA macros [15] within IGOR Pro.

## **Film Characterization**

Grazing Incident X-ray Diffraction (GIXRD) was collected using a Rigaku Ultima IV diffractometer with Cu K $\alpha$  radiation. The incident angle ( $\omega$ ) was set to 0.700° and  $2\theta$  was scanned from 15 to 70°.

Spectroscopic ellipsometry was conducted on a J. A. Woollam M-2000 scanning spectroscopic ellipsometer with a xenon arc lamp source. Data was collected at 55° and

65°. Modeling of the data was conducted using the CompleteEase software and the Cauchy model to determine film thickness and the index of refraction.

### **Temperature Programmed Desorption**

Temperature Programmed Desorption (TPD) was used to determine the decomposition temperature of the thin films in vacuum (and the optimal temperature to anneal in air for complete counter ion removal). TPD measurements were performed on a Hiden Analytical TPD workstation with a quadrupole mass analyzer (3F PIC) to analyze gas-phase products evolved from the thin films upon heating. The measurement was performed under ultra-high vacuum, with the base pressure for the instrument being less than  $5 \times 10^{-9}$  Torr. Spectra were obtained using electron impact ionization with 70 eV ionization potential and 20- $\mu$ A emission current. The thin film samples on  $2.5 \times 2.5 \text{ cm}^2$  samples were cleaved into  $1 \times 1 \text{ cm}^2$  for the TPD analysis.

### **Conclusions**

An alkaline pH hafnium oxide precursor was synthesized and successfully used to make hafnium oxide thin films. The precursor was determined to consist of species that were consistent in size with a previously reported hexameric hafnium peroxide hydroxide cluster. Though a significant amount of impurities persists in the precursor they are easily removed during the annealing process and increase the shelf life of the precursor from hours as with the dissolved pure hexamer to a month. Films also tend to crystalize in the monoclinic structure though have a slight preferred orientation in the 111 plane.

## References

- [1] Lysaght, P. S.; Foran, B.; Bersuker, G.; Peterson, J. J.; Young, C. D.; Majhi, P.; Lee, B. H.; Huff, H. R. *Appl. Phys. Lett.* **2005**, *87*, 85–88.
- [2] Robertson, J. *Reports Prog. Phys.* **2006**, *69*, 327–396.
- [3] Shi, N.; Ramprasad, R. *Appl. Phys. Lett.* **2007**, *91*.
- [4] Jiang, K.; Anderson, J. T.; Hoshino, K.; Li, D.; Wager, J. F.; Keszler, D. a. *Chem. Mater.* **2011**, *23*, 945–952.
- [5] Banger, K. K.; Yamashita, Y.; Mori, K.; Peterson, R. L.; Leedham, T.; Rickard, J.; Sirringhaus, H. *Nat. Mater.* **2011**, *10*, 45–50.
- [6] Bartlett, J.; Woolfrey, J.; Percy, M. *J. Sol-Gel ...* **1994**, *220*, 215–220.
- [7] Tang, J.; Fabbri, J.; Robinson, R. *Chem. Mater.* **2004**, 1336–1342.
- [8] Meyers, S.; Anderson, J.; Hong, D. *Chem. ...* **2007**, 4023–4029.
- [9] Jiang, K.; Meyers, S. *Chem. ...* **2013**, *3*.
- [10] Hagfeldt, C.; Kessler, V.; Persson, I. *R. Soc. Chem.* **2004**.
- [11] Kalaji, a; Soderholm, L. *Chem. Commun. (Camb)*. **2014**, *50*, 997–999.
- [12] Kalaji, A.; Soderholm, L. *Inorg. Chem.* **2014**, *53*, 11252–11260.
- [13] Goberna-Ferron, S.; Park, D. H.; Amador, J. M.; Keszler, D. A.; Nyman, M. *Angew. Chemie - Int. Ed.* **2016**, *55*, 6221–6224.
- [14] Mansergh, R. H.; Fullmer, L. B.; Park, D. H.; Nyman, M.; Keszler, D. A. *Chem. Mater.* **2016**, *28*, 1553–1558.
- [15] Ilavsky, J.; Jemian, P. R. *J. Appl. Crystallogr.* **2009**, *42*, 347–353.

## Chapter 4: Addition of $M^{3+}$ and $M^{4+}$ Cations to Aqueous Hafnia Precursors

### **Introduction**

The addition of other elements into hafnium oxide has been known to stabilize higher energy phases such as the tetragonal [1,2], cubic [3,4], and even orthorhombic [5,6] phases.[Figure 4.1] Traditionally, these types of mixtures are synthesized in the solid state by the diffusion of two oxides at high temperatures. This process can be time consuming and energetically inefficient as in some cases diffusion does not occur until temperatures reach as high as 1500 - 1900 °C. [7,8] To remedy this, solution processing as a means of synthesis is gaining interest as it provides a faster and more energetically efficient means to attain high quality mixed metal oxides.[9,10] Solution processing also provides a means of creating a single source precursory material for direct deposition of thin films through prompt-inorganic-condensation (PIC) thin film processing. [11]. In this contribution the incorporation of yttrium and aluminum into the acidic hafnium peroxide hydroxide nitrate (HafNO<sub>x</sub>) precursor first reported by Kai et al [12] and the incorporation of silicon and germanium into the alkaline pH precursor tetramethylammonium hafnium hydroxide peroxide (TMAHfO<sub>x</sub>) derived from an alkaline hafnium cluster synthesized by Goberna-Ferron et al [13] and outlined in the previous chapter are discussed.

### **Results and Discussion**

#### **Electron Probe Microanalysis (EPMA)**

EPMA was done on the films made from 10% dopant solutions to determine if metal-metal ratios of the precursory solution were reflected in the films. Table 4.1 shows the mole fractions of the precursory solution compared to that of EPMA. In all cases the measured

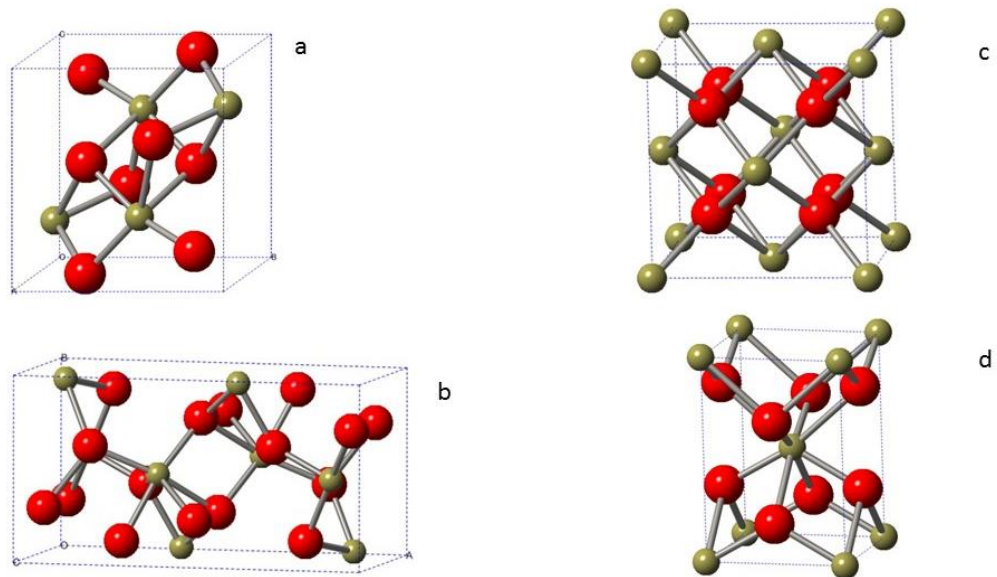


Figure 4.1: Phases of hafnium oxide: a) monoclinic b) orthorhombic c) cubic d) tetragonal

**Table 4.1:** Mole fractions for solutions based on concentrations of precursors and films based on EPMA.

Sample	Metals Present	Mole Fraction in Solution	Mole Fraction in Films
Y:HafNO <sub>x</sub>	Hf : Y	0.9 : 0.1	0.9 : 0.1
Al:HafNO <sub>x</sub>	Hf : Al	0.9 : 0.1	0.89 : 0.11
Ge:TMAHfO <sub>x</sub>	Hf : Ge	0.9 : 0.1	0.89 : 0.11
Si:TMAHfO <sub>x</sub>	Hf : Si	0.9 : 0.1	0.76 : 0.24

ratio of the films closely mirrored that of the precursor solution with the exception of silicon. Silicon was determined to make up 24% of the total metal in the films despite making up only 10% of the metal species in the precursor from which it was spun. There may be a few reasons for this. The first may deal with solubility of the different species. The hafnium species may be inherently more soluble than the silicon species under these conditions and be more likely to spin off in the excess rather than adhere to the surface of the substrate. This could be due to factors such as size of the species in solution, surface energies of the species, or nature of the substrate as this was the only sample to be spun on sapphire for this analysis.

### **Yttrium in HafNO<sub>x</sub>**

Though yttrium has been known to stabilize the cubic phase of hafnium oxide in concentrations as low as 5-6% [6], figure 4.2 shows this not to be the case for the HafNO<sub>x</sub> system. Pure HafNO<sub>x</sub> is seen to crystallize in the monoclinic phase at 500 °C. Mixing 5% Y(NO<sub>3</sub>)<sub>3</sub> into the precursor had no effect on the crystallization temperature but did start to show the growing in of the cubic phase. This can be seen with the appearance of the *c*-111 peak beginning to grow near  $2\theta = 30^\circ$ . As the amount of yttrium is increased to 7%, the cubic phase becomes more prevalent, but the films are still a mixture of monoclinic and cubic phases. At 10% the film is single phase cubic and polycrystalline with no preferred orientation. As the Y<sup>3+</sup> (107 pm)[14] ion is larger than Hf<sup>4+</sup> (83 pm)[14] yttrium stabilizes the cubic phase of hafnium oxide by occupying the same position as a Hf<sup>4+</sup> and creating oxygen vacancies. In this structure yttrium is 6 coordinate and hafnium is 8.

Through implementation of the Scherrer equation [eq 1] the mean grain size is determined to be 17.7 nm. In this equation K is a dimensionless shape factor approaching

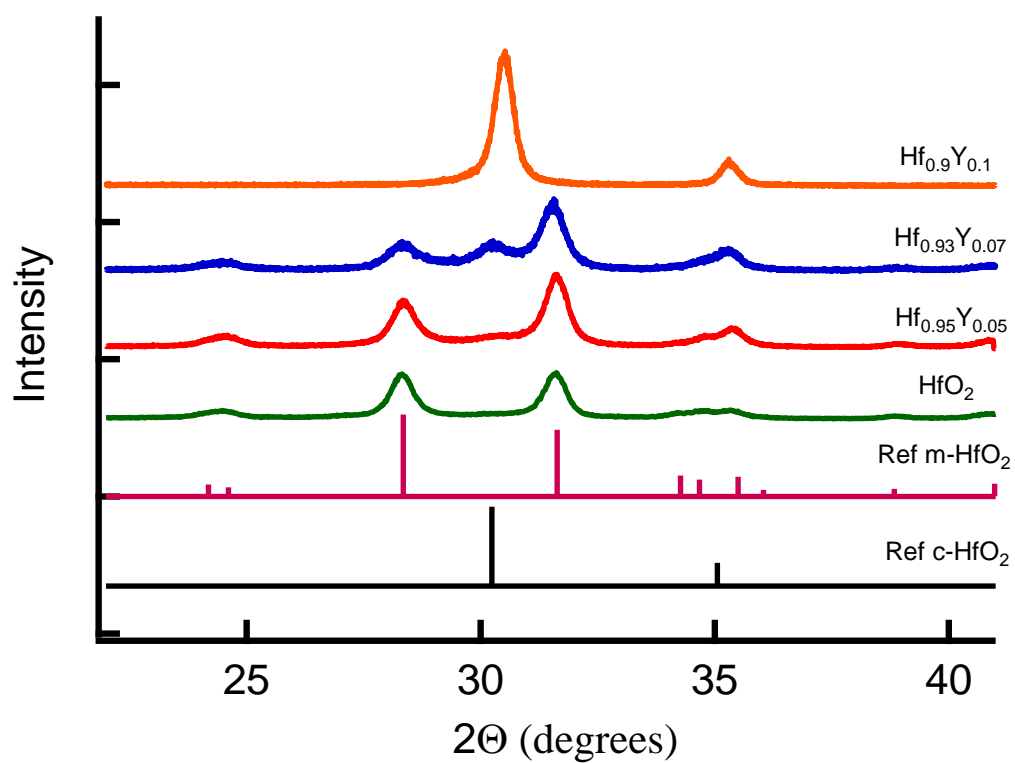


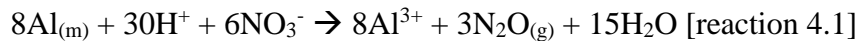
Figure 4.2: Thin film XRD from Cu K $\alpha$  source of hafnia films heated for one hour to 500 °C with yttria added: 0% (green), 5% (red), 7% (blue) and 10% (orange). Reference spectra for cubic hafnia (pink) and monoclinic hafnia (black) have been added.

$K=1$  for spherical grains. The value for the calculations used was  $K=0.94$ . The wavelength of the tool is  $\lambda=0.154$  nm,  $\beta$  is the full width at half max for a given peak and  $\theta$  is the Bragg angle for a given peak. The grain size ( $\tau$ ) was calculated for multiple peaks and the mean size is reported.

$$\tau = \frac{K\lambda}{\beta \cos\theta} \quad [\text{eq 1}]$$

### **Aluminum in HafNOx**

Aluminum and hafnium in equal parts are not known to form a stable single phase material like the other mixtures used in this study. However, in small quantities aluminum has been known to stabilize the cubic phase of hafnium oxide. [15] Aluminum was added to the HafNOx precursor as a metal powder as opposed to a nitrate salt to consume nitrate in the oxidation process of aluminum as outlined in reaction 4.1. This was done to remove nitrate from the precursory solution chemically rather than rely solely on thermal means. Taking what was learned about the Y:HfO<sub>2</sub> system mixtures of Al were done at 7% [Figure 4.3] and 10% [Figure 4.4].



Unlike the Y:HfO<sub>2</sub> system which crystallized at the same temperature as the undoped system, the incorporation of Al delays the onset of crystallization depending on the amount of Al present. At 7%, crystallization occurs at 600 °C in a mixture of cubic and monoclinic. At 10% crystallization is delayed by a further 100 °C to 700 °C and films are single phase cubic. This behavior has been noted before in films of hafnium aluminum oxide deposited by vacuum chamber techniques such as atomic layer deposition though these films are

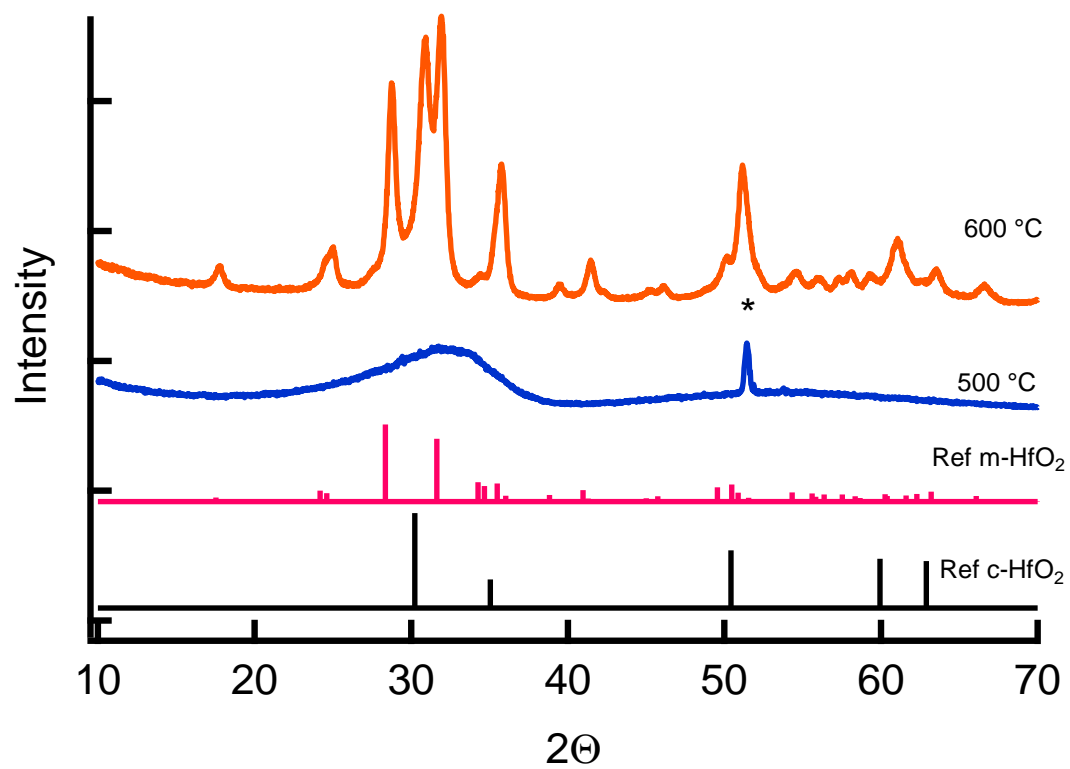


Figure 4.3: Films with 7% Al added to HafNO<sub>x</sub> heated to 500 °C (blue) and 600 °C (orange) for one hour. Reference spectra for monoclinic (pink) and cubic (black) hafnia have been added. Substrate peak denoted with a star.

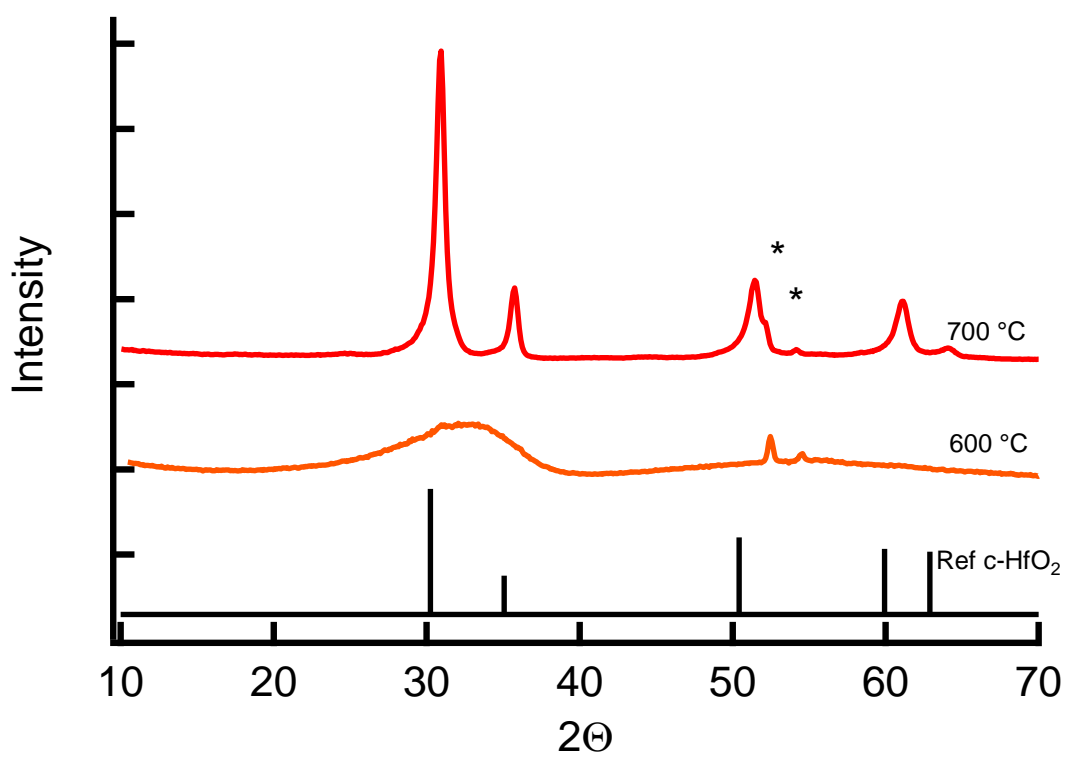


Figure 4.4: Films with 10% Al added to HafNO<sub>x</sub> heated to 600 °C (orange) and 700 °C (red) for one hour. Cubic hafnia reference spectra has been added (black). Substrate peak denoted with a star.

reported to crystallize in an orthorhombic structure. [16] The average grain size for these films was calculated to be 11.95 nm.

Increasing the aluminum above 10% consumes too much nitrate during the oxidation of the aluminum and raises the pH above the window of stability for  $\text{Al}^{3+}$  in solution. In these solutions a small  $\text{Al}(\text{OH})_3$  precipitate forms and solutions gradually turn into a glassy gel over time.

At this time it is not known how aluminum incorporates into the hafnia lattice. As the  $\text{Al}^{3+}$  is much smaller than  $\text{Hf}^{4+}$  and has a lower charge, it is unlikely to displace hafnium in the lattice and more than likely occupies an interstitial site.

### **Silicon in TMA Hafnia Precursor**

Figures 4.5 and 4.6 show the crystallization behavior of films made from the alkaline TMA precursor mixed with silicon at approximately 7% and 10% Si respectively in the mother solution. The high pH precursor has been shown in the previous chapter to crystallize at 600 °C. Much like with aluminum, the incorporation of silicon to higher percentages is shown to delay the crystallization of the films. [Figure 4.6] Films at 7% Si begin to crystallize at the same temperature as the pure precursor, but in a mixture of monoclinic and cubic phases. [Figure 4.5] XRD data in figure 4.6 show that increasing the ratio to 10% delays crystallization by 100 °C to 700 °C and films are single phase cubic. This has also been noted in hafnium silicate films deposited by vacuum chamber techniques. [16] The reason for this delay is most likely associated with the size difference of the silicon to hafnium.  $\text{Hf}^{4+}$  has an ionic radius of 83 pm [14] where  $\text{Si}^{4+}$  has an ionic radius of 40 pm.

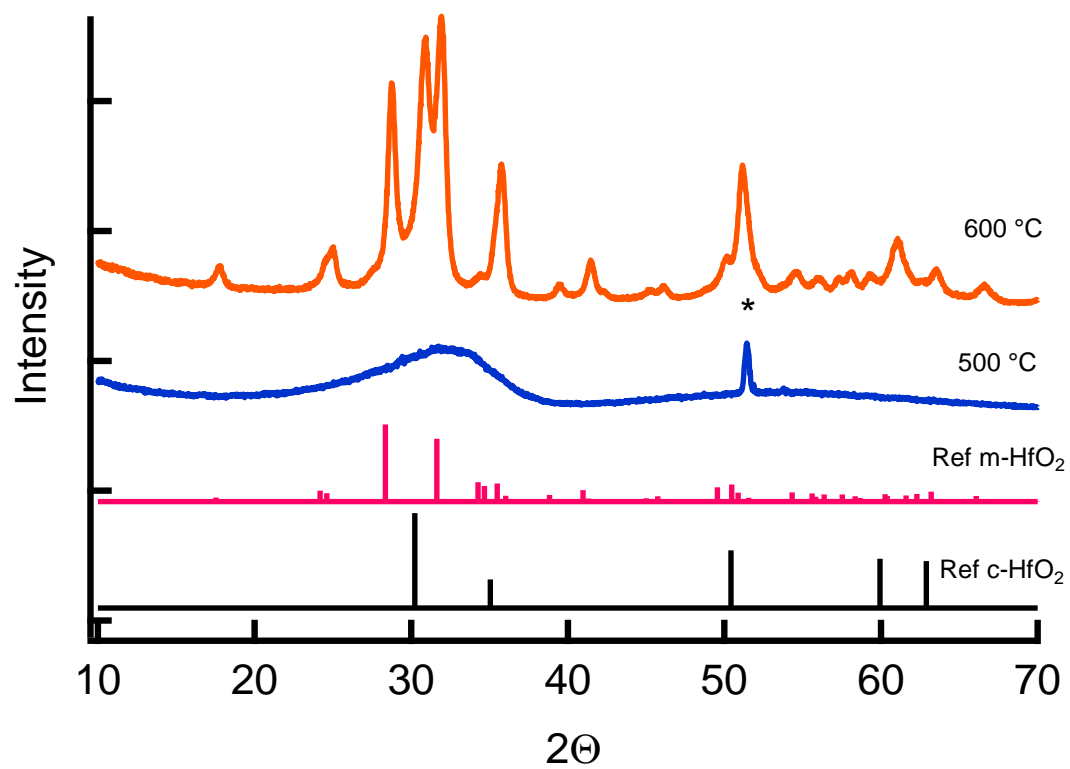


Figure 4.5: Films spun and from TMA Hf precursor with 7% added Si and heated for 1 hour to 500 °C (orange), 600 °C (blue), and 700 °C (red). Substrate peak denoted with a star.

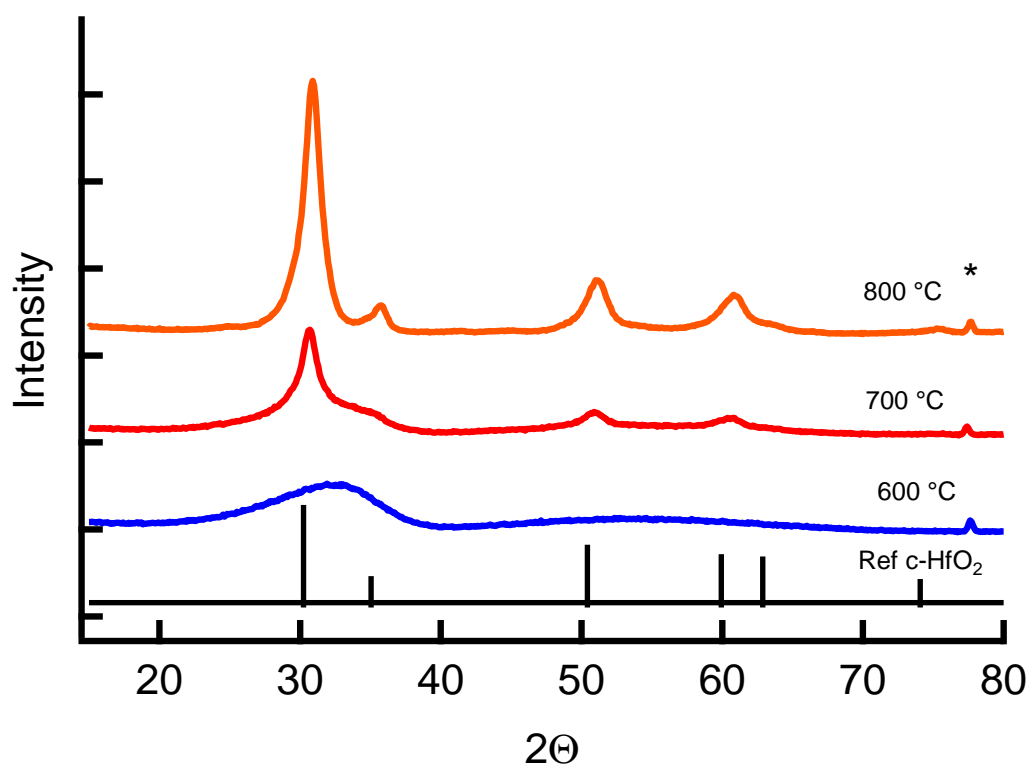


Figure 4.6: Films spun and from TMA Hf precursor with 10% added Si and heated for 1 hour to 600 °C (blue), 700 °C (red) and 800 °C (orange). Reference spectra for cubic hafnia added (black). Substrate peak denoted with a star.

[14] Equal mixtures of hafnium and silicon oxides form a tetragonal hafnium silicate with hafnium CN = 8 and silicon CN = 4. This shows that silicon does not displace hafnium in the lattice but rather occupies tetrahedral interstitial sites. In lower concentrations, like we have here, the incorporation of silicon into these spaces is able to frustrate the lattice enough to stabilize the higher energy phase. Average grain size per the Scherrer equation is 5.95 nm.

### **Germanium in TMA Hafnia Precursor**

Incorporation of  $\text{Ge}^{4+}$  has a similar effect on the behavior of the precursor as  $\text{Si}^{4+}$ . Figure 4.7 shows the crystallization behavior of films spun coated from 10% germanium incorporated into the TMA hafnia precursor. Films crystallize by 700 °C and do so in the cubic structure. Germanium most likely behaves in a similar way as silicon in the lattice as hafnium silicate and hafnium germinate are isostructural. Scherrer calculations show the average crystal grain size for these films is 6.5 nm.

## **Methods**

### **Precursor Synthesis**

The acidic hafnia precursor  $\text{HafNO}_x$  was synthesized in the same manner described by Jiang et al. [12]  $\text{HafNO}_x$  was used to make the aluminum and yttrium containing precursors. For the  $\text{Y:HfO}_2$  films, a 1 M solution of  $\text{Y}(\text{NO}_3)_3$  was used as the source of yttrium. Solutions were made with hafnium to yttrium amounts of 0.95:0.05, 0.93:0.07, and 0.9:0.1.  $\text{Al:HfO}_2$  solutions were made by dissolving 325 mesh aluminum powder in the  $\text{HafNO}_x$  solution at ratios of 0.93:0.07, and 0.9:0.1.

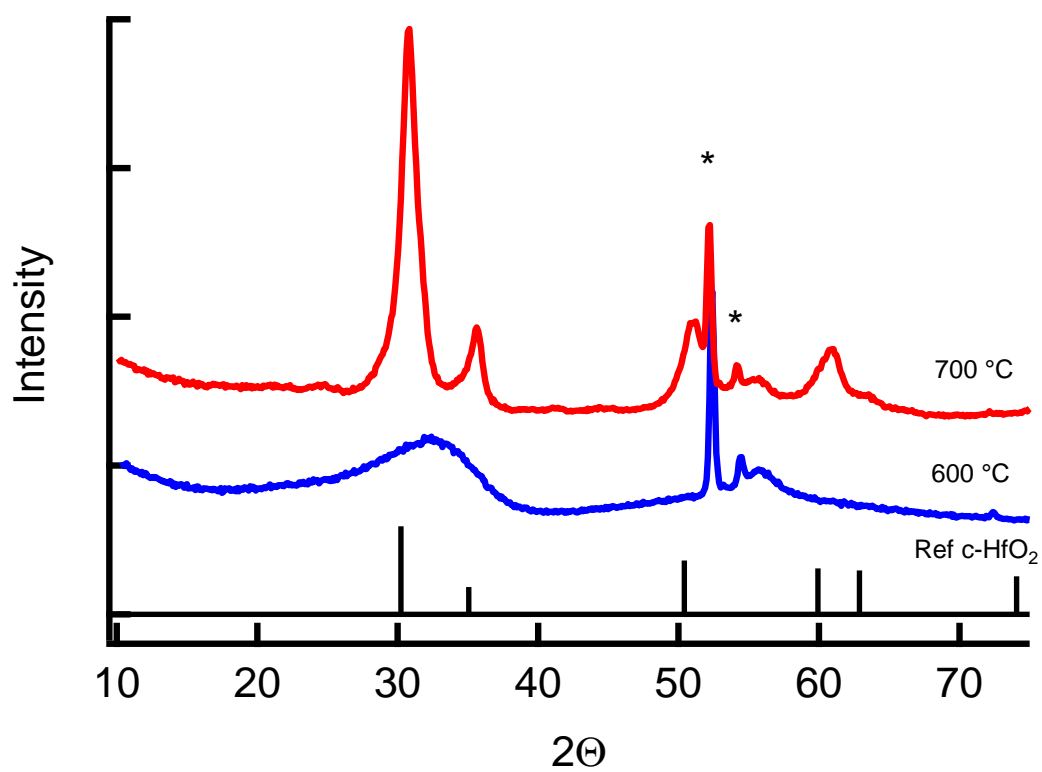


Figure 4.7: Films spun and from TMA Hf precursor with 10% added Ge and heated for 1 hour to 600 °C (blue), 700 °C (red). Reference spectra for cubic hafnia added (black).

Substrate peaks denoted with a star.

The TMA hafnia precursor was synthesized as outlined in chapter 3. Silicon and germanium were added to their respective precursors as either  $\text{SiO}_2$  or  $\text{GeO}_2$  dissolved in 25% v/v TMAH. Solution of 0.93:0.07 and 0.9:0.1 Hf:Si were made and a single solution of 0.9:0.1 Hf:Ge precursor was made for spinning films. All pure solutions were standardized by calcination.

### **Film Synthesis**

The yttrium, aluminum, germanium and 7% silicon films were spin coated on silicon wafers with 100 nm thermally grown oxide measuring 2.5 cm x 2.5 cm. For the 10% Si solution, a 2.5 cm x 2.5 cm wafer sapphire wafer was used as the substrate. This was done for the purposes of conducting EPMA and eliminating interference from the substrate. The silicon substrates were made hydrophilic by sonication in a Contrad 70 bath for 1 hour at 45 °C. The sapphire substrate was made hydrophilic by ashing in an oxygen plasma for 2 minutes using a PE 50. Set bake temperature of 250 °C were used to set the aluminum and yttrium containing films. A set bake temperature of 260 °C was used to set the silicon and germanium containing films. All films were made by laying down 6 coats of their respective precursors to achieve the desired thickness.

### **Electron Probe Micro Analysis**

EPMA was conducted at the CAMCOR facility at the University of Oregon using a Cameca SX 50 equipped with 4 wavelength dispersive spectrometry Bragg spectrometers, a Bruker 10 mm silicon drift detector, and energy dispersive spectrometry detector with hyperspectral mapping that has been optimized for thin film measurements. Data analysis was conducted using in-house developed software.

### **Grazing Incidence X-Ray Diffraction**

Grazing Incident X-ray Diffraction (GIXRD) was collected using a Rigaku Ultima IV diffractometer with Cu K $\alpha$  radiation. The incident angle ( $\omega$ ) was set to 0.700° and  $\theta$  was scanned from 20- 40 ° for the yttrium containing films and 10 - 70° for all other films.

### **Conclusions**

Spin coating precursors from the acidic and alkaline pH ranges were used to incorporate various metals into hafnium oxide PIC processed films. The successful integration of aluminum, yttrium, silicon and germanium into these precursors show the potential diversity of application this technique offers with fewer steps in manufacturing and lower overall energy input compared to traditional solid state techniques. In most cases, the ratios of the metals in the starting precursor represent the ratios of the final film. This work offers an attractive avenue for future work and characterization of these films in the forms of electrical testing and reaction synthesis pathways as well as elucidating any role a selected substrate may play on the resulting composition of the final film.

## References

- [1] Lomenzo, P. D.; Zhao, P.; Takmeel, Q.; Moghaddam, S.; Nishida, T.; Nelson, M.; Fancher, C. M.; Grimley, E. D.; Sang, X.; Lebeau, J. M.; Jones, J. L.; Lomenzo, P. D.; Zhao, P.; Takmeel, Q.; Moghaddam, S.; Nelson, M.; Fancher, C. M.; Grimley, E. D.; Sang, X.; Lebeau, J. M.; Jones, J. L. **2016**, *123*, 0–8.
- [2] Wiemer, C.; Lamagna, L.; Baldovino, S.; Perego, M.; Coulon, P. E.; Salicio, O.; Spiga, S.; Fanciulli, M.; Wiemer, C.; Lamagna, L.; Baldovino, S.; Perego, M. **2015**, *2*, 27–30.
- [3] Müller, J.; Schröder, U.; Böschke, T. S.; Müller, I.; Böttger, U.; Wilde, L.; Sundqvist, J.; Lemberger, M.; Kücher, P.; Mikolajick, T.; Frey, L. *J. Appl. Phys.* **2011**, *110*, 114113.
- [4] Olsen, T.; Schröder, U.; Müller, S.; Krause, a.; Martin, D.; Singh, a.; Müller, J.; Geidel, M.; Mikolajick, T. *Appl. Phys. Lett.* **2012**, *101*.
- [5] He, W.; Zhang, L.; Chan, D. S. H.; Cho, B. J. **2009**, *30*, 623–625.
- [6] Manning, W. R. **1978**, *2–7*.
- [7] Pavunny, S. P.; Sharma, Y.; Kooriyattil, S.; Dugu, S.; Katiyar, R. K.; Scott, J. F.; Katiyar, R. S. *Appl. Phys. Lett.* **2015**, *106*.
- [8] Zhou, G.; Wang, Z.; Zhou, B.; Zhao, Y.; Zhang, G.; Wang, S. *Opt. Mater. (Amst)*. **2013**, *35*, 774–777.
- [9] Kast, M. G.; Cochran, E. A.; Enman, L. J.; Mitchson, G.; Ditto, J.; Siefe, C.; Plassmeyer, P. N.; Greenaway, A. L.; Johnson, D. C.; Page, C. J.; Boettcher, S. W. *J. Am. Chem. Soc.* **2016**, *138*, 16800–16808.
- [10] Banger, K. K.; Yamashita, Y.; Mori, K.; Peterson, R. L.; Leedham, T.; Rickard, J.; Siringhaus, H. *Nat. Mater.* **2011**, *10*, 45–50.
- [11] Smith, S. W.; Wang, W.; Keszler, D. A.; Conley, J. F. *J. Vac. Sci. Technol. A Vacuum, Surfaces, Film.* **2014**, *32*, 41501.
- [12] Jiang, K.; Anderson, J. T.; Hoshino, K.; Li, D.; Wager, J. F.; Keszler, D. a. *Chem. Mater.* **2011**, *23*, 945–952.
- [13] Goberna-Ferron, S.; Park, D. H.; Amador, J. M.; Keszler, D. A.; Nyman, M. *Angew. Chemie - Int. Ed.* **2016**, *55*, 6221–6224.
- [14] Shannon, R. D. *Acta Crystallogr. Sect. A* **1976**, *32*, 751–767.
- [15] Lakiza, S. M.; Tyschenko, J. S.; Lopato, L. M. *J. Eur. Ceram. Soc.* **2011**, *31*, 1285–1291.
- [16] Choi, J. H.; Mao, Y.; Chang, J. P. *Mater. Sci. Eng. R Reports* **2011**, *72*, 97–136.

## Chapter 5

Aqueous Process to Limit Hydration of Thin-Film Inorganic Dielectrics

Cory K. Perkins, Ryan H. Mansergh, Deok-Hie Park, Charith E. Nanayakkara, Juan C. Ramos, **Shawn R. Decker**, Yu Huang, Yves J. Chabal, and Douglas A. Keszler

Published in *Solid State Sciences*, 61, 106-110 September 2016

**Abstract**

Aqueous-processed aluminum oxide phosphate (AlPO) dielectric films were studied to determine how water desorbs and absorbs during heating and cooling. *In-situ* Fourier transform infrared spectroscopy showed a distinct, reversible mono- to bidentate phosphate structural change associated with water loss and uptake. Temperature programmed desorption measurements on a 1- $\mu\text{m}$  thick AlPO film revealed water sorption was inhibited by a aqueous-processed HfO<sub>2</sub> capping film only 11-nm thick, demonstrating solution-deposited HfO<sub>2</sub> functions an effective moisture barrier.

## Introduction

Solvent and solute transport through porous and gel media and interfaces fundamentally affects many materials functions and processes, ranging from the mechanics of biological soft tissues[1] to semiconductor lithography[2,3] and printed electronics.[4] Processing electronic materials with water, either in aqueous solutions or humid environments, presents challenges for residual water removal and passivation, as associated mobile water and hydroxyl protons commonly degrade electronic and device performance.[5–12] Consequently, understanding how to systematically affect and control both liquid and vapor water transport and its antecedent dehydration reactions in gels and solids are essential to produce functional materials from water, especially at low temperatures.

Recently, Anderson and co-workers, employing only aqueous deposition methods, showed the properties of aluminum oxide phosphate (AlPO) dielectric thin films could be enhanced by capping them with an ultrathin HfO<sub>2</sub> layer at low processing temperatures.[13] The HfO<sub>2</sub> cap reduced the relative transient capacitance of a comparable uncapped AlPO film by a factor of 70 in sweeps covering  $\pm 1.5$  MV/cm. Simultaneously, zero-bias hysteresis decreased from 7000 to <100 ppm. These electrical results are consistent with sluggish mobile protons in the uncapped films and their diminution in the capped analogs, which was further confirmed by chemical analysis via forward hydrogen scattering. To improve understanding of this unique process, we examine here dehydration, hydration, and H<sub>2</sub>O transport dynamically via *in-situ* Fourier transform infrared (FTIR) spectroscopy, temperature-programmed desorption (TPD), and transmission electron microscopy (TEM). We find water sorption after film annealing critically affects water and mobile charge concentrations in single layer AlPO films. On heating, AlPO films coated with a thin Hf-

based gel cap readily desorb  $\text{H}_2\text{O}$ . By  $350\text{ }^\circ\text{C}$ , the Hf-based layer converts to a dense, continuous  $\text{HfO}_2$  film, which limits water resorption. Hence, solution deposition produces an effective ultra-thin  $\text{HfO}_2$  moisture barrier at modest process temperatures, rendering performance stability to the AlPO dielectric. The approach may provide highly effective barrier and encapsulation coatings, where integration supports aqueous processing.

## Results and Discussion

Figure 5.1 shows a TEM micrograph of a typical  $\text{HfO}_2$ -AlPO bilayer structure examined in this study. The AlPO film is homogeneous, the AlPO/ $\text{HfO}_2$  interface is sharp, and the  $\text{HfO}_2$  surface is atomically smooth. The films are deposited from aqueous solutions comprising oxo-hydroxo metal clusters accompanied by nitrate counter ions.[14–16] On spin coating, partial condensation occurs to produce continuous films. The AlPO film must be heated to  $230\text{ }^\circ\text{C}$  prior to deposition of the Hf precursor to prevent its dissolution. At this temperature, the films are heavily hydroxylated, and they retain nitrate. We focus here on dehydroxylation and hydroxylation and associated desorption and sorption of water, respectively, for both uncapped and capped AlPO to understand the effects of the  $\text{HfO}_2$  top layer.

### AlPO dehydration

We performed *in-situ* heated FTIR and temperature programmed desorption (TPD) measurements to examine thermal dehydration of AlPO and  $\text{HfO}_2$ -capped AlPO films. Three different films—single layer AlPO and  $\text{HfO}_2$  and bilayer AlPO/ $\text{HfO}_2$ —were investigated. For the FTIR studies, films were heated from  $80$  to  $350\text{ }^\circ\text{C}$  in  $50\text{ }^\circ\text{C}$  increments, holding each temperature for 5 min. In each case, samples were cooled to  $80\text{ }^\circ\text{C}$  prior to data collection. Figure 5.2 shows IR absorption between  $3740$  and  $3000\text{ cm}^{-1}$ ,

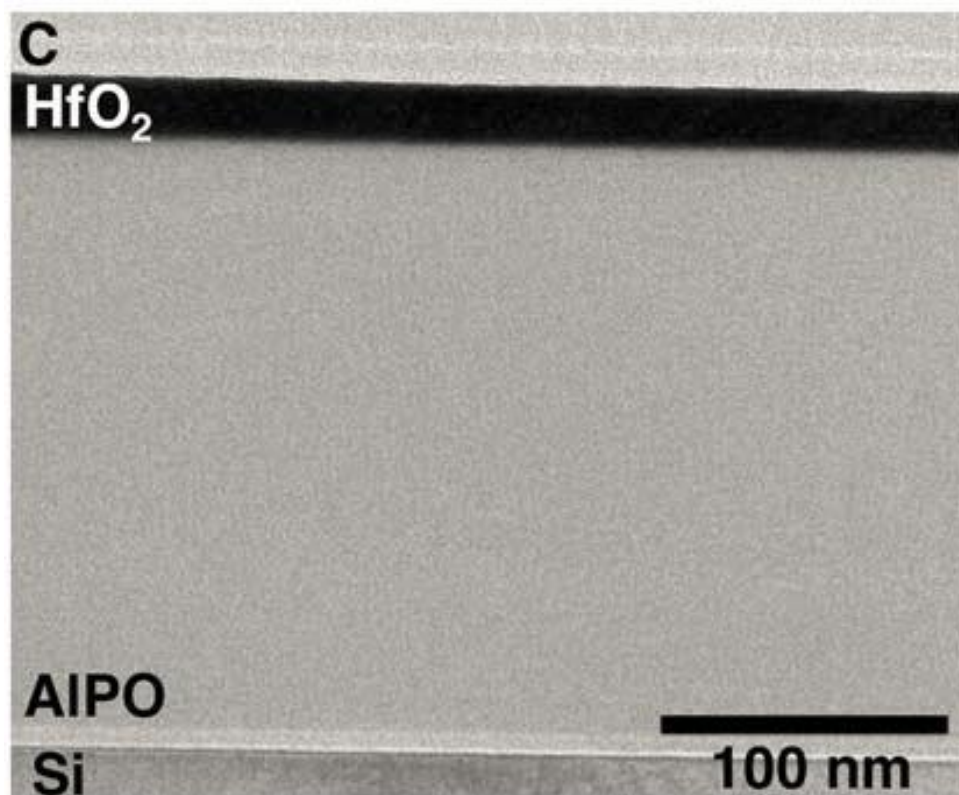
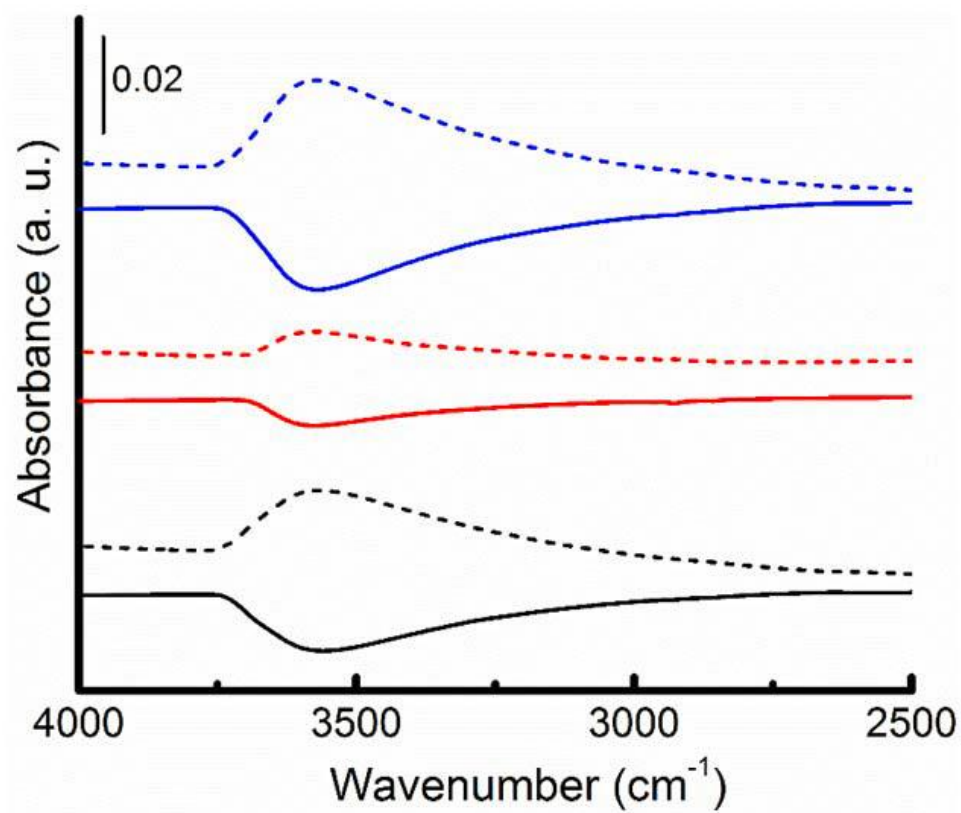


Figure 5.1. TEM micrograph of AlPO-HfO<sub>2</sub> bilayer heated to 550 °C.



**Figure 5.2.** FTIR absorption spectra (dashed lines) for 120-nm AlPO (black), 20-nm HfO<sub>2</sub> (red), and 20-nm HfO<sub>2</sub>-capped 120-nm AlPO (blue) films after stepwise annealing to 350 °C. The solid lines are difference spectra for samples annealed at 80 and 350 °C.

corresponding to the  $\text{-OH/H}_2\text{O}$  vibrational region. The solid lines are difference spectra for samples heated at 80 and 350 °C. The dips represent dehydration. Percent signal loss is determined from the difference in integrated areas of the dashed-line and solid-line spectra; results are summarized in Table 5.1. The single-layer AlPO film loses 84% of its  $\text{-OH}$  signal after annealing to 350 °C. A similar reduction, 90%, occurs for the  $\text{HfO}_2$  and  $\text{HfO}_2$ -capped AlPO films. Figure 5.2 shows IR absorption between 3740 and 3000  $\text{cm}^{-1}$ , corresponding to the  $\text{OH/H}_2\text{O}$  vibrational region. The solid lines are difference spectra for samples heated at 80 and 350 °C. The dips represent dehydration. Percent signal loss is determined from the difference in integrated areas of the dashed-line and solid-line spectra; results are summarized in Table 5.1. The single-layer AlPO film loses 84% of its  $\square\text{OH}$  signal after annealing to 350 °C. A similar reduction, 90%, occurs for the  $\text{HfO}_2$  and  $\text{HfO}_2$ -capped AlPO films.

Figure 5.3 shows  $\text{H}_2\text{O}$  TPD spectra for AlPO and  $\text{HfO}_2$ -capped AlPO films heated to 550 °C. Substantial water evolves below 350 °C; AlPO loses 80% of its initial  $\text{H}_2\text{O}$  content, while  $\text{HfO}_2$ -capped AlPO loses 87%. These results match the FTIR measurements. Figure 5.3(a) shows data for a thick, 46-nm  $\text{HfO}_2$  capping layer, while Figure 5.3(b) shows data for a thin, 11-nm  $\text{HfO}_2$  capping layer. For the thicker capping layer, peak water desorption shifts from 85 to 105 °C, while for the thinner capping layer, peak desorption shifts from 85 to 95 °C, indicating the thicker  $\text{HfO}_2$  layer likely inhibits water desorption from the AlPO layer.

The low-frequency IR region, 2000 – 700  $\text{cm}^{-1}$  (Figure 5.4), corresponding to phosphate vibrational modes, provides clues about structural changes that occur with changing water content. Weak absorption bands at 1011 and 955  $\text{cm}^{-1}$  correspond to asymmetric and

**Table 5.1.** Percent water remaining from integrated area analysis of each absorption spectra between 3740–3000  $\text{cm}^{-1}$  for each film.

Sample	Initial integrated area ( $\text{abs cm}^{-1}$ )	Area after 350 °C anneal ( $\text{abs cm}^{-1}$ )	Water remaining (%)
AlPO	5.10 (+0.41/-0.42)	0.83 (+0.2/-0.21)	16.3 (+2.42/-3.03)
HfO <sub>2</sub>	1.9 (+0.15/-0.16)	0.19 (+0.03/-0.03)	10.0 (+0.73/-0.80)
HfO <sub>2</sub> -AlPO	6.87 (+0.64/-0.65)	0.67 (+0.03/-0.04)	9.75 (+0.73/-0.80)*

\*data corrected for water loss due to HfO<sub>2</sub> layer

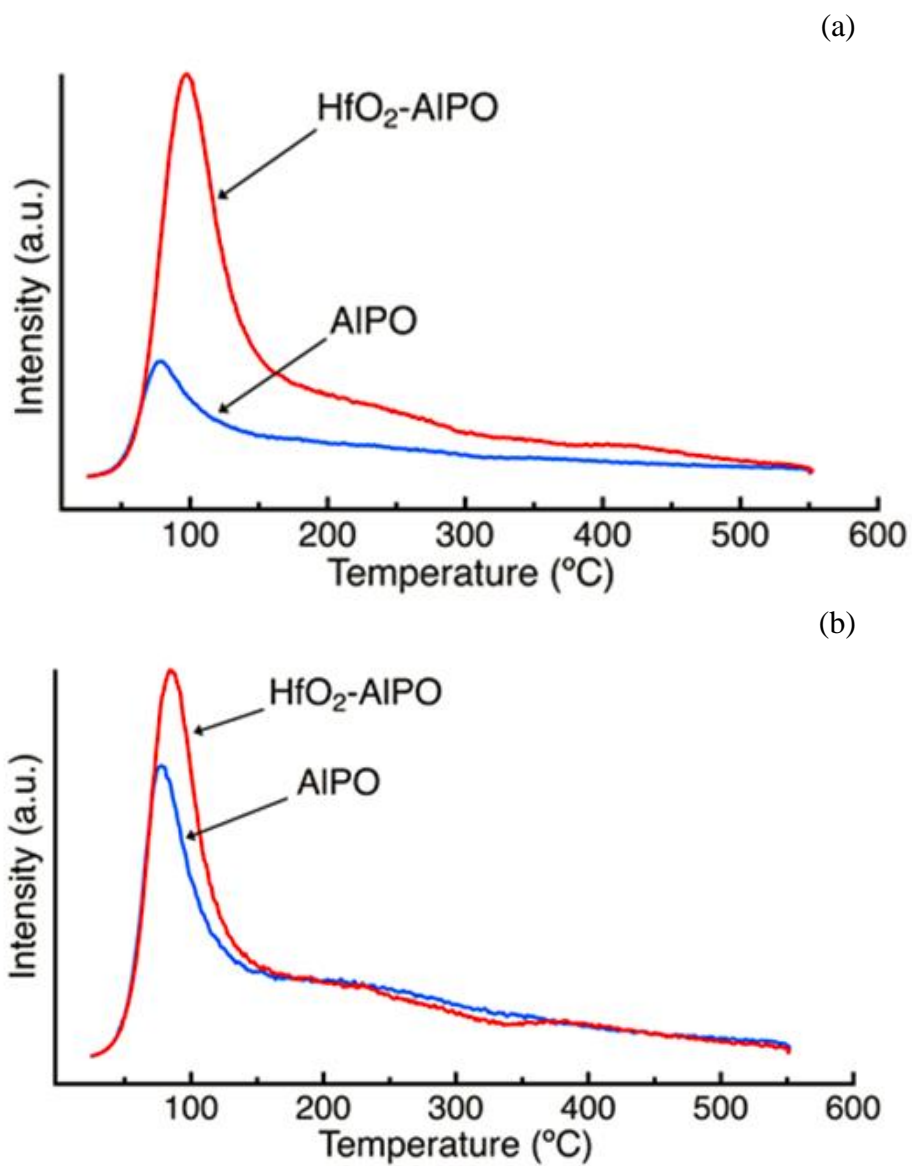


**Figure 5.3.** H<sub>2</sub>O TPD spectra for AlPO (blue) and HfO<sub>2</sub>-AlPO (red) thin films. (a) 46-nm HfO<sub>2</sub> capping layer, (b) 11-nm capping layer.

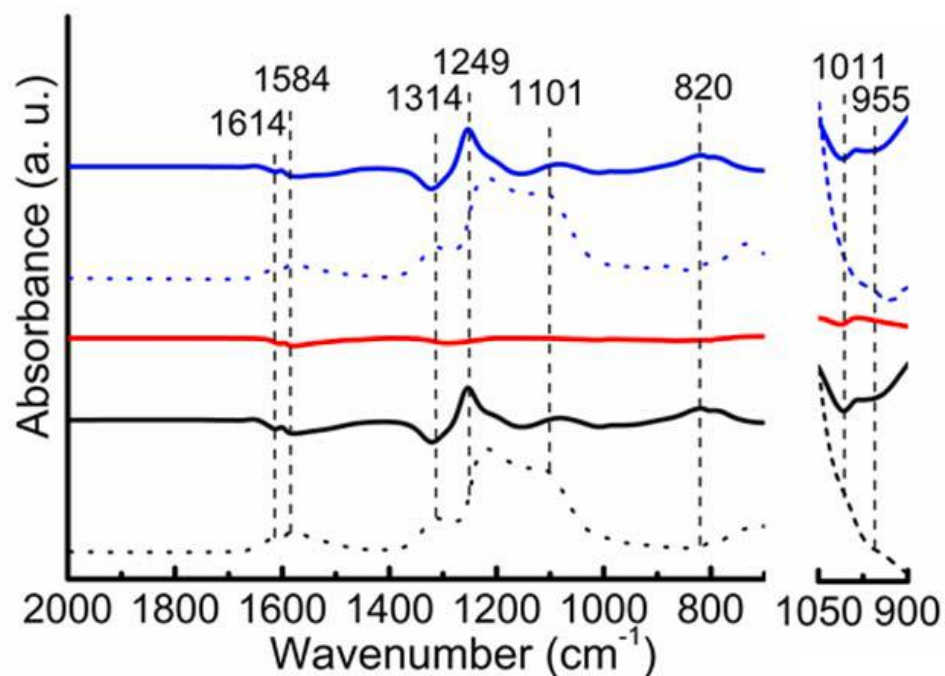
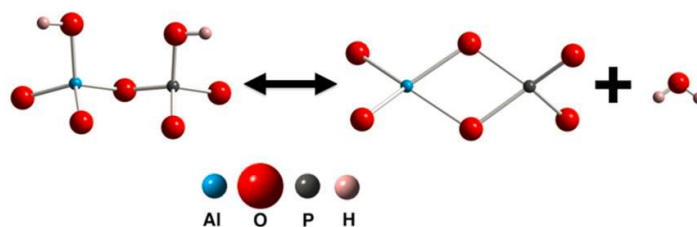


**Figure 5.4.** Dashed lines represent FTIR absorption spectra of 120-nm AlPO (black), 20-nm HfO<sub>2</sub> (red), and 20-nm HfO<sub>2</sub>-capped 120-nm AlPO (blue) after stepwise annealing to 350 °C. Solid lines represent the corresponding difference spectra between 80 and 350 °C. The contributions from the HfO<sub>2</sub> layer in the HfO<sub>2</sub>-capped AlPO film were subtracted from the black spectra. The weak monodentate phosphate stretches at 1011 and 955 cm<sup>-1</sup> are highlighted at right.

symmetric stretch modes of monodentate phosphate binding, while bands at 1249, 1101, and 820  $\text{cm}^{-1}$  correspond to degenerated asymmetric stretch modes and symmetric stretching mode of bidentate phosphate binding.[17] These binding modes are represented in Scheme 5.1. On heating to 350  $^{\circ}\text{C}$ , the difference spectra (Solid lines in Figure 5.4) indicate the concentration of monodentate binding decreases, while bidentate binding increases. This transition is accompanied by water loss (Scheme 5.1), which is observed in the IR spectra and TPD measurements (Figures 5.2 and 5.3). To quantitatively assess this binding change, we integrated the 1249 and 1101  $\text{cm}^{-1}$  bands of single layer AIPO and  $\text{HfO}_2$ -capped AIPO with contributions from the  $\text{HfO}_2$  film removed. Both films exhibit a 16% increase in the bidentate signal on heating to 350  $^{\circ}\text{C}$  (Table 5.2).

Bands at 1614, 1584, and 1314  $\text{cm}^{-1}$  are assigned to the asymmetric stretch modes of bridged bidentate and chelating bidentate nitrates (Figure 5.4). Hence, the negative components in the solid spectra at these frequencies indicate a nitrate loss upon heating.[18]

**Scheme 5.1:** Transformation for the phosphate binding modes upon desorption and resorption of water.



### AIPO Rehydration

After annealing, AIPO films exposed to air resorb water. Figure 5.5 shows  $\text{H}_2\text{O}$  desorption from a 144-nm AIPO film heated to 550  $^{\circ}\text{C}$  in the TPD instrument, then rested on the

**Table 5.2.** Increase in bidentate phosphate absorbance from bands at 1249 and 1101  $\text{cm}^{-1}$ .\*

Sample	Initial integrated area ( $\text{abs cm}^{-1}$ )	Gains in area after anneal ( $\text{abs cm}^{-1}$ )	Water remaining (%)
AlPO	20.55 (+0.45/-0.45)	3.30 (+0.10/-0.10)	16.1 (+0.1/-0.1)
HfO <sub>2</sub> -AlPO	21.35 (+0.25/-0.25)	3.35 (+0.25/-0.25)	15.7 (+1.0/-1.0)

\*contributions from HfO<sub>2</sub> removed

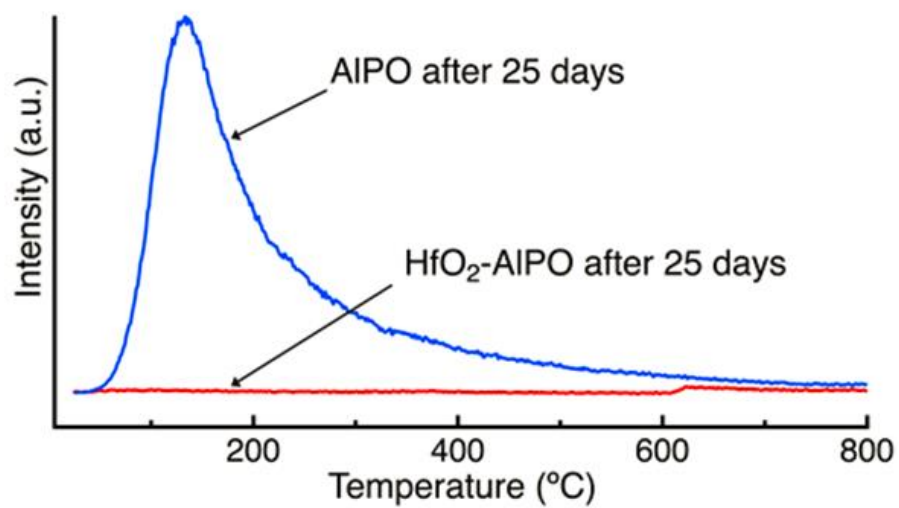
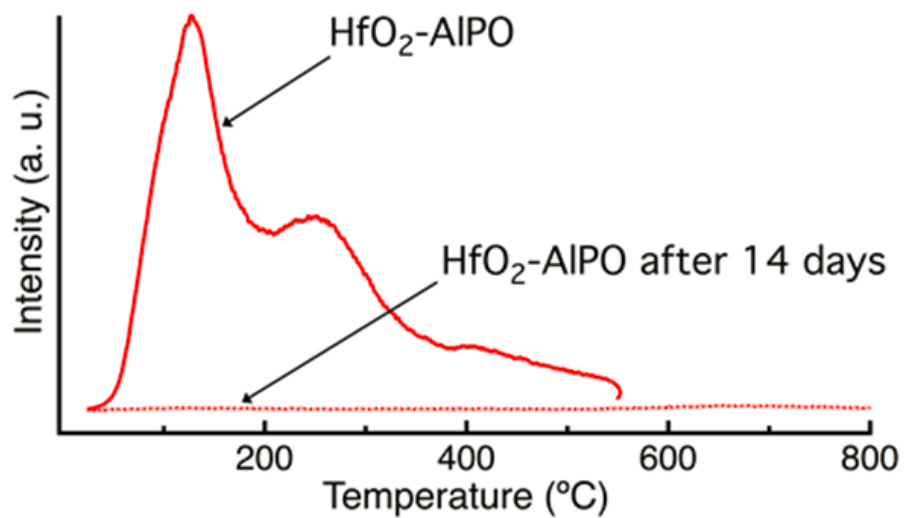


Figure 5.5. H<sub>2</sub>O TPD spectra for AIPO (blue) and HfO<sub>2</sub>-capped AIPO (red) thin films after heating to 550 °C, then resting in air for 25 days.

benchtop for 25 days. The film resorbs 100% of the water desorbed in the initial heating to 550 °C, and the peak desorption signal temperature required to remove the resorbed water increases from 80 to 135 °C, compare Figures 5.3 and 5.5. Capping the AlPO film with a 46-nm thick HfO<sub>2</sub> coating and heating to 550 °C completely prevents water resorption (Figure 5.5, red line).

To establish the barrier efficacy of the HfO<sub>2</sub> cap, we deposited a thick, 1- $\mu$ m AlPO film, then capped it with 11 nm of HfO<sub>2</sub>. Figure 5.6 (solid line) shows the initial water loss on heating to 550 °C. After resting in air for 14 days, the bilayer does not resorb water. Even though the spin-coated HfO<sub>2</sub> cap comprises only 1% of the total bilayer thickness, it functions effectively to block water sorption.

To further explore water resorption, we collected FTIR spectra from films annealed at 350 °C, then exposed to heavy water (D<sub>2</sub>O). At 45 °C, approximately 3 $\times$  more D<sub>2</sub>O resorbs than H<sub>2</sub>O desorbed based on comparison of the decrease of the OH band between 3000 and 3800 cm<sup>-1</sup> and the increase in the OD band between 1800 and 2800 cm<sup>-1</sup>. Coincident with this D<sub>2</sub>O uptake, 95% of the bidentate phosphate converts to monodentate binding. A subsequent anneal at 150 °C decreases the broad OD/D<sub>2</sub>O band by 50% (Figure S1) and increases the bidentate phosphate band by 90%. Hence, the film undergoes a significant, reversible water loss and uptake associated with the phosphate structural change merely upon soft baking. Because the bidentate phosphate binding mode increases dramatically above 150 °C and dominates at 350 °C, water loss and resorption below 150 °C must be dominated by weakly bound molecular H<sub>2</sub>O and its diffusion. Above 150 °C initial water loss occurs by phosphate condensation, and subsequent resorption occurs by phosphate



**Figure 5.6.** H<sub>2</sub>O TPD spectra for a 1- $\mu$ m AlPO film capped by an 11-nm HfO<sub>2</sub> layer. The solid line corresponds to the H<sub>2</sub>O desorption for the HfO<sub>2</sub>-AlPO film after a 230 °C soft bake, and the dashed line corresponds to reabsorption after sitting in air for 14 days.

hydrolysis. This initial hydrolysis creates  $\text{-OH}$  groups and a hygroscopic environment leading to additional  $\text{H}_2\text{O}$  sorption.

### **In-situ Transmission Electron Microscopy**

We performed an *in-situ* TEM experiment to monitor the morphological changes that occur on heating a bilayer of a 143-nm AlPO film and a 31-nm  $\text{HfO}_2$  capping layer. The sample lamella is approximately 100-nm thick, i.e., the thickness orthogonal to the film stacking direction. Figure 5.7 shows micrographs collected at increasing temperatures for samples initially annealed in air at 230 °C for 60 s. At 230 °C, the films remain hydroxylated (Figure 5.3), so water continues to evolve as the films are heated. The effects of this evolution are evident by the inhomogeneous bright contrast areas in the micrographs, both in the spherical areas in the film bulk and at the AlPO- $\text{HfO}_2$  interface. We associate these areas with high  $\text{-OH/H}_2\text{O}$  content in large pores.[19] Because the  $\text{HfO}_2$  film is capped by amorphous C and Cr, water is unable to diffuse through the  $\text{HfO}_2$  layer and desorb. Nevertheless, water collects at the AlPO- $\text{HfO}_2$  interface, then likely diffuses orthogonal to the image plane and evolves from the film.

We conducted an additional *in-situ* TEM experiment with a thinner  $\text{HfO}_2$  cap to determine if water accumulation would be significant at the  $\text{HfO}_2$ -AlPO interface. The AlPO film thickness was held constant at 140 nm, while the  $\text{HfO}_2$ -film thickness was reduced to 11 nm. (Figure 5.8a). Upon heating (Figures 5.8b & 5.8c), the thinner film did not show the same water accumulation effect observed with a 31-nm thick  $\text{HfO}_2$ -capping layer. The only observed inhomogeneities were the dynamic, spherical features, which continued to evolve as water desorbed. The thinner  $\text{HfO}_2$  film likely enables the facile

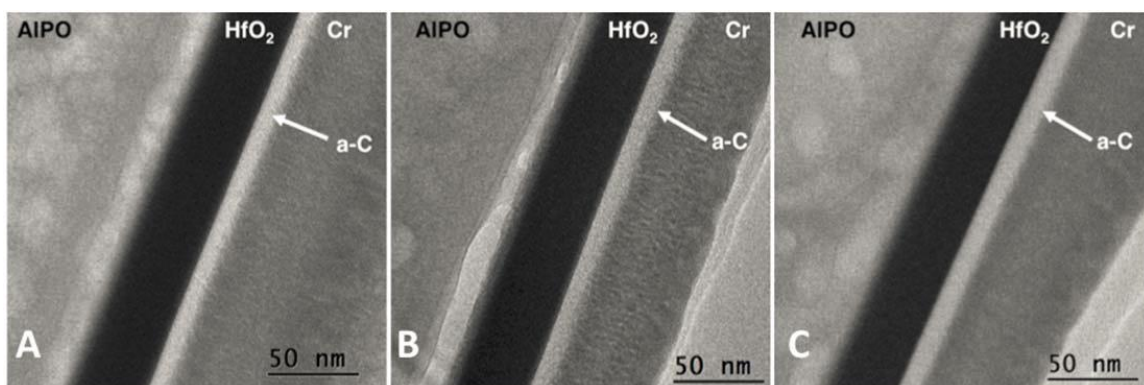


**Figure 5.7.** *In-situ* heated TEM micrographs of a 143-nm AlPO film capped by 31 nm of HfO<sub>2</sub>. The (A) 150-200 °C, (B) 250 °C, and (C) 400 °C.

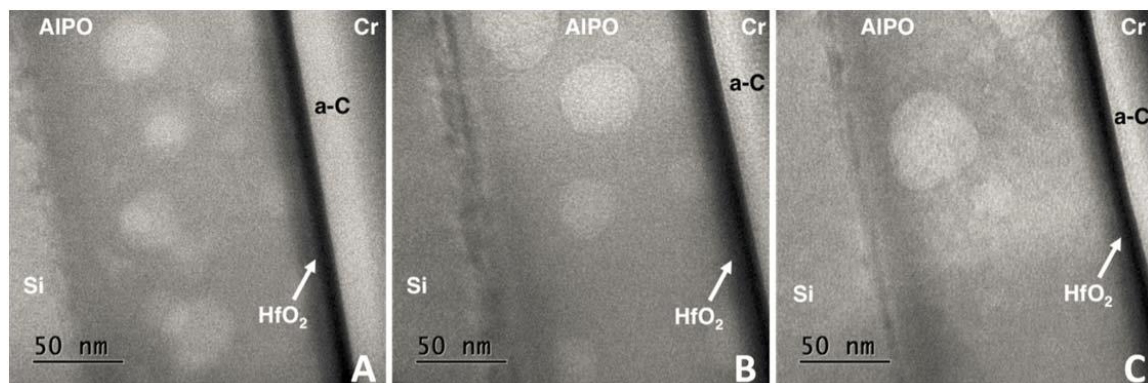


**Figure 5.8.** TEM micrographs of 140-nm AlPO film capped by 11-nm HfO<sub>2</sub> films. (A) 150 °C (B) 200 °C, and (C) 400 °C.

diffusion of water through the capping layer during the initial soft bake, thereby limiting water accumulation at the interface. Conversely, the thick capping layer hinders AIPO dehydration. The TPD spectra support this observation as the thick AIPO-HfO<sub>2</sub> bilayer shows the peak water desorption at 105 °C, compared to 95 °C for the thinner HfO<sub>2</sub> cap. With the thinner cap, the image contrast indicates possible interdiffusion at the AIPO-HfO<sub>2</sub> interface, which is largely hidden by the higher retained water content in the bilayer with the thicker cap. This interdiffusion may be promoted by the water-trapping effects of the amorphous carbon and Cr cover layers, as it is not evident in Figure 5.1.

## Conclusions

*In-situ* IR vibrational analysis and TPD measurements reveal AIPO films reversibly desorb and absorb water. Condensation involving hydrogen phosphate and hydrolysis involving phosphate regulate these processes. From in-situ TEM studies, film dehydration is initially characterized by accumulation of OH/H<sub>2</sub>O-rich droplets. Over time and with heating, these droplets dissipate by evolving H<sub>2</sub>O. Capping AIPO films with a thin HfO<sub>2</sub> aqueous precursor barely affects AIPO dehydration. Conversely, the thin HfO<sub>2</sub> film formed on annealing the bilayer effectively suppresses water resorption under conditions that uncapped AIPO films sorb copious amounts of water. Solution-processed HfO<sub>2</sub> thus enables the fabrication of an effective water-blocking layer, even when it comprises only 1% of underlayer thickness. Generally, the approach holds promise for realizing new high-performance barrier coatings, corrosion inhibitors, and encapsulants, where integration may be aided by aqueous processing.

## Experimental Section

Solution precursor synthesis has been described previously.<sup>14,15</sup> The AlPO solution was prepared with a 0.85-M Al concentration and an aluminum:phosphorus ratio of 1:0.6. The water-based peroxide HfO<sub>2</sub> precursor was prepared in two different concentrations—0.250 and 0.124 M for the thick and thinner films, respectively.

Prior to thin-film deposition, all substrates were cleaned by sonication in a deionized water bath. Following this cleaning, they were treated in a low-energy O<sub>2</sub> plasma to create a clean, hydrophilic surface. The films were deposited onto either *p*-type Si (for the TEM experiment) or 100-nm thermally grown SiO<sub>2</sub>/Si (for TPD-MS). Films were deposited by spin coating the aqueous precursors at 3000 rpm for 30 s. Each coat was soft baked at 230 °C for 1 min prior to deposition of additional layers. In each case, two coats of 0.85 M AlPO were deposited, resulting in film thicknesses of 140–150 nm. For the thicker HfO<sub>2</sub> films, three coats of the 0.250 M HfO<sub>2</sub> precursor were deposited to produce a film thickness near 45 nm. One coat of the 0.124 M solution was used to deposit the 11-nm HfO<sub>2</sub>-capping layer.

Spectroscopic ellipsometry data were collected with a J. A. Woollam M-2000 spectroscopic ellipsometer to determine film thickness. Film thicknesses of the HfO<sub>2</sub> and AlPO layers were determined with a Cauchy model via the CompleteEASE software package.[20]

*In-situ* FTIR spectroscopy studies were carried out using a nitrogen-purged home-built ALD reactor with a Thermo Nicolet 6700 infrared spectrometer equipped with a liquid nitrogen-cooled broadband mercury cadmium telluride (MCT-B) detector.[21] A single-pass transmission at Brewster incidence (~74°) was used to minimize the substrate phonon

absorption in the low frequency region ( $<1000\text{ cm}^{-1}$ ) and to increase detection sensitivity of all film chemical components. After heating in flowing  $\text{N}_2(\text{g})$ , the films were cooled to  $80\text{ }^\circ\text{C}$  for data collection. A K-type thermocouple spot-welded onto a tantalum clip was attached at the center of the long edge of the substrate to monitor the sample temperature during analysis. Two gate valves were used to isolate the KBr windows used in the analysis chamber for IR transmission during annealing.

FTIR data analysis involved two parts. To measure water (hydroxide) content in the films, the relative absorbance was integrated from the spectra; all films were referenced to a spectrum of a clean  $\text{SiO}_2/\text{Si}$  (100) wafer. The amount of water desorbed after annealing was calculated by measuring the integrated area in the range of  $3740 - 3000\text{ cm}^{-1}$  of the absorbance spectra. The baselines of the spectra before and after annealing were not consistent; therefore, absorbance values at  $3740$  and  $3000\text{ cm}^{-1}$  were assumed as the baseline. Similar to the water content, the initial and final amounts of phosphate binding after the  $350\text{ }^\circ\text{C}$  anneal were quantified by integrating the area between  $1300$  and  $1250\text{ cm}^{-1}$ . To quantify the phosphate content of the 20-nm  $\text{HfO}_2$ -capped AlPO film, changes from the  $\text{HfO}_2$ -cap were subtracted from the spectrum using the band at  $1576\text{ cm}^{-1}$  as the reference.

The TPD study was performed on a Hiden Analytical TPD Workstation with a quadrupole mass analyzer (3F PIC) to monitor gas-phase products released from the thin films upon heating. The measurement was performed under ultra-high vacuum with a base pressure  $< 5 \times 10^{-9}$  Torr. Mass spectra were obtained using electron impact ionization with  $70\text{ eV}$  ionization potential and  $20\text{-}\mu\text{A}$  emission current. The  $m/z$  of 18 was selected to monitor of water desorption. Thin films on  $2.54 \times 2.54\text{ cm}^2$  substrates were cleaved into 1

x 1 cm<sup>2</sup> for the TPD analysis. To test the amount of water in each of the samples, the films were heated from room temperature to 550 °C with a ramp rate of 30 °C/min and a dwell time of 5 min at 550 °C. The samples were then allowed to sit open in air in preparations for tests of water resorption and then ran TPD again heating to 900 °C. The area under the peaks were integrated to quantify the mass responses for each sample.

*In-situ* TEM experiments were performed using an FEI Titan 80-200 TEM/STEM transmission electron microscope operating at 200 kV. Carbon and chromium coatings were deposited on HfO<sub>2</sub>/AlPO bilayers for protection and to enhance sample contrast. After adding a final protective layer of platinum *in-situ*, a thin cross section of the HfO<sub>2</sub>-capped AlPO film was selectively machined using the focused gallium ion beam and an FEI Quanta 3D SEM. The lamella was welded to a copper TEM grid and thinned to approximately 100 nm using the ion beam. The films were heated *in-situ* with a ramp rate of 20 °C/min. Micrographs were collected at 50 °C increments to study effects of heating on the films.

### **Author Information**

#### **Corresponding Author**

\*Douglas.Keszler@oregonstate.edu

#### **Author Contributions**

All authors have given approval to the final version of the manuscript.

#### **Funding Sources**

This material is based on work in the Center for Sustainable Materials Chemistry supported by the U.S. National Science Foundation under Grant CHE-1102637.

### **Acknowledgments**

The authors thank P. Eschbach and T. Sawyer for assistance with SEM and TEM imaging in the OSU Electron Microscope Facility. The TEM was acquired with funds from the M.J. Murdock Charitable Trust, the Oregon Nanoscience and Microtechnologies Institute, and the U.S. National Science Foundation (Grant No. 1040588).

## References

- [1] Ateshian, G. A.; Maas, S.; Weiss, J. A. *J. Biomech.* **2012**, *45* (6), 1023–1027.
- [2] Moreau, W. M. *Semiconductor Lithography: Principles, Practices, and Materials*; Plenum Publishing Corp.: emiconductor Lithography: Principles and Materials., 1988.
- [3] Oleksak, R. P.; Ruther, R. E.; Luo, F.; Fairley, K. C.; Decker, S. R.; Stickle, W. F.; Johnson, D. W.; Garfunkel, E. L.; Herman, G. S.; Keszler, D. A. *ACS Appl. Mater. Interfaces* **2014**, *6* (4), 2917–2921.
- [4] Mitzi, D. B. *J. Mater. Chem.* **2004**, *14* (15), 2355–2365.
- [5] Park, J. S.; Jeong, J. K.; Chung, H. J.; Mo, Y. G.; Kim, H. D. *Appl. Phys. Lett.* **2008**, *92* (7), 34–36.
- [6] Park, J. H.; Kim, K.; Yoo, Y. B.; Park, S. Y.; Lim, K.-H.; Lee, K. H.; Baik, H. K.; Kim, Y. S. *J. Mater. Chem. C* **2013**, *1* (43), 7166–7174.
- [7] Houssa, M.; Pourtois, G.; Heyns, M. M.; Stesmans, a. *J. Phys. Condens. Matter* **2005**, *17* (21), S2075–S2088.
- [8] Schneider, J. M.; Anders, A.; Hjorvarsson, B.; Petrov, I.; Macak, K.; Helmersson, U.; Sundgren, J.-E. *Appl. Phys. Lett.* **1999**, *74* (2), 200–202.
- [9] Guha, S.; Yang, J.; Williamson, D. L.; Lubianiker, Y.; Cohen, J. D.; Mahan, a. H. *Appl. Phys. Lett.* **1999**, *74* (13), 1860.
- [10] Jun, T.; Song, K.; Jeong, Y.; Woo, K.; Kim, D.; Bae, C.; Moon, J. *J. Mater. Chem.* **2011**, *21* (4), 1102–1108.
- [11] Smith, S. W.; Wang, W.; Keszler, D. A.; Conley, J. F. *J. Vac. Sci. Technol. A Vacuum, Surfaces, Film.* **2014**, *32* (4), 041501.
- [12] Jeong, W. H.; Kim, D. L.; Kim, H. J. *ACS Appl. Mater. Interfaces* **2013**, *5* (18), 9051–9056.
- [13] Anderson, J. T.; Wang, W.; Jiang, K.; Gustafsson, T.; Xu, C.; Gafunkel, E. L.; Keszler, D. A. *ACS Sustain. Chem. Eng.* **2015**, *3* (6), 1081–1085.
- [14] Meyers, S. T.; Anderson, J. T.; Hong, D.; Hung, C. M.; Wager, J. F.; Keszler, D. A. *Chem. Mater.* **2007**, *19* (16), 4023–4029.
- [15] Jiang, K.; Anderson, J. T.; Hoshino, K.; Li, D.; Wager, J. F.; Keszler, D. A. *Chem. Mater.* **2011**, *23* (4), 945–952.
- [16] Jiang, K.; Meyers, S. T.; Anderson, M. D.; Johnson, D. C.; Keszler, D. A. *Chem. Mater.* **2013**, *25* (2), 210–214.
- [17] Arai, Y.; Sparks, D. L. *J. Colloid Interface Sci.* **2001**, *241* (2), 317–326.
- [18] Goodman, A. L.; Bernard, E. T.; Grassian, V. H. *J. Phys. Chem. A* **2001**, *105* (26), 6443–6457.
- [19] Brinker, C. J.; Sherrer, G. W. *Sol–Gel Science*; Academic Press: New York, 1990.
- [20] Hale, J.; Johs, B. *CompleteEase*; J. A. Wollam: Lincoln, NE, 2012.
- [21] Kwon, J.; Dai, M.; Halls, M. D.; Langereis, E.; Chabal, Y. J.; Gordon, R. G. *J. Phys. Chem. C* **2009**, *113* (2), 654–660.

## Chapter 6

Patterning Chemistry of HafSO<sub>x</sub> Photoresist

Jenn M. Amador, **Shawn R. Decker**, Stefan E. Lucchini, Rose E. Ruther, and Douglas A. Keszler

Published in *Proc. of SPIE* Vol. 9051, 2014

**ABSTRACT**

A combination of ICP-OES, titration, and Raman spectroscopy was used to determine the ratio of peroxide to hafnium in the inorganic photoresist  $\text{HfSO}_x$ . By using ICP-OES to determine the hafnium concentration and titration with permanganate to determine peroxide in a solution of dissolved films, the  $\text{Hf}:\text{O}_2^{2-}$  ratio was found to be approximately 2:1 in the films. From Raman measurements on precursor solutions, it was determined that Hf bound peroxide saturated at this level. Film insolubility is induced through loss of approximately 75% of bound peroxide following exposure to a 30-keV electron beam.

## Introduction

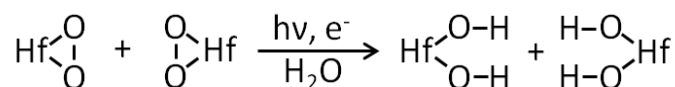
In this contribution, we report results on the determination of the peroxide concentration in thin films of the radiation-sensitive resist  $\text{Hf}(\text{OH})_{4-2x-2y}(\text{O}_2)_x(\text{SO}_4)_y \cdot q\text{H}_2\text{O}$  commonly known as HafSOx. This information is needed to develop an understanding of the basic mechanism of lithographic patterning and the intrinsic performance potential of the material. HafSOx free of peroxide was originally investigated as a thin-film high- $\kappa$  dielectric.[1] The addition of peroxide renders the material sensitive to radiation, yielding a photoresist that can be densely patterned at feature sizes smaller than 10 nm.[2-5]

HafSOx films are deposited by spin coating from acidic aqueous solutions. Such solutions are known to contain small nanosized hydroxo clusters containing approximately four Hf atoms. On deposition and heating, these clusters can condense via dehydration (scheme 6.1) to form rigid gel films. Following extensive dehydration, the films become



Scheme 6.1

insoluble in common resist developers such as TMAH. In HafSOx, this condensation process is inhibited by the binding of peroxide to Hf. As shown in scheme 6.2, peroxide



Scheme 6.2

decomposition can be induced by high-energy light or electrons. This radiation switch could initiate condensation through dehydroxylation (scheme 6.1) or a more direct formation of oxo bridges. The presence of  $-\text{OH}$  in the films prior to irradiation likely contributes a background level of condensation that must be overcome with radiation exposure to induce

solubility changes and contrast in the films. Hence, the concentrations of hydroxide and peroxide in the films should play a significant role in determining the amount of background condensation.

Because no direct and quantitative method for the determination of peroxide concentration in an inorganic film has been previously reported, we have developed methods involving film stripping to produce solutions for analysis. Hf and peroxide solution concentrations were established through a combination of inductively-coupled-plasma optical-emission spectroscopy (ICP-OES), permanganate titrations, and Raman spectroscopy. The results were then used to examine relationships among peroxide concentration, electron beam exposure dose, and solubility contrast.

## **METHODOLOGY**

### **ICP-OES**

Hafnium concentrations were determined by using a Teledyne Leeman Prodigy ICP-OES in axial mode and monitoring spectral lines at 239.33 and 277.33 nm. A standard solution of 1-M  $\text{HfOCl}_2(\text{aq})$  was made from 99.99%  $\text{HfOCl}_2 \cdot 8\text{H}_2\text{O}$ , (Alfa Aesar) with 1% v/v nitric acid (ACS Grade, Malinckrodt). The Hf content of  $\text{HfOCl}_2 \cdot 8\text{H}_2\text{O}$  was determined from the mass of  $\text{HfO}_2$  produced by heating said chloride at 800 °C. Calibration curves were established with solutions diluted to 0.05, 0.5, 5, and 10 ppm with 1% v/v  $\text{HNO}_3(\text{aq})$ . An additional Hf standard (1000  $\mu\text{g}$  Hf/mL, Inorganic Ventures) was diluted in a similar manner. The 1% v/v  $\text{HNO}_3(\text{aq})$  alone was used to establish the baseline for the measurement. Films for analysis were deposited by spinning a 0.4-M  $\text{HfSO}_x$  solution[2,3,5] onto ten  $\text{O}_2$  plasma-treated 6" silicon wafers. Samples for analysis were

then stripped from the wafers with 1M H<sub>2</sub>SO<sub>4</sub>(aq). After stripping, the wafers were rinsed with 18.2 MΩ water, then gently blown with Ar(g) to collect the liquid remaining on the wafer. Five samples for ICP-OES analysis were made from 1mL aliquots that were diluted 1:50 with 1% HNO<sub>3</sub>(aq).

### **Titration**

Peroxide concentrations were determined by permanganate titration<sup>6</sup> of the samples used for ICP-OES measurements. 0.005-M KMnO<sub>4</sub> (EM Science 99%+), standardized with Na<sub>2</sub>C<sub>2</sub>O<sub>4</sub> (Acros Organics, 99%+), was used as the titrant. Permanganate was added in 10-μL aliquots and allowed to react slowly without heating until the endpoint was visually noted by a change in color from colorless to pale pink. Prior to titration of the film rinses, the measurement was tested by titration of peroxide solutions with known concentration. A measurement error of 1% and a detection limit of 1.25 x 10<sup>-7</sup> M peroxide were established.

### **Raman Measurements**

Raman spectra of HafSO<sub>x</sub> precursor solutions were collected by using a Nicolet FT-Raman instrument. Data collection and signal averaging were handled with Omnic 8 software. 1-mL samples of 0.5-M HfOCl<sub>2</sub>(aq) were prepared in 20-mL glass scintillation vials. Chilled hydrogen peroxide (Macron, 30% solution) was added in 10-μL aliquots to give ratios of H<sub>2</sub>O<sub>2</sub>:Hf up to 3:1. H<sub>2</sub>SO<sub>4</sub> (EMD, ACS Grade) was also added concurrently to give a H<sub>2</sub>SO<sub>4</sub>:Hf ratio of 0.7:1. Spectra were collected over the range 500-3000 cm<sup>-1</sup> with a total exposure time of 100 s. Measurement of an empty scintillation vial was used to establish background for the experiment.

Films were deposited onto 1 x 1" substrates of 200 nm thermally-deposited Al on SiO<sub>2</sub>. Prior to HafSO<sub>x</sub> deposition, substrates were treated in a Plasma Etch 50 O<sub>2</sub> plasma asher for five min. All films were deposited via spin-coating and then baked at 80 °C for three minutes. The resulting films were analyzed with a Horiba LabRAM Raman instrument equipped with a 100 x objective and 532-nm laser. Spectra were collected over the range 600–1300 cm<sup>-1</sup> by accumulating three spectra in 15 min. Raman spectra were also measured on films exposed to an electron beam at selected doses. Films were spun on aluminum substrates and then exposed via electron-beam writing to produce a 7 x 3 array of 200 x 200- μm squares with doses ranging from 0 to 800 μC/cm<sup>2</sup> in increasing increments of 40 μC/cm<sup>2</sup>. A 30-kV beam of an FEI Quanta 3D Dual Beam SEM/FIB was controlled with NPGS software for pattern writing. Following patterning, Raman spectra of the exposed and unexposed regions were obtained.

## **RESULTS AND DISCUSSION**

ICP-OES analysis for Hf concentration initially produced inconsistent results. Significant sample-to sample variation were observed, despite consistent handling and dilution methods. During measurement, the derived concentration of a given sample would decrease with sampling time. In each case, however, the concentration would stabilize at 0.5 mM. We surmised that residual Hf from the standard solution, which was run before each sample, appeared to be the source of the inconsistent results. An acid rinse with H<sub>2</sub>SO<sub>4</sub>(aq) was then used to clear the delivery lines prior to sample injection. With this procedure, measured concentrations more quickly stabilized at 0.5 mM. To confirm the results, a commercial standard was then used for comparison. The measurements were readily reproduced, again giving a Hf concentration of 0.5 mM with a standard deviation

of 2%. Concurrent with the ICP-OES analysis, the concentration of peroxide was determined by peroxide titrations. The equivalent peroxide concentration was found to be 0.27 M, affording a Hf:O<sub>2</sub><sup>2-</sup> ratio of 1.8:1 in the thin film.

Raman spectra for HafSO<sub>x</sub> solutions containing increasing concentrations of peroxide are shown in Figure 6.1. Bands, centered near 1000 cm<sup>-1</sup>, are attributed to sulfate. The central peak is assigned to sulfate bound to Hf, and the two remaining shoulders at 970 and 1050 cm<sup>-1</sup> are assigned to unbound sulfate.[7] Addition of peroxide to a solution containing only Hf and sulfate results in the appearance of a band near 830 cm<sup>-1</sup>, *cf.*, bottom two spectra in Figure 6.1. This signal is assigned to μ<sub>2</sub> binding of peroxide to Hf.[8] On further addition of peroxide, *cf.*, Figure 6.2, this signal grows. At a O<sub>2</sub><sup>2-</sup>:Hf ratio of 0.6:1, a new signal appears at 870 cm<sup>-1</sup>. This peak is also observed in solutions of 1% H<sub>2</sub>O<sub>2</sub>(aq), and it is assigned to the ν (O-O) stretch of solvated peroxide.[9] The unbound peroxide peak only appears beyond a O<sub>2</sub><sup>2-</sup>:Hf ratio of 0.6:1. Hence, this solution result is entirely consistent with the ratio deduced from ICP-OES analysis of thin films. Even with excess peroxide in the precursor solution, the Hf:O<sub>2</sub><sup>2-</sup> ratio saturates near 2:1 in the solution, and it persists in the film.

On the basis of these results and assuming a fully protonated state, the precursor formulation can be approximated as Hf(OH)<sub>1.6</sub>(O<sub>2</sub>)<sub>0.5</sub>(SO<sub>4</sub>)<sub>0.7</sub>·*q*H<sub>2</sub>O. During spin coating and the post-application bake a certain amount of –OH condensation occurs to form a continuous gel-like film. Additional condensation is then initiated through radiation exposure or additional, spontaneous water loss. The peroxide and sulfate Raman signals provide a convenient means for monitoring the effects of radiation exposure. As shown in Figure 6.2, strong bands at 830 and 1050 cm<sup>-1</sup>, corresponding to Hf-bound peroxide and

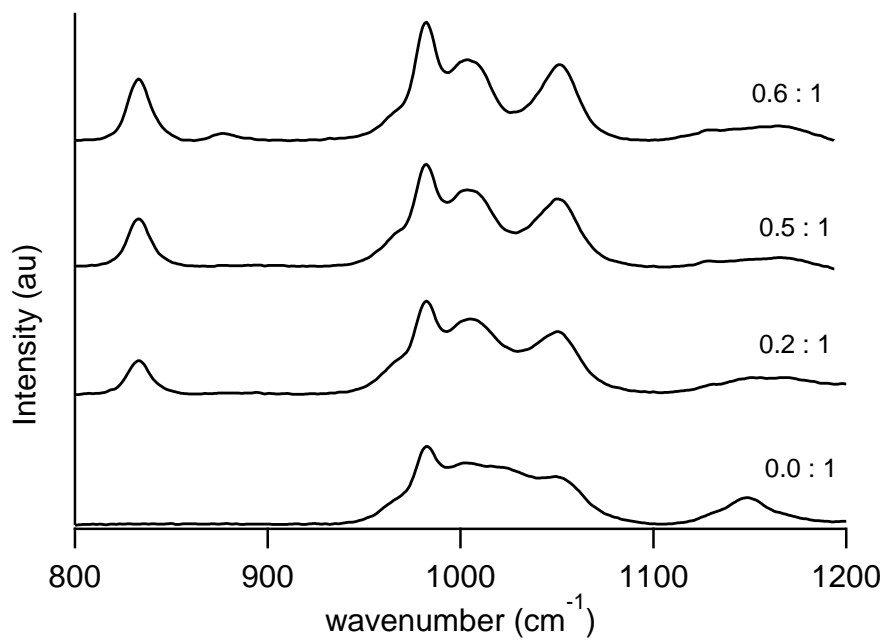


**Figure 6.1.** Raman spectra of HafSO<sub>x</sub> solutions with selected O<sub>2</sub><sup>2-</sup>:Hf ratios.

sulfate, respectively, are readily observed in unexposed films ( $0 \mu\text{C}/\text{cm}^2$ ). The films differ from the solutions in that free peroxide and sulfate are not observed. With increasing exposure (Figure 6.2) with a 30-kV electron beam, the peroxide signal diminishes relative to the sulfate signal, indicating peroxide is lost. This decreasing signal is correlated to studies of development contrast in Figure 6.3. Below a dose of approximately  $220 \mu\text{C}/\text{cm}^2$ , the development rate of an unexposed film is considerably faster than an exposed film in 25% TMAH(aq). Across the dose range  $220\text{--}340 \mu\text{C}/\text{cm}^2$ , the film switches from soluble to insoluble. In calibration studies, we have found a linear relationship between the peroxide Raman signal and concentration with a detection limit of 25% peroxide. Hence, a dose of  $340 \mu\text{C}/\text{cm}^2$  corresponds to photodecomposition of nearly 75% of total peroxide content. Through the transition region, no more than 15% of total peroxide is lost as a result of exposure.

## CONCLUSIONS

A combination of ICP-OES analysis, chemical titration, and Raman spectroscopy has been used to establish a working formula for a HafSO<sub>x</sub> photoresist. The resulting formulation  $\text{Hf}(\text{OH})_{1.6}(\text{O}_2)_{0.5}(\text{SO}_4)_{0.7} \cdot q\text{H}_2\text{O}$  represents the upper concentration limit of Hf-bound peroxide both in the solution precursor and the thin film. Under electron-beam exposure, nearly 75% of the bound peroxide must be eliminated to produce an insoluble product. These results represent an initial step toward unraveling the chemical processes that contribute to the production of high-resolution, high-fidelity nanostructures with HafSO<sub>x</sub>.

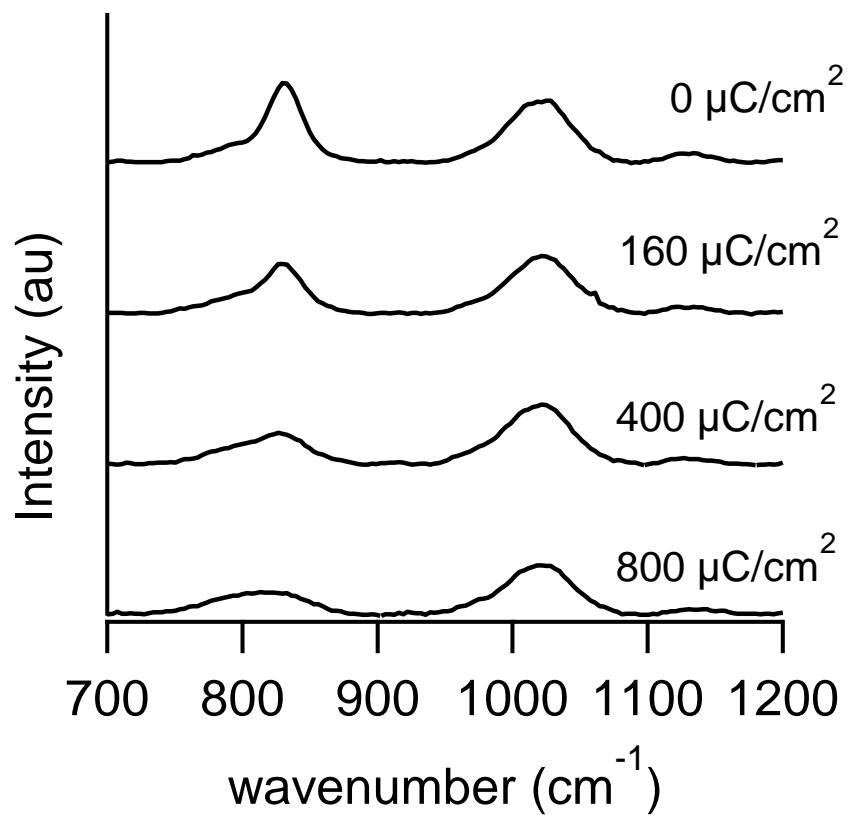


Figure 6.2. Raman spectra for HafSOx films after exposure with a 30-kV electron beam. The exposure dose associated with each spectrum is noted.

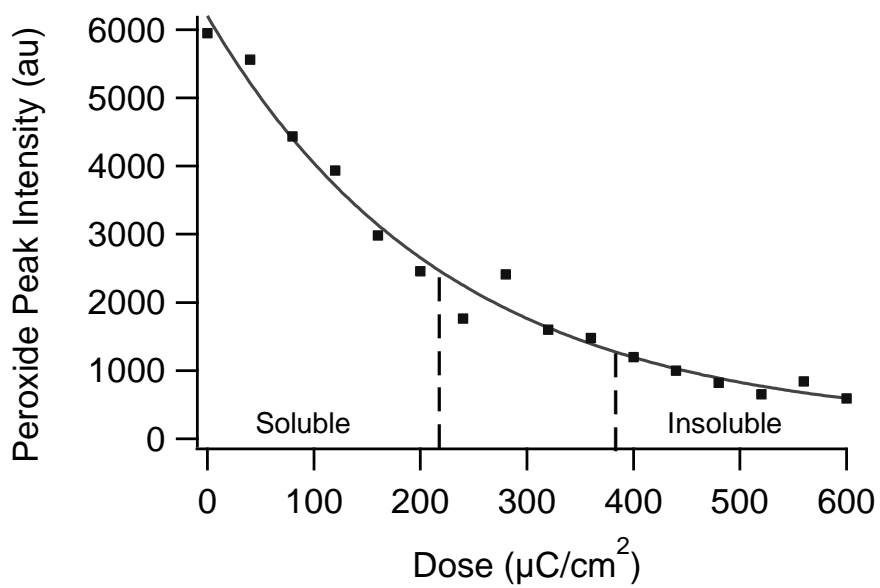


Figure 6.3: Raman signal as a function of electron-beam exposure dose and solubility characteristics.

## **ACKNOWLEDGMENTS**

This material is based upon work conducted in the Center for Sustainable Materials Chemistry, which is supported by the US National Science Foundation (grant number CHE-1102637). The authors thank Dr. Andy Ungerer for assistance with the ICP-OES measurements and Peter Eschbach and Teresa Sawyer for help with the electron-beam writing experiment.

## REFERENCES

- [1] Anderson, J.T.; Munsee, C.L.; Hung, C.M.; Phung, T.M.; Herman, G.S., Johnson, D.C.; Wager, J.F.; Keszler, D.A., Solution Processed HafSO<sub>x</sub> and ZircSO<sub>x</sub> Inorganic Thin-Film Dielectrics and Nanolaminates, *Adv. Funct. Mater.* **17**, 2117-2124 (2007).
- [2] Stowers, J.; Keszler, D. A. High Resolution, High Sensitivity Inorganic Resists *Microelectronic Eng.* **86** 730–733 (2009).
- [3] Telecky, A.; Xie, P.; Stowers, J.; Grenville, A.; Smith, B.; Keszler, D.A. Photopatternable Inorganic Hardmask. *J. Vac. Sci. Technol.* **26**, (2010).
- [4] Ekinici, Y.; Vockenhuber, M.; Terhalle, B.; Hojeij, M.; Wang, L.; Younkin, T. R. Evaluation of resist performance with EUV interference lithography for sub-22 nm patterning. *Proc. SPIE* **8322**, 83220W (2012).
- [5] Oleksak, R. P.; Ruther, R. E.; Luo, F.; Fairley, K.; Decker, S. R.; Stickle, W. F.; Johnson, D. W.; Garfunkel, E. L.; Herman, G. S.; Keszler, D. A. Chemical and structural investigation of high-resolution patterning with HafSO<sub>x</sub>. *ACS Appl. Mater. Interfaces*, DOI: 10.1021/am405463u (2014).
- [6] Huckaba, C. E.; Keyes, F. G. The Accuracy of Estimation of Hydrogen Peroxide by Potassium Permanagate Titration. *J. Am. Chem. Soc.* **70**, 1640-1644 (1948).
- [7] X-Ray and Vibrational Spectra of Sulfate in Earth Materials. *Reviews in Mineralogy and Geochemistry: Sulfate Minerals: Crystallography, Geochemistry, and Environmental Significance*, 1st ed.; The Mineralogical Society of America: Washington, DC, 2000: Vol. 40, pp 113-172.
- [8] Dickman, M. H.; Pope, M. T. Peroxo and Superoxo Complexes of Chromium, Molybdenum, and Tungsten. *Chem. Rev.* **94**, 579-584 (1994).
- [9] Moreno, T. Moran Lopez, M.A.; Huerta Illera, I.; Piqueras, C.M.; Sanz Arranz, A.; Garcia Serna, J.; Cocero, M.J. Quantitative Raman determination of hydrogen peroxide using the solvent as internal standard: Online application in the direct synthesis of hydrogen peroxide. *Chem. Eng. J.* **166**, 1061-1065 (2011).

## Chapter 7

Chemical and Structural Investigation of High-Resolution Patterning with HafSO<sub>x</sub>

Richard P. Oleksak, Rose E. Ruther, Feixiang Luo,§ Kurtis C. Fairley, **Shawn R. Decker**, William F. Stickle, Darren W. Johnson, Eric L. Garfunkel, Gregory S. Herman, and Douglas A. Keszler

Published in *ACS Applied Materials and Interfaces*, 6, 2917-2921 (2014)

**Abstract**

High-resolution transmission electron microscopy (TEM) imaging and energy-dispersive X-ray spectroscopy (EDS) chemical mapping have been used to examine key processing steps that enable sub-20-nm lithographic patterning of the material  $\text{Hf}(\text{OH})_{4-2x-2y}(\text{O}_2)_x(\text{SO}_4)_y \cdot q\text{H}_2\text{O}$  (HafSO<sub>x</sub>). Results reveal that blanket films are smooth and chemically homogeneous. Upon exposure with an electron beam, the films become insoluble in aqueous tetramethylammonium hydroxide [TMAH(aq)]. The mobility of sulfate in the exposed films, however, remains high, because it is readily exchanged with hydroxide from the TMAH(aq) solution. Annealing the films after soaking in TMAH(aq) results in the formation of a dense hafnium hydroxide oxide material that can be converted to crystalline  $\text{HfO}_2$  with a high electron beam dose. A series of 9 nm lines is written with variable spacing to investigate the cross-sectional shape of the patterned lines and the residual material found between them.

## Introduction

In this contribution, we describe results from high-resolution imaging and chemical analysis of thin films and patterned structures of  $\text{Hf}(\text{OH})_{4-2x-2y}(\text{O}_2)_x(\text{SO}_4)_y \cdot q\text{H}_2\text{O}$ , commonly known as HafSOx.[1] HafSOx is representative of a new approach involving the chemistry of nanosized inorganic clusters for addressing the resolution, line-width roughness (LWR), and sensitivity (RLS) trade-offs that limit lithographic performance of conventional organic materials at resolutions  $<20$  nm.[2–4] Dense, sub-10-nm features have already been written with HafSOx using extreme ultraviolet (EUV) irradiation.[5] By examining films and structures derived from electron-beam exposures, we offer new insights into the HafSOx patterning process.

The small spot size and direct-write capabilities of electron-beam lithography make it a convenient method for studying nanopatterning at high resolution.[6] Organic materials, such as polymethyl methacrylate (PMMA),[7–9] ZEP-520,[10,11] and related chemically amplified resists,[12] are commonly employed to produce features at resolutions near 30 nm. In such systems, resolution is limited by the large radius of gyration of a polymer chain (2–4 nm) and photoacid diffusion in chemically amplified systems. These characteristics lead to high LWR (2–4 nm), which ultimately limits resolution. Smaller LWRs ( $<2$  nm) have been demonstrated in inorganic materials, notably hydrogen silsequioxane (HSQ),[6,13] but this performance has come at the expense of poor sensitivities and long exposure times. The HafSOx system may offer a path for redefining the RLS triangle of conventional materials, because small LWRs and ultra-high-resolution features have been realized commensurate with relatively high sensitivities.[3] HafSOx uniquely affords these

characteristics, because other Hf-based systems exhibit low resolution[14] and low sensitivity.[15]

The patterning capabilities and radiation sensitivity of HafSO<sub>x</sub> derive from the presence of Hf-bound peroxy ligands. The absorption of radiation leads to dissociation of the O–O bond of the peroxy group, which drives condensation reactions and a reduced solubility in exposed areas.[2] Unexposed areas of a film may be readily dissolved in an appropriate developer, leaving a negative-tone pattern. The patterning process for HafSO<sub>x</sub> thus follows that of a conventional organic photoresist, involving some or all of the sequential steps: spin coat, post application bake, exposure, post-exposure bake, development, and hard bake. Films and structures derived from selected steps in this flow have been characterized to develop an improved understanding of the overall process. As film thickness and feature size approach 10 nm and smaller, it becomes increasingly difficult to characterize in detail films and patterns using conventional methods, such as scanning electron microscopy.[16] In this study, we have used cross-sectional transmission electron microscopy (TEM) and energy-dispersive X-ray spectroscopy (EDS) to better assess these nanodimensional features. In addition, the high atomic-number elements of the HafSO<sub>x</sub> system make these techniques especially useful for high-contrast imaging and chemical analysis. Because these characteristics are not commonly present in conventional patterning materials, e.g., organic resists, HafSO<sub>x</sub> presents a unique platform for studying lithographic patterning at near-atomic resolution.

## **Experimental**

Stock solutions (1 M) were prepared by dissolution and dilution of HfOCl<sub>2</sub>·8H<sub>2</sub>O (Alfa Aesar) and H<sub>2</sub>SO<sub>4</sub>(aq) (Mallinckrodt) with 18.2 MΩ purified water. Solutions for spin coating were

prepared by adding 30 wt %  $\text{H}_2\text{O}_2(\text{aq})$  (Macron) to the  $\text{HfOCl}_2(\text{aq})$  solution, followed by sequential addition of  $\text{H}_2\text{SO}_4(\text{aq})$  and 18.2 M $\Omega$  water. Final solutions were 0.15 M in hafnium, 0.105 M in sulfuric acid, and 0.45 M in hydrogen peroxide. Solutions were stable against precipitation for approximately 4 days at room temperature (depending upon the concentration) and several months when refrigerated. No change in film quality or reproducibility was observed for films deposited from aged, refrigerated solutions. Prior to spin coating, the substrates were treated with an  $\text{O}_2$  plasma to improve wetting of the substrate. Films were deposited by dispensing solutions through a 0.45  $\mu\text{m}$  filter and spin coating at 3000 rpm for 30 s. The films were then baked on a hot plate between 80 and 300  $^\circ\text{C}$  for 3–5 min. For patterning, films were baked at 80  $^\circ\text{C}$  for 3 min. Exposures were performed with a ZEISS Ultra-55 scanning electron microscope operating at 30 kV at a dose of 800  $\mu\text{C}/\text{cm}^2$ . The microscope was equipped with a JC Nabity writing system for pattern generation. Unexposed and exposed films were soaked or developed at room temperature in 25 wt % tetramethylammonium hydroxide (TMAH, Alfa Aesar) for 30–60 s, thoroughly rinsed with 18.2 M $\Omega$  water, and baked at 300  $^\circ\text{C}$  for 3–5 min. A J. A. Woollam M-2000 spectroscopic ellipsometer was used to measure film thickness. Data were collected in 5 $^\circ$  steps at incident angles covering the range of 55–65 $^\circ$ . A Cauchy model was used to extract thickness. A FEI Titan G2 80-200 transmission electron microscope with ChemiSTEM operating at 200 kV was used for imaging and chemical analysis. TEM samples were prepared as cross-sections via focused ion-beam lift-out using a FEI Quanta three-dimensional (3D) dual beam scanning electron microscope. Approximately 30 nm of amorphous carbon were thermally evaporated on the sample to serve as a protective layer during the lift-out process. EDS line scans were taken in STEM mode, and the areas were correlated to bright field TEM images that were acquired on nearby locations of the sample to avoid significant damage during STEM operation. The line scans were collected with a step size of 0.15–0.2 nm and then averaged over 1 nm to reduce noise. The scans were analyzed with Bruker Esprit 1.9 software using automatic background subtraction and quantification without

standards. X-ray photoelectron spectroscopy (XPS) measurements were performed with a Thermo Scientific KAlpha X-ray photoelectron spectrometer with an Al K $\alpha$  (1486.7 eV) micro-focus monochromatic X-ray source and ultra-low energy electron flood gun. A 50 eV pass energy was used for high-resolution, element-specific XPS spectra. Spectra were analyzed with an Avantage XPS software package. All peaks were charge-corrected to adventitious hydrocarbon at 284.8 eV, and Au metal was used for energy scale calibration of the photoelectron spectrometer.

## Results and Discussion

Cross-sectional TEM images and associated STEM-EDS traces of a blanket-coated, unexposed HafSO<sub>x</sub> film (baked at 300 °C) are shown in Figure 7.1. From the bottom to the top, the material stack consists of the Si substrate, native silicon oxide, spin-coated HafSO<sub>x</sub>, and carbon/platinum protective layers. A low-magnification image (Figure 7.1a) reveals that the HafSO<sub>x</sub> film is smooth and very uniform. This uniformity is confirmed with a high-magnification image (Figure 7.1b), which was obtained immediately upon moving to a new location on the sample. The HafSO<sub>x</sub> film thickness, measured to be 12–13 nm from spectroscopic ellipsometry measurements, agrees with the thickness and uniformity observed in these TEM images. Films are observed to change under prolonged exposure to the high-energy electron beam during analysis. A comparison of panels b and c of Figure 7.1, for example, reveals that the HafSO<sub>x</sub>/SiO<sub>x</sub> bilayer thickness increases from approximately 15 to 17 nm after a 5 min exposure. In this process, the HafSO<sub>x</sub> film thickness decreases from 12 to 9 nm, while the SiO<sub>x</sub> film thickness increases from 3 to 8 nm. This indicates that the electron beam is driving densification of the HafSO<sub>x</sub> layer while promoting further oxidation of the Si substrate. In the EDS line scan (Figure 7.1d), the S signal is found to track that of Hf, where S as a sulfate appears to be homogeneously

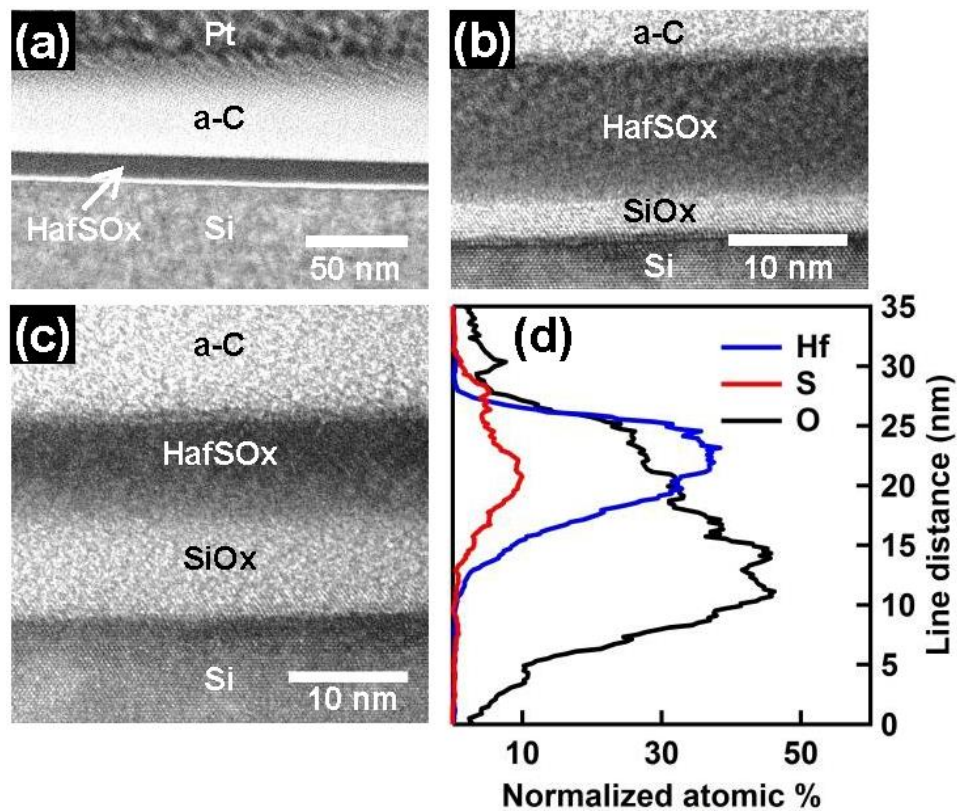


**Figure 7.1.** Cross-sectional TEM images of unexposed HafSO<sub>x</sub> film annealed at 300 °C (a-c) and STEM-EDS line scan (d) aligned to (c).

distributed with Hf throughout the thickness of the film. This distribution is consistent with imaging results, and it confirms the high uniformity of the films in terms of both morphology and composition.

TEM images and STEM–EDS chemical analysis data of a  $\text{HfSO}_x$  film, baked at 80 °C, exposed at 800  $\mu\text{C}/\text{cm}^2$ , soaked in 25% TMAH(aq), and baked at 300 °C, are shown in Figure 7.2. A low-resolution image (Figure 7.2a) indicates that the resulting film remains uniform and very smooth, similar to that of the unexposed film. From the high-resolution image (Figure 7.2c), the exposed film is found to be amorphous, and its thickness relative to an unexposed film (Figure 7.1b) decreases from approximately 12 to 7 nm. From the STEM–EDS line scan, sulfate (S) is no longer present in the film, following the soak in TMAH. These data indicate that electron-beam exposure and TMAH(aq) development have led to the formation of a thin, amorphous binary hafnium oxide hydroxide film. We also found that extended exposure of these films to the electron beam caused portions to crystallize (Figure 7.2b), producing atomic spacings consistent with monoclinic  $\text{HfO}_2$ .

XPS has been used to further elucidate composition and chemical state of the films. Hf 4f, S 2p, and O 1s spectra were monitored at four stages during the patterning process: (i) 80 °C post-application bake (PAB), (ii) 80 °C PAB and electron exposure dose of 800  $\mu\text{C}/\text{cm}^2$ , (iii) 300 °C PAB, and (iv) 80 °C PAB, exposure dose of 800  $\mu\text{C}/\text{cm}^2$ , soak in TMAH, and 300 °C post-soak bake. Results are summarized in Figure 7.3. Only subtle changes are observed in the relative intensities and binding energies of each element following only exposure and baking (80 °C, 80 °C and exposed, and 300 °C). After exposure and soaking in TMAH, however, significant spectral changes have occurred. For example, the O 1s and Hf 4f peaks shift to lower binding energies, and the S 2p peak is

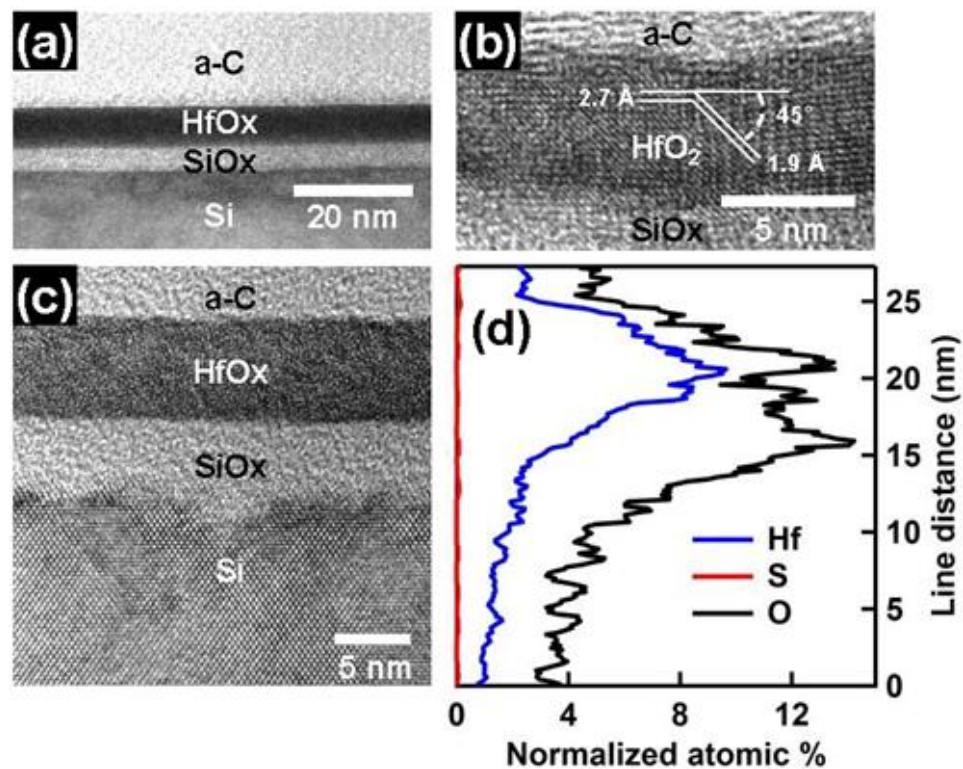


**Figure 7.2.** TEM cross sectional images of HafSOx film exposed at  $800 \mu\text{C}/\text{cm}^2$ , soaked in 25% TMAH, and hard baked at  $300 \text{ }^\circ\text{C}$  (a-c) and STEM-EDS line scan (d) aligned to (c).

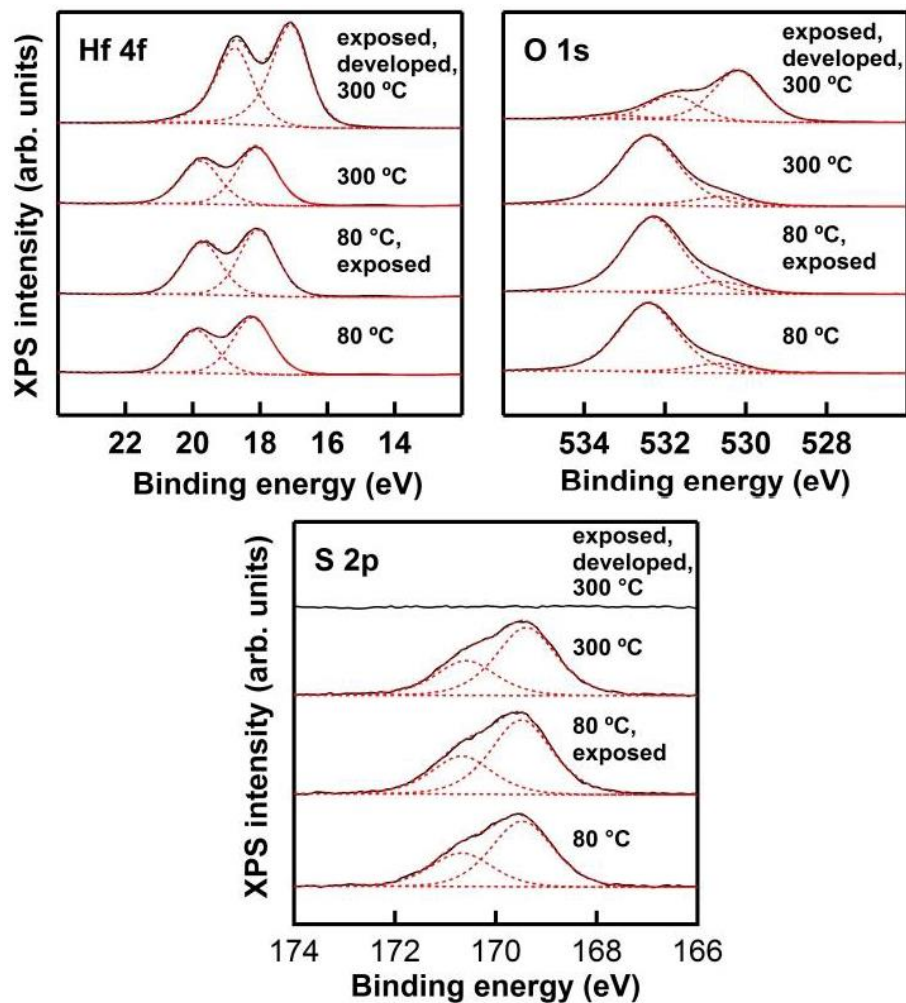


**Figure 7.3.** Hf 4f, O 1s, and S 2p X-ray photoelectron spectra of HafSOx films under selected process conditions.

now absent, indicating significant chemical changes, including the loss of sulfate from the film. For the O 1s spectra, the low-binding energy peak at 530.2 eV can be assigned to oxygen bound to Hf as oxide, while the high-binding-energy O 1s peak near 531.8 eV can be assigned to O bound as sulfate and hydroxo groups. Similar assignments have been made previously for Zr analogues of HafSO<sub>x</sub>. [17,18] For this sample, a third low-intensity peak at 533.3 eV was necessary to obtain an adequate fit; it is assigned to residual water that is present following the development process. This O 1s binding energy is consistent with water adsorbed to metal oxide surfaces. [19,20] We found that the low-binding energy metal oxide component becomes dominant after both exposure and TMAH soak. A similar change in the O 1s spectra was observed after the thermal desorption of sulfate from HafSO<sub>x</sub> films in ultrahigh vacuum. [21] While most of the oxygen is coordinated as Hf–O, a significant number of OH groups are detected following the 300 °C bake, which may be partly attributed to surface contamination from exposure to ambient prior to analysis. Together, the XPS and STEM–EDS analyses indicate that a fully exposed and developed HafSO<sub>x</sub> film is converted into a hafnium oxide hydroxide product.

We have extended these findings to examine fine-scale patterning of 9 nm wide lines using electron-beam lithography to write the lines at defined spacing by following the same processing steps as those used for the blanket films. A cross sectional TEM image, representing decreasing line spacing from 44 to 11 nm, is shown in Figure 7.4a. The average full width at half maximum (FWHM) line width is  $9.0 \pm 0.7$  nm. The features are readily resolved to the smallest spacing of 11 nm and a line–line distance of 21 nm. The rounded profiles reflect the modest development contrast of the system. [2] Initially, the as-processed features are amorphous, i.e., similar to the blanket film (Figure 7.2). After

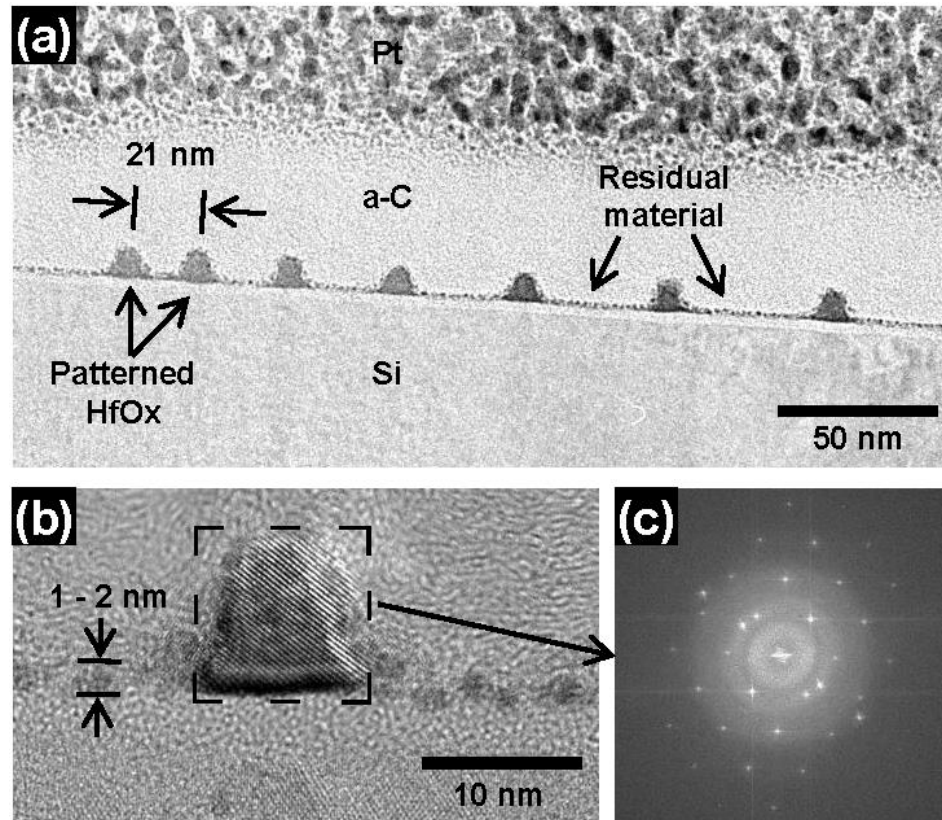


**Figure 7.4.** TEM cross sectional image of an electron-beam patterned HafSOx film after  $800 \mu\text{C}/\text{cm}^2$  exposure and development in 25% TMAH (a), HR-TEM image of single line (b) and fast Fourier transform (c) of region indicated in (b).

extended electron-beam exposure, the features are found to crystallize as monoclinic HfO<sub>2</sub> (Figure 7.4b). A Fourier transform (Figure 7.4c) of the atomic-resolved image indicates that the grain is oriented along the [101] zone axis. A very thin layer of residual material containing Hf is consistently observed between the lines, independent of spacing (Figure 7.4a). The TEM image of Figure 7.4b indicates that this residual is 1–2 nm thick and consists of small, discrete structures. HafSO<sub>x</sub> precursor solutions contain nanosized clusters (diameter  $\approx$  1 nm), and remnants of individual nanoclusters may become strongly bound to the substrate during the patterning process. At all of the line spacings, secondary electrons can also initiate exposure chemistry.

This exposure could enhance interactions between the deposited film and the substrate or simply render these regions insoluble during development. A small increase in residual material thickness is observed at the smallest line spacing, where the thinnest portion is 2 nm. The image contrast is darker and more uniform relative to that of the discrete structures between the more widely spaced lines (Figure 7.4b). The buildup and broadening of the profile tails between the patterned lines are likely due to proximity effects associated with scattered electrons.

Overall, the findings can be well-correlated to the chemistry expected for the HafSO<sub>x</sub> system, i.e.,  $\text{Hf}(\text{OH})_{1.6}(\text{O}_2)_{0.5}(\text{SO}_4)_{0.7} \cdot q\text{H}_2\text{O}$ . The binding of peroxide and sulfate to Hf in small nanosized clusters inhibits oligation and condensation reactions. As demonstrated, exposure to radiation drives peroxide decomposition,[22] inducing condensation reactions that lead to diminished solubility in TMAH(aq). However, this radiation induced condensation does not lead to full densification, because sulfate remains a mobile species. Because the films are solid acids, they are neutralized on contact with TMAH(aq), resulting

in extraction of sulfate. This sulfate is replaced with  $-OH$ , which sets the stage for additional condensation. The insolubility of the final product is thus initiated by both radiation and the follow-on development chemistry.

## **Conclusions**

In this study, we have demonstrated the utility of high-resolution imaging and composition-mapping techniques for examining selected chemical steps contributing to the direct patterning of an inorganic material at feature sizes near 10 nm. The techniques have been successfully used to identify key aspects of condensation, sulfate exchange, and residual formation that contribute to pattern fidelity within the  $HafSO_x$  system. We expect that the methods discussed herein will provide important information in future studies addressing near atomic-scale characterization of new classes of inorganic materials that hold promise for patterning at unprecedented resolutions.

## **Acknowledgments**

This material is based on work in the Center for Sustainable Materials Chemistry, which is supported by the U.S. National Science Foundation under Grant CHE-1102637. The authors thank Stephen Meyers, Jeremy Anderson, and Kai Jiang for several insightful discussions and Pete Eschbach for assistance with the electron microscopy work. Darren W. Johnson is a Scialog Fellow of Research Corporation for Science Advancement.

## **Author Information**

Corresponding Authors

E-mail: greg.herman@oregonstate.edu.

E-mail: douglas.keszler@oregonstate.edu.

Notes: The authors declare no competing financial interest.

## REFERENCES

- [1] Anderson, J. T.; Munsee, C. L.; Hung, C. M.; Phung, T. M.; Herman, G. S.; Johnson, D. C.; Wager, J. F.; Keszler, D. A. Solution processed HafSO<sub>x</sub> and ZircSO<sub>x</sub> inorganic thin-film dielectrics and nanolaminates. *Adv. Funct. Mater.* 2007, 17, 2117–2124.
- [2] Stowers, J.; Keszler, D. A. High resolution, high sensitivity inorganic resists. *Microelectron. Eng.* 2009, 86, 730–733.
- [3] Telecky, A.; Xie, P.; Stowers, J.; Grenville, A.; Smith, B.; Keszler, D. A. Photopatternable inorganic hardmask. *J. Vac. Sci. Technol., B: Nanotechnol. Microelectron.: Mater., Process., Meas., Phenom.* 2010, 28, C6S19–C6S22.
- [4] Thrun, X.; Choi, K. H.; Freitag, M.; Grenville, A.; Gutsch, M.; Hohle, C.; Stowers, J. K.; Bartha, J. W. Evaluation of direct patternable inorganic spin-on hard mask materials using electron beam lithography. *Microelectron. Eng.* 2012, 98, 226–229.
- [5] Ekinici, Y.; Vockenbuder, M.; Hojeij, M.; Wang, L.; Mojarad, N. M. Evaluation of EUV resist performance with interference lithography towards 11 nm half-pitch and beyond. *Proc. SPIE* 2013, 8679, 867910–867910.
- [6] Grigorescu, A. E.; Hagen, C. W. Resists for sub-20-nm electron beam lithography with a focus on HSQ: State of the art. *Nanotechnology* 2009, 20, 292001.
- [7] Haller, I.; Hatzakis, M.; Srinivasan, R. High-resolution positive resists for electron-beam exposure. *IBM J. Res. Dev.* 1968, 12, 251–256.
- [8] Chen, W.; Ahmed, H. Fabrication of 5–7 nm wide etched lines in silicon using 100 keV electron beam lithography and polymethylmethacrylate resist. *Appl. Phys. Lett.* 1993, 62, 1499–1501.
- [9] View, C.; Carcenac, F.; Pepin, A.; Chen, Y.; Mejias, M.; Lebib, A.; Manin-Ferlazzo, L.; Couraud, L.; Launois, H. Electron beam lithography: Resolution limits and applications. *Appl. Surf. Sci.* 2000, 164, 111–117.
- [10] Nishida, T.; Notomi, M.; Iga, R.; Tamamura, T. Quantum wire fabrication by e-beam lithography using high-resolution and high-sensitivity e-beam resist ZEP-520. *Jpn. J. Appl. Phys., Part 1* 1992, 31, 4508–4514.
- [11] Tanenbaum, D. M.; Lo, C. W.; Isaacson, M.; Craighead, H. G.; Rooks, M. J.; Lee, K. Y.; Huang, W. S.; Chang, T. H. P. High resolution electron beam lithography using ZEP520 and KRS resists at low voltage. *J. Vac. Sci. Technol., B: Microelectron. Nanometer Struct. Process. Meas., Phenom.* 1996, 14, 3829–3833.
- [12] Ito, H. Chemical amplification resists for microlithography. *Adv. Polym. Sci.* 2005, 172, 37–245.
- [13] Namatsu, H.; Takahashi, Y.; Yamazaki, K.; Yamaguchi, T.; Nagase, M.; Kurihara, K. Three-dimensional siloxane resist for the formation of nanopatterns with minimum linewidth fluctuations. *J. Vac. Sci. Technol., B: Microelectron. Nanometer Struct. Process., Meas., Phenom.* 1998, 16, 69–76.
- [14] Trikeriotis, M.; Bae, W. J.; Schwartz, E.; Krysak, M.; Lafferty, N.; Xie, P.; Smith, B.; Zimmerman, P. A.; Ober, C. K.; Giannelis, E. P. Development of an inorganic photoresist for DUV, EUV, and electron beam imaging. *Proc. SPIE* 2010, 7639, 76390E–76390E.
- [15] Saifullah, M. S. M.; Khan, M. Z. R.; Hasko, D. G.; Leong, E. S. P.; Neo, X. L.; Goh, E. T. L.; Anderson, D.; Jones, G. A. C.; Welland, M. E. Spin-coatable HfO<sub>2</sub>

- resist for optical and electron beam lithographies. *J. Vac. Sci. Technol., B: Microelectron. Nanometer Struct. Process., Meas., Phenom.* 2010, 28, 90–95.
- [16] Broers, A. N.; Hoole, A. C. F.; Ryan, J. M. Electron beam lithography Resolution limits. *Microelectron. Eng.* 1996, 32, 131–142.
- [17] Hino, M.; Kurashige, M.; Matsushashi, H.; Arata, K. The surface structure of sulfated zirconia: Studies of XPS and thermal analysis. *Thermochim. Acta* 2006, 441, 35–41.
- [18] Breilkopf, C.; Papp, H.; Li, X.; Olindo, R.; Lercher, J. A.; Lloyd, R.; Wrabetz, S.; Jentoft, F. C.; Meinel, K.; Förster, S.; Schindler, K.-M.; Neddermeyer, H.; Widdra, W.; Hofmann, A.; Sauer, J. Activation and isomerization of n-butane on sulfated zirconia model systems – An integrated study across the materials and pressure gaps. *Phys. Chem. Chem. Phys.* 2007, 9, 3600–3618.
- [19] Henderson, M. A. The interaction of water with solid surfaces: Fundamental aspects revisited. *Surf. Sci. Rep.* 2002, 46, 1–308.
- [20] Herman, G. S.; Kim, Y. J.; Chambers, S. A.; Peden, C. H. F. Interaction of D<sub>2</sub>O with CeO<sub>2</sub>(001) investigated by temperature programmed desorption and X-ray photoelectron spectroscopy. *Langmuir* 2009, 15, 3993–3997.
- [21] Flynn, B.; Kim, D.; Clark, B. L.; Telecky, A.; Arnadottir, L.; Szanyi, J.; Keszler, D. A.; Herman, G. S. In-situ characterization of aqueous-based hafnium oxide hydroxide sulfate thin films. *Surf. Interface Anal.* 2013, DOI: 10.1002/sia.5205.
- [22] Okamoto, H.; Ishikawa, A.; Kudo, T. Photoresist characteristics and their reaction mechanism for crystalline peroxopolytungstic acid. *J. Electrochem. Soc.* 1989, 136,

## Chapter 8

Nanoscale Patterning Mechanisms of Hafnium Polyoxometalate Thin Films

Rose E. Ruther, Feixiang Luo , Richard P. Oleksak, Jennie M. Amador, **Shawn R. Decker**, Milton N. Jackson, Joshua R. Motley, Darren W. Johnson, Gregory S. Herman, Eric L. Garfunkel, and Douglas A. Keszler

To be submitted for publication

**Abstract**

Polyoxometalates and related metal oxide thin films formed by the condensation of nanoscale clusters are promising inorganic resist materials for ultrahigh resolution lithography. Under acidic conditions, hafnium ions, in an appropriate solution, form very small clusters (radius  $< 1$  nm). By controlling the assembly of clusters into thin films which contain radiation sensitive species, very high resolution patterns can be written with UV photons or electrons. Here we elaborate on the mechanisms which control the thermal and radiation chemistry of these materials and ultimately the sensitivity and resolution which can be obtained. Raman and X-ray photoelectron spectroscopies are used to follow the coordination of sulfate and peroxide ligands in films as a function of thermal processing and radiation exposure. Results from the spectroscopic studies are correlated with direct measurements of film solubility and resist sensitivity. Small changes in the solution chemistry of the film precursors yield significant differences in the patterning properties of the final films. The ability to control condensation chemistry and radiation sensitivity is critical to further developing cluster based materials which can be directly patterned at the nanoscale.

## Introduction

The ability to pattern materials at ever smaller length scales has driven advances in electronics, photonics, plasmonics, micro/nano-electromechanical systems, and sensor technologies. To continue to decrease the feature size that can be achieved with photon and electron beam based lithographic patterning, improvements in resists are necessary. Chemically amplified resists have become the standard since they were first introduced by IBM in the 1980s. While these resists have excellent sensitivity, acid diffusion, statistical dose fluctuations and other factors contribute to line edge roughness (LER) and limit resolution.[1] Very high resolution has been achieved with non-chemically amplified resists such as a poly(methyl methacrylate) (PMMA)[2, 3] and hydrogen silsesquioxane (HSQ)[4, 5] but conversely these materials require large exposure doses. As pattern dimensions continue to shrink, the molecular and nanoscale structure of the resist itself becomes increasingly important. Large LER in polymeric resists has been attributed to the formation of polymer aggregates with sizes on the order of tens of nanometers.[6-8] Low LER in resists of calixarene[9], molecular glasses[10], HSQ[11], and nanoparticles[12] have been attributed to the small size and uniformity of the fundamental nanoscale units which make up these materials. We are not aware of definitive proof of the LER to cluster size correlation, although the rationale has appeared often in the literature.

Films formed by the deposition of aqueous polyoxometalate clusters offer a very promising approach to nanoscale patterning. If clusters size is in fact critical, then highly monodisperse clusters can be synthesized and used to produce films with cluster/grain size well below what is typically achieved with other methods. Many metal oxides have

relatively high absorbance for EUV (13.5 nm) lithography.[13] Additionally, inorganic materials offer very high etch resistance which enables thinner resists and prevents pattern collapse of high aspect ratio features.[12] Thinner films also reduce proximity effects and enable higher resolution.[4] Recently, we showed that metal oxide sulfates ( $\text{MSO}_x$ ) demonstrate very high resolution, moderately high sensitivity, and exceptionally low LER.[14-16] We believe that the resist chemistry that leads to pattern formation is based on the controlled condensation (by photon or electron radiation) of metal oxide clusters which are deposited from aqueous solutions using spin-coating.

In this contribution, we elaborate on the thermal and radiation chemistry of the hafnium based system ( $\text{HfSO}_x$ ). Under acidic conditions in the absence of strongly complexing anions, hafnium is believed to form tetranuclear clusters, while in solution, with the formula  $[\text{Hf}_4(\text{OH})_8(\text{H}_2\text{O})_{16}]^{8+}$  as shown in Figure 8.1a.[17, 18] Both sulfate and peroxide are known to coordinate strongly to hafnium (IV),[19] and may change the predominant cluster species in solution. Very smooth, amorphous films can be deposited from hafnium sulfate solutions,[20] while the addition of radiation-sensitive peroxide ligands yields a smooth film that can be directly patterned using UV light or electron beams.[14-16] By monitoring the chemical changes that occur in the film as a function of annealing temperature and radiation exposure, a more mechanistic understanding of the roles these coordinating ligands play in determining film properties emerges. The sensitivity and resolution of the resist is strongly dependent on the composition of the film precursors. The results presented here are an important step towards understanding and controlling condensation chemistry in resists formed from metal oxide clusters and will help to advance the development of future classes of inorganic resists.

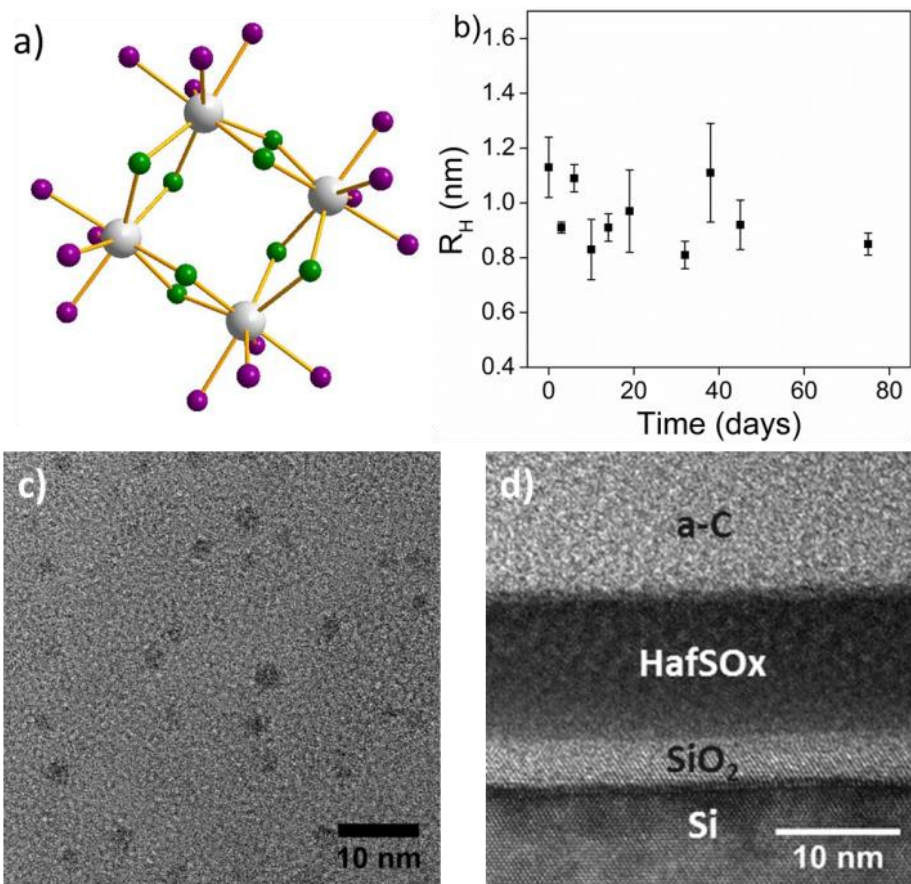


**Figure 8.1.** (a) Structure of hafnium tetramer. White: hafnium; Green: hydroxyl oxygen; Purple: oxygen in bound water. (b) DLS size analysis for a 150 mM HafSO<sub>x</sub> solution as a function of solution age. (c) TEM image of hafnium sulfate clusters. (d) Cross-sectional TEM image of a spin-coated HafSO<sub>x</sub> film on a Si/SiO<sub>x</sub> substrate with an amorphous carbon protecting layer.

## Experimental

### Solution Precursor Preparation.

A hafnium stock solution was prepared from  $\text{HfOCl}_2 \cdot 8\text{H}_2\text{O}$  (98+%, Alfa Aesar) and 18.2 M $\Omega$  purified water at approximately 1 M concentration. The exact concentration was determined gravimetrically by conversion of a known volume of solution to solid hafnium oxide. 1 M  $\text{H}_2\text{SO}_4$  (BDH Chemicals) and 30 wt%  $\text{H}_2\text{O}_2$  (Macron) were used as received. All  $\text{HfSO}_x$  solutions were prepared by mixing  $\text{HfOCl}_2$ ,  $\text{H}_2\text{O}_2$ , and  $\text{H}_2\text{SO}_4$  solutions and diluting with 18.2 M $\Omega$  purified water to the appropriate concentration. A standard  $\text{HfOCl}_2$ : $\text{H}_2\text{O}_2$ : $\text{H}_2\text{SO}_4$  ratio of 1:3:0.7 was used in all  $\text{HfSO}_x$  films unless otherwise noted. For other films with different ratios, the sulfate to hafnium molar ratio varied from 0.1 to 2. The peroxide to hafnium molar ratio varied from 0 to 7. The molarity of the precursor solution is given with respect to hafnium.

### Film Deposition

For experiments using a quartz crystal microbalance (QCM), thin  $\text{HfSO}_x$  films were deposited onto QCM crystals with  $\text{SiO}_x$  coatings designed for liquid applications (Inficon). Prior to deposition, the QCM crystals were cleaned with a UV/ozone treatment to generate a hydrophilic surface. For Raman spectroscopy, films were deposited on sapphire or aluminum substrates (80 nm Al/200 nm thermal  $\text{SiO}_2/\text{Si}$ ). For all other experiments films were deposited on Si<100> substrates with native oxide. Prior to deposition the silicon substrates were rinsed with deionized water, acetone, and isopropanol, and then treated with oxygen plasma for 5 – 10 minutes. All films were deposited via spin coating at 3000 rpm for 30 s, followed by a thermal anneal on a hotplate at temperatures from 70 – 300 °C.

### **Dynamic Light Scattering (DLS)**

DLS measurements were taken using the Mobius instrument from Wyatt technologies. The samples were filtered using a 0.1  $\mu\text{m}$  PTFE syringe tip to remove any particulate matter. The hydrodynamic radius ( $R_h$ ), and polydispersity were determined using Dynamics software where the data was averaged over 20 measurements with 5 second integration time per acquisition.

### **Microscopy**

Transmission electron microscopy (TEM) imaging was performed using an FEI Titan 80-200 TEM operating at 200 kV. For cluster images, a surface functionalized TEM grid (NanoPlus, Dune Sciences) was placed face down on a drop of a 150 mM  $\text{HafSO}_x$  solution. The grid was then placed face down on deionized water to rinse off excess material. TEM cross sections were prepared via the focused ion beam lift out method on a Quanta 3D Dual Beam scanning electron microscope. Atomic Force Microscopy (AFM) images were acquired with a Bruker Innova AFM in intermittent contact (tapping) mode using silicon probes with a resonance frequency of 300 kHz and a force constant of 40 N/m (Budget Sensors). To correct for sample tilt and scanner bow, images were leveled by polynomial background subtraction. Scanning electron microscopy (SEM) imaging was performed on an FEI Nova NanoSEM 230 operating at 5 kV.

### **Raman Spectroscopy**

Solution Raman spectra ( $500\text{-}3000\text{cm}^{-1}$ ) were collected on a Thermo Scientific DXR SmartRaman spectrometer with a 780 nm laser source. Thin film Raman spectra were collected using a Horiba LabRAM 800 equipped with a 532 nm laser source, 300 lines/mm

grating, and a 100x objective. The Raman frequency shift was calibrated using a SiO<sub>2</sub> standard.

### **Quartz Crystal Microbalance**

QCM measurements of film etch rate were measured with an RQCM (research quartz crystal microbalance) and PLO-10i (phase lock oscillator) system from Inficon. QCM crystals were placed in a crystal holder designed for contact with liquids. Crystals were immersed in tetramethylammonium hydroxide solutions (electronic grade, Alfa Aesar) and the change in resonance frequency was monitored with a frequency counter (Keithley) and recorded using custom software.

### **X-ray Photoelectron Spectroscopy (XPS)**

XPS spectra were acquired with a Thermo Scientific K-alpha X-ray photoelectron spectrometer with an Al K $\alpha$  (1486.6 eV) micro-focused monochromatic X-ray source and ultra-low energy electron flood gun. A pass energy of 50 eV was used for high-resolution element-specific XPS spectra. All spectra were analyzed with the Avantage software package from Thermo Scientific. The binding-energy scale was calibrated with the adventitious carbon 1s peak at 284.8 eV. The number of O peaks was set to two, and peak full width half maxima (FWHM) were constrained to be in the range of 1.7-1.8eV for peak fitting of the oxygen 1s spectra. The peak fitting was conducted with mixed Lorentzian and Gaussian peak shapes, while for background we used the “Smart” Shirley method.

### **Peroxide analysis**

The peroxide content of the thin films was measured using standard permanganate titrations and compared to the hafnium content measured by inductively coupled plasma optical emission spectrometry (ICP-OES). Samples were prepared by stripping films from

silicon wafers with 1 M sulfuric acid. A portion of the sample was titrated with  $\text{KMnO}_4$  for peroxide analysis and the remainder was diluted with 1% nitric acid for ICP analysis. The hafnium concentration was determined using a Teledyne Leeman Prodigy ICP-OES in axial mode using spectral lines of 277.33 and 239.33 nm. Standards were made by diluting a 1000 ppm hafnium standard (Inorganic Ventures) with 1% nitric acid.

## Results and Discussion

First, we establish that the film precursor solutions consist of discrete nano-sized clusters. Figure 8.1b shows DLS data for a 150 mM  $\text{HafSO}_x$  solution. The sample was kept refrigerated at 5 °C and aliquots were taken periodically for size analysis. The clusters have a hydrodynamic radius of approximately 1 nm and no change in size is observed over the course of several months. The size was also measured directly with TEM. Clusters with a radius of 1-2 nm were imaged and are shown in Figure 8.1c. The size measured by TEM is larger than that measured by DLS, possibly due to small amounts of aggregation that occur when the samples are dried on the TEM grid. The size from DLS is also larger than would be expected for the hafnium tetramer.[21] Since DLS measures the hydrodynamic radius of a species, the larger DLS radius could also result from solvent and/or counterion association with the clusters.[22] The addition of sulfate and peroxide ligands results in more highly polymerized species consistent with prior work on zirconium sulfate solutions.[23, 24] Figure 8.1d shows a cross-sectional TEM image of a  $\text{HafSO}_x$  film deposited via spin coating on  $\text{Si/SiO}_x$  substrates. This image illustrates the very low roughness of the film, which can be attributed to the small size of the clusters in the precursor solution. Surface roughness also correlates with sidewall roughness in fully

developed patterns.[7, 8, 11] The exceptional smoothness of HafSO<sub>x</sub> films correlates well with the very low LER observed in our patterned films.[14, 15]

The coordination of sulfate and peroxide ligands to the clusters was studied using Raman spectroscopy. Figure 8.2a shows the Raman spectra of the precursor solution, as well as sulfuric acid and hydrogen peroxide for comparison. The  $\nu(\text{O-O})$  vibration in free (uncoordinated) peroxide appears at  $876\text{ cm}^{-1}$  as seen in the spectrum of aqueous hydrogen peroxide. The coordination of peroxide to the hafnium clusters results in a new stretch at  $834\text{ cm}^{-1}$  consistent with what has been observed previously for peroxo complexes of hafnium and zirconium.[25-27] Typically a large excess of peroxide, usually 3 molar equivalents of peroxide relative to  $\text{HfOCl}_2$ , is added to the precursor solution to stabilize the small hafnium clusters and prevent the formation of an insoluble network. Peroxide acts as a capping ligand which prevents oligation and condensation similar to acetylacetonate or carboxylate ligands commonly used in sol gel chemistry.[28] While a significant amount of free peroxide is typically present in the solutions, only bound peroxide is present in the final (pre-radiation exposure) films (Figure 8.2a). Similar to monitoring the peroxide, the coordination of sulfate to the hafnium clusters can be followed in the Raman spectra. Free sulfate and bisulfate appear at  $982$  and  $1050\text{ cm}^{-1}$  respectively[29] as seen in the spectrum of aqueous sulfuric acid (Figure 8.2a). At least two new vibrational modes appear for sulfate coordinated to hafnium, with peaks at  $967$  and  $1004\text{ cm}^{-1}$ . Similar spectra have been reported for other sulfate complexes.[30, 31] Both free and bound sulfate are present in the precursor solution, but films contain primarily bound sulfate.

As a radiation sensitive ligand, peroxide plays an important role in the patterning chemistry (*vide infra*). The number of peroxide ligands that can bind to each cluster is

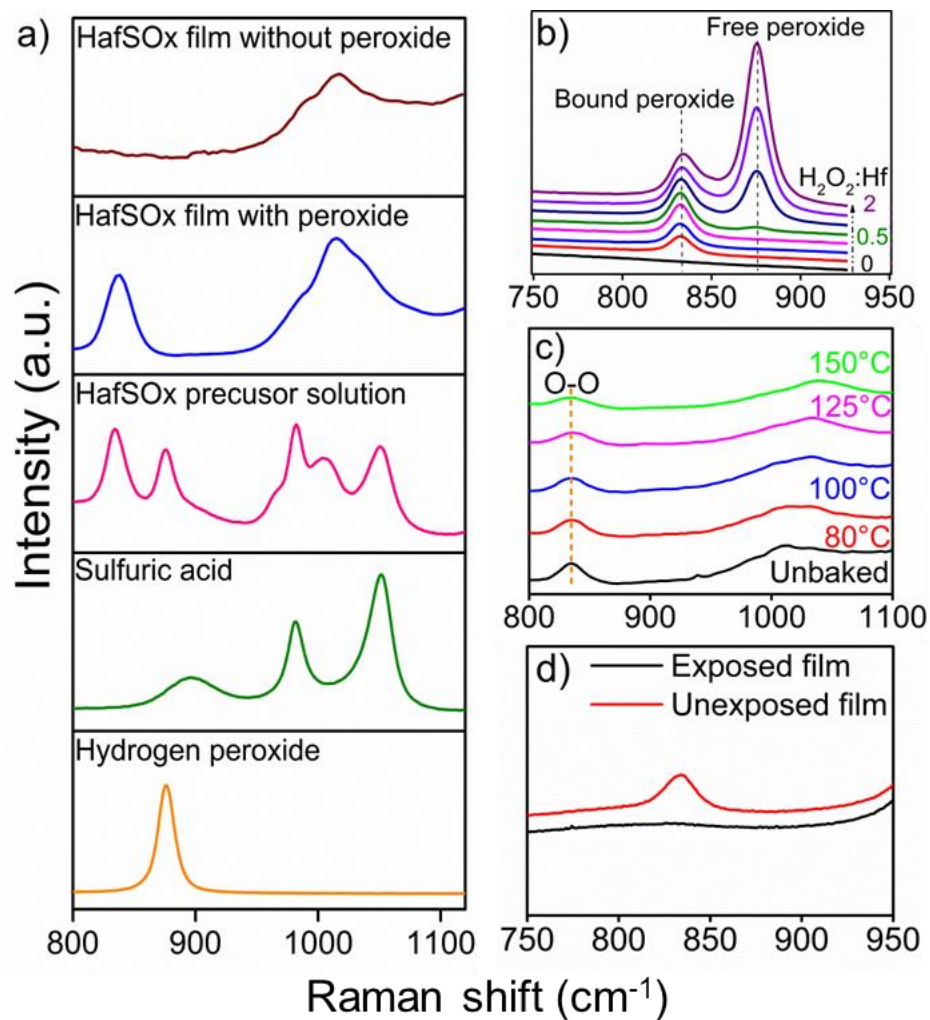


**Figure 8.2.** Raman spectra of (a) hydrogen peroxide, sulfuric acid, the HafSOx precursor solution, and HafSOx films made with and without peroxide. (b) HfOCl<sub>2</sub> solutions with increasing concentrations of hydrogen peroxide. (c) HafSOx films annealed at increasingly high temperatures. (d) A HafSOx film before and after exposure to electron beam radiation.

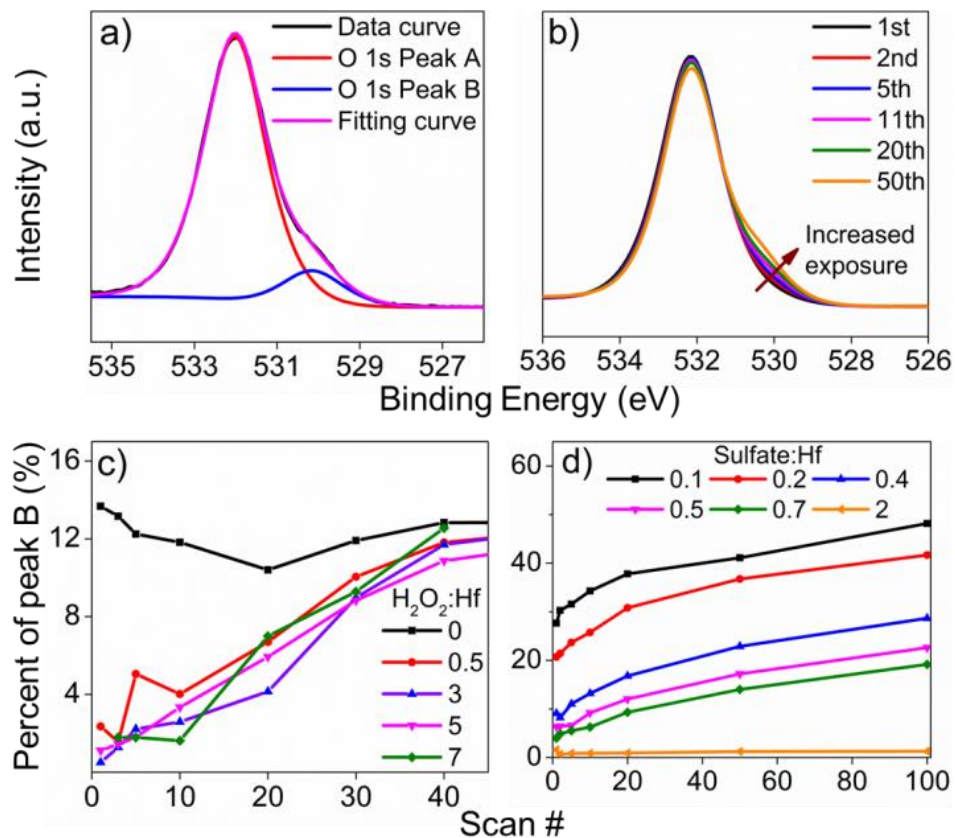
likely an important factor that influences the sensitivity of the final resist. We therefore sought to characterize the relative amount of bound peroxide in the precursor solutions and resulting films. Figure 8.2b shows Raman spectra of  $\text{HfOCl}_2$  solutions with increasing amounts of hydrogen peroxide. For low peroxide concentrations, all of the peroxide coordinates to the cluster and only the stretch at  $834\text{ cm}^{-1}$  is observed. With increasing amounts of peroxide, the free peroxide stretch at  $876\text{ cm}^{-1}$  appears and grows in intensity, while the intensity of the bound peroxide stretch saturates. The free peroxide stretch first appears when the peroxide to hafnium molar ratio reaches 0.5, indicating that approximately 2 peroxide ligands can coordinate to each hafnium tetrameric unit. This is consistent with prior investigations which propose that two peroxide groups replace four hydroxyl groups in the tetramer to form  $[\text{Hf}_4(\text{O}_2)_2(\text{OH})_4(\text{H}_2\text{O})_{16}]^{8+}$ . [32] The peroxide to hafnium ratio was also measured in films. As deposited, the films are soluble and can be rinsed from the substrates for analysis using standard wet chemical techniques, such as wet etching with tetramethylammonium hydroxide (TMAH). The peroxide to hafnium molar ratio was determined to be  $0.67 \pm 0.09$  from permanganate titration and ICP-OES analysis. Both the solution and thin film analysis indicate that the number of peroxide ligands that are able to bind to each hafnium cluster is relatively small, with less than one peroxide group per hafnium ion.

Figure 8.2c shows Raman spectra of thin films annealed at the indicated temperatures for three minutes. The peroxide group was found to be thermally stable in the films and shows only a 20% loss in intensity in the Raman spectrum when annealed to  $125\text{ }^\circ\text{C}$ . Figure 8.2d shows Raman spectra for a film soft-baked at  $80\text{ }^\circ\text{C}$  before and after exposure to a  $5\text{ kV}$  electron beam with a dose of  $800\text{ }\mu\text{C}/\text{cm}^2$ . The Raman peak associated

to peroxide bound to Hf is completely eliminated under this electron beam exposure. Thus the peroxide group exhibits relatively high thermal stability, but is readily eliminated by e-beam radiation. This selectivity is an important factor why peroxide groups are central in enabling inorganic resists to function.

The reactions in the HafSO<sub>x</sub> films were further explored using XPS. Figure 8.3a shows a typical O 1s spectrum obtained after a relatively long x-ray exposure (> 30 min.). The O 1s peak can be resolved into two components. The higher binding energy (BE) O 1s peak at 532.0 eV (peak A) is assigned to oxygen in hydroxyl and sulfate groups.[33-37] The lower BE O 1s peak at 530.2 eV (peak B) can be attributed to oxygen in the Hf-O-Hf network, similar to hafnium oxides.[35-38] Figure 8.3b shows the evolution of the O 1s spectrum with increasing number of scans and exposure to X-rays. The increase in the intensity of the lower BE peak is consistent with the growth of the oxide network with continued exposure to radiation. Figure 8.3c plots the atomic percent of peak B out of the total oxygen (peak A + peak B), which provides a quantitative method to monitor the dynamic formation of the Hf-O-Hf network. In the unexposed films, peroxide groups prevent condensation and very little of peak B can be resolved. Radiation-induced decomposition of peroxide groups leads to oxide network formation which saturates around 30 scans, corresponding to a flux of order  $10^{15}$  -  $10^{16}$  photons/cm<sup>2</sup>.

Film condensation was also monitored using XPS for films spun from solutions with different amounts of peroxide (Figure 8.3c). HafSO<sub>x</sub> films made without H<sub>2</sub>O<sub>2</sub> initially show significant oxide network formation, and no increase is observed with increasing X-ray exposure. Films made with at least a 0.5 peroxide to hafnium ratio in solution show very similar behavior with respect to condensation. This is consistent with



**Figure 8.3.** (a) XPS O1s spectra of a HafSO<sub>x</sub> film collected after a long X-ray exposure time (>30 min.). (b) XPS O1s peak evolution with increasing number of scans. (c) Quantitative comparison of O 1s peak evolution for HafSO<sub>x</sub> films with increasing amounts of peroxide. (d) Quantitative comparison of O 1s peak evolution for HafSO<sub>x</sub> films with increasing amounts of sulfate.

results from Raman spectroscopy and wet chemical analysis which indicate that the amount of peroxide in the films saturates at less than one peroxide group per hafnium ion.

Increasing the amount of peroxide in the solutions above a molar ratio of 0.5 does not cause further changes in the radiation chemistry of the films. The XPS results provide further evidence to the argument that oxide network formation is driven by the decomposition of peroxide groups.

Film condensation can also be controlled by the concentration of sulfate groups. Figure 8.3d plots the atomic percent of peak B out of the total oxygen for films made with different sulfate concentrations. Films with a lower sulfate concentration show a higher percentage of oxygen coordinated as oxide at the beginning of X-ray exposure. All films with the sulfate to hafnium ratio  $< 2$  show increasing oxide formation with longer X-ray exposure. The curves also follow the same slope, which confirms that similar amounts of peroxide are present in the films to drive further condensation. When the hafnium to sulfate ratio is equal to 2, no measurable oxide is present. Since the stoichiometry of the film is close to  $\text{Hf}(\text{SO}_4)_2$ , no additional oxide or hydroxide ligands are needed for charge balance.

The condensation reactions that occur upon exposure to radiation result in a decrease in solubility of the exposed regions. To further understand how changes in processing conditions influence film solubility, film dissolution was monitored using QCM. Films were deposited on QCM crystals, and the change in mass was monitored as the films were dissolved in TMAH solutions.[39, 40] Figure 8.4a shows results for the dissolution of films made with and without peroxide. The films made with peroxide are significantly more soluble as seen by the much larger loss in mass. These results provide further evidence that peroxide acts as a capping ligand, preventing oxidation and network formation. Annealing

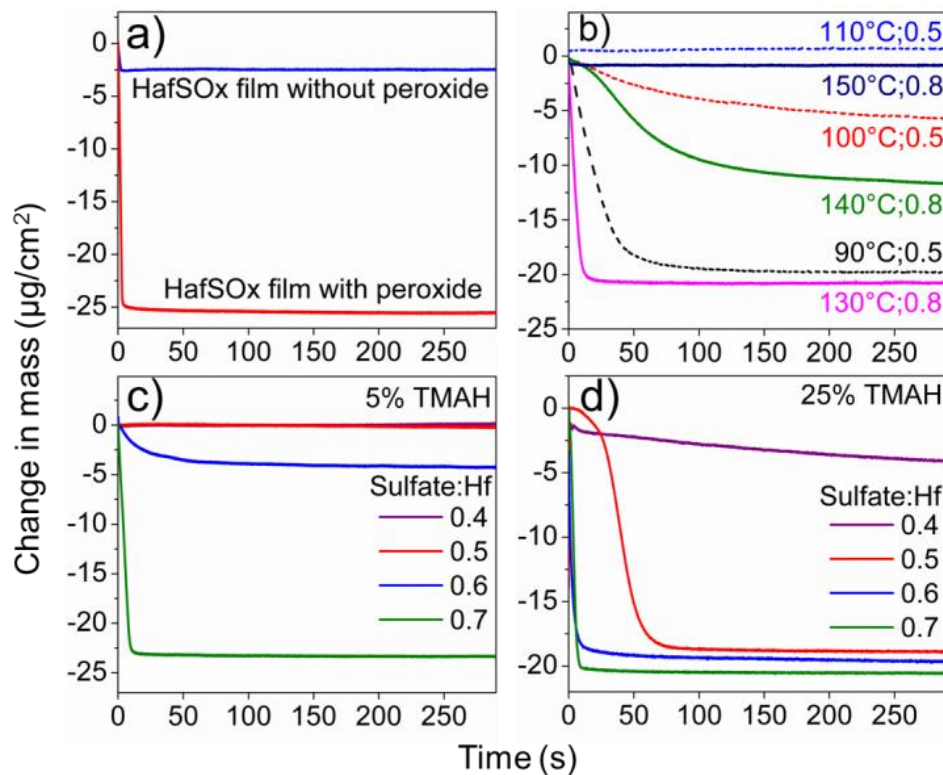


**Figure 8.4.** QCM measurements of the dissolution of (a) HafSOx films with and without peroxide developed in 5% TMAH. (b) HafSOx films with sulfate: Hf ratio of 0.5 and 0.8 annealed at increasing temperatures and developed in 25% TMAH. (c) HafSOx films with increasing sulfate: Hf ratio developed in 5% TMAH. (d) HafSOx films with increasing sulfate: Hf ratio developed in 25% TMAH.

temperature is another important factor that changes solubility. Figure 8.4b show that films quickly transition from soluble to insoluble with only a 20 °C increase in the soft bake temperature. The minimal amount of energy required to significantly change the solubility of HafSO<sub>x</sub> explains the high sensitivity of this material relative to other non-chemically amplified resists.<sup>14-16</sup> Figures 8.4c and 8.4d present data for films made with different amounts of sulfate. Films with more sulfate etch more quickly while films with too little sulfate are largely insoluble. This is consistent with the XPS results that indicate the formation of Hf-O-Hf networks at low hafnium to sulfate ratios, as well as the solubility trends of hafnium sulfate salts. Neutral hafnium sulfates (salts without hydroxyl groups with a sulfate to hafnium ratio of 2) such as Hf(SO<sub>4</sub>)<sub>2</sub>·nH<sub>2</sub>O are highly soluble whereas the basic salts (salts with hydroxyl groups with a sulfate to hafnium ratio less than 2) such as Hf(OH)<sub>2</sub>SO<sub>4</sub>·nH<sub>2</sub>O tend to be less soluble. Comparing figures 8.4c with 8.4d indicates that films are also more soluble in more concentrated TMAH developer.

The results from the XPS and QCM studies indicate that the solubility of HafSO<sub>x</sub> films is controlled by a number of variables including the addition of peroxide, amount of sulfate, annealing temperature, and concentration of the TMAH developer. Important resist properties such as resolution and sensitivity can also be optimized by controlling these same variables. Figures 8.5a and 8.5b show SEM images of arrays that were patterned into a HafSO<sub>x</sub> film using electron beam lithography. The squares are patterned using an electron beam dose which increases from 100 to 1500 μC/cm<sup>2</sup> in increments of 40 μC. Similar arrays were imaged by AFM to produce the contrast curve shown in Figure 8.5c. For low doses, the films remain soluble. The dose at which the films become insoluble

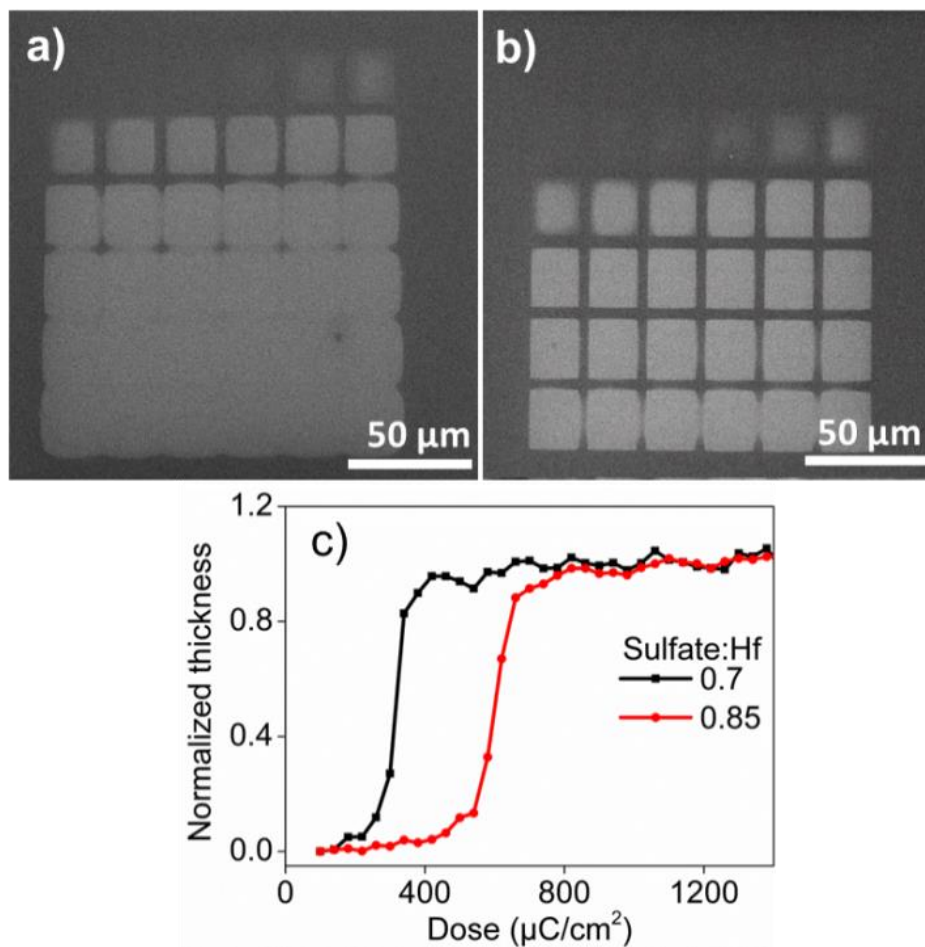


**Figure 8.5.** (a-b) SEM images of contrast arrays generated by patterning films with increasing electron beam exposure doses. The HafSO<sub>x</sub> films have sulfate:Hf ratios of (a) 0.7 (b) 0.85. (c) Contrast curve generated from AFM images of contrast arrays similar to those shown in (a-b).

(resist sensitivity) is easily tuned by changing the amount of sulfate in the resist. The films with lower sulfate concentrations (Figure 8.5a) were more sensitive than the film with higher sulfate concentrations (Figure 8.5b), but it was found that this increase in sensitivity comes at the expense of resolution.

Table 8.1 summarizes the XPS analysis of  $\text{HafSO}_x$  films made with different amounts of sulfate and presents an approximate film stoichiometry. The stoichiometry was derived using the composition determined by XPS and the requirement for overall charge balance for the film. In this analysis 0.5 peroxide groups are included for each hafnium, based on our Raman spectroscopy results. Film condensation is governed by two competing mechanisms. Condensation can occur thermally through the hydroxyl groups or it can proceed via a radiation stimulated pathway through the decomposition of peroxide groups. For a fixed peroxide concentration, the amount of sulfate can be adjusted over a wide range. Increasing the amount of sulfate in the films reduces the number of oxide and hydroxide groups which drive condensation. Changing the amount of sulfate in the films is, therefore, one means to control film solubility and resist sensitivity. Similarly, resolution and other resist properties can be optimized through careful control of the coordination of the different ligands (peroxide, sulfate, oxide, and hydroxide). One limitation of the  $\text{HafSO}_x$  system is the relatively small number of peroxide groups that can coordinate to hafnium. This likely limits the sensitivity which can be achieved with this material. Metal ions which can coordinate to multiple peroxide ligands such as chromium, molybdenum, or tungsten may be of interest for increasing the sensitivity of this family of inorganic resists.

**Table 8.1.** Normalized atomic percent of Hf, O, S for HafSO<sub>x</sub> films with increasing sulfate:Hf molar ratios from XPS analysis. An approximate film stoichiometry derived from the XPS composition is also shown.

Sulfate: Hf ratio in precursor solution	Hf (at.%)	O (at.%)	S (at.%)	approximate stoichiometry
0.10	23	74	3	Hf(O <sub>2</sub> ) <sub>0.5</sub> (SO <sub>4</sub> ) <sub>0.14</sub> (OH) <sub>0.56</sub> O <sub>1.08</sub>
0.20	20	75	5	Hf(O <sub>2</sub> ) <sub>0.5</sub> (SO <sub>4</sub> ) <sub>0.25</sub> (OH) <sub>0.90</sub> O <sub>0.80</sub>
0.40	17	74	9	Hf(O <sub>2</sub> ) <sub>0.5</sub> (SO <sub>4</sub> ) <sub>0.51</sub> (OH) <sub>0.64</sub> O <sub>0.67</sub>
0.50	16	73	11	Hf(O <sub>2</sub> ) <sub>0.5</sub> (SO <sub>4</sub> ) <sub>0.65</sub> (OH) <sub>0.20</sub> O <sub>0.75</sub>
0.70	14	73	13	Hf(O <sub>2</sub> ) <sub>0.5</sub> (SO <sub>4</sub> ) <sub>0.86</sub> (OH) <sub>0.14</sub> O <sub>0.57</sub>

## **Conclusions**

Peroxo hafnium sulfate clusters offer a promising approach to nanoscale patterning because the small cluster size enables high resolution and low line edge roughness. Peroxide groups are effective capping ligands which limit condensation in the films and increase solubility prior to exposure. Peroxide ligands are decomposed by photon and electron radiation, resulting in controlled condensation in exposed regions and formation of an insoluble hafnium oxide network. The resolution and sensitivity of the HafSO<sub>x</sub> system are easily tuned by changes in the sulfate content of the films, annealing temperature, and concentration of the basic developer.

## **Author Information**

Corresponding Authors

\*E-mail: (E.L.G.) [egarf@rutgers.edu](mailto:egarf@rutgers.edu); (D.A.K.) [Douglas.Keszler@oregonstate.edu](mailto:Douglas.Keszler@oregonstate.edu)

## **Acknowledgments**

This material is based upon work in the Center for Sustainable Materials Chemistry, which is supported by the US National Science Foundation under grant number CHE-1102637. DWJ is a Scialog Fellow of Research Corporation for Science Advancement.

## References

- [1] Ito, H., Chemical amplification resists for microlithography. In *Microlithography - Molecular Imprinting*, Ito, H.; Marty, J. D.; Mauzak, M., Eds. Springer-Verlag Berlin: Berlin, 2005; Vol. 172, pp 37-245.
- [2] Yasin, S.; Hasko, D. G.; Ahmed, H., Fabrication of < 5 nm width lines in poly(methylmethacrylate) resist using a water : isopropyl alcohol developer and ultrasonically-assisted development. *Applied Physics Letters* **2001**, 78, (18), 2760-2762.
- [3] Duan, H. G.; Winston, D.; Yang, J. K. W.; Cord, B. M.; Manfrinato, V. R.; Berggren, K. K., Sub-10-nm half-pitch electron-beam lithography by using poly(methyl methacrylate) as a negative resist. *Journal of Vacuum Science & Technology B* **2010**, 28, (6), C6C58-C6C62.
- [4] Grigorescu, A. E.; Hagen, C. W., Resists for sub-20-nm electron beam lithography with a focus on HSQ: state of the art. *Nanotechnology* **2009**, 20, (29).
- [5] Manfrinato, V. R.; Zhang, L. H.; Su, D.; Duan, H. G.; Hobbs, R. G.; Stach, E. A.; Berggren, K. K., Resolution Limits of Electron-Beam Lithography toward the Atomic Scale. *Nano Letters* **2013**, 13, (4), 1555-1558.
- [6] Yoshimura, T.; Shiraishi, H.; Yamamoto, J.; Okazaki, S., Nano edge roughness in polymer resist patterns. *Applied Physics Letters* **1993**, 63, (6), 764-766.
- [7] Nagase, M.; Namatsu, H.; Kurihara, K.; Iwadate, K.; Murase, K.; Makino, T., Nano-scale fluctuations in electron beam resist pattern evaluated by atomic force microscopy. *Microelectronic Engineering* **1996**, 30, (1-4), 419-422.
- [8] Yamaguchi, T.; Namatsu, H.; Nagase, M.; Yamazaki, K.; Kurihara, K., Nanometer-scale linewidth fluctuations caused by polymer aggregates in resist films. *Applied Physics Letters* **1997**, 71, (16), 2388-2390.
- [9] Fujita, J.; Ohnishi, Y.; Ochiai, Y.; Matsui, S., Ultrahigh resolution of calixarene negative resist in electron beam lithography. *Applied Physics Letters* **1996**, 68, (9), 1297-1299.
- [10] Dai, J. Y.; Chang, S. W.; Hamad, A.; Yang, D.; Felix, N.; Ober, C. K., Molecular glass resists for high-resolution patterning. *Chemistry of Materials* **2006**, 18, (15), 3404-3411.
- [11] Namatsu, H.; Takahashi, Y.; Yamazaki, K.; Yamaguchi, T.; Nagase, M.; Kurihara, K., Three-dimensional siloxane resist for the formation of nanopatterns with minimum linewidth fluctuations. *Journal of Vacuum Science & Technology B* **1998**, 16, (1), 69-76.
- [12] Trikeriotis, M.; Krysak, M.; Chung, Y. S.; Ouyang, C.; Cardineau, B.; Brainard, R.; Ober, C. K.; Giannelis, E. P.; Cho, K., Nanoparticle Photoresists from HfO<sub>2</sub> and ZrO<sub>2</sub> for EUV Patterning. *Journal of Photopolymer Science and Technology* **2012**, 25, (5), 583-586.
- [13] Neisser, M.; Cho, K.; Petrillo, K., The Physics of EUV Photoresist and How It Drives Strategies for Improvement. *Journal of Photopolymer Science and Technology* **2012**, 25, (1), 87-94.
- [14] Stowers, J.; Keszler, D. A., High resolution, high sensitivity inorganic resists. *Microelectronic Engineering* **2009**, 86, (4-6), 730-733.

- [15] Telecky, A.; Xie, P.; Stowers, J.; Grenville, A.; Smith, B.; Keszler, D. A., Photopatternable inorganic hardmask. *Journal of Vacuum Science & Technology B* **2010**, 28, (6), C6S19-C6S22.
- [16] Stowers, J. K.; Telecky, A.; Kocsis, M.; Clark, B. L.; Keszler, D. A.; Grenville, A.; Anderson, C. N.; Naulleau, P. P. In *Directly patterned inorganic hardmask for EUV lithography*, Proc. SPIE 7969, Extreme Ultraviolet (EUV) Lithography II, 2011; 2011; pp 796915-796915.
- [17] Muha, G. M.; Vaughan, P. A., Structure of the Complex Ion in Aqueous Solutions of Zirconyl and Hafnyl Oxyhalides. *The Journal of Chemical Physics* **1960**, 33, (1), 194-199.
- [18] Aberg, M., X-ray investigations of some aqueous zirconium (IV) halide, an hafnium (IV) chloride, and some zirconium (IV) perchlorate solutions. *Acta Chemica Scandinavica Series A-Physical and Inorganic Chemistry* **1977**, 31, (3), 171-181.
- [19] Connick, R. E.; McVey, W. H., The Aqueous Chemistry of Zirconium. *Journal of the American Chemical Society* **1949**, 71, (9), 3182-3191.
- [20] Anderson, J. T.; Munsee, C. L.; Hung, C. M.; Phung, T. M.; Herman, G. S.; Johnson, D. C.; Wager, J. F.; Keszler, D. A., Solution-processed HafSO<sub>x</sub> and ZircSO<sub>x</sub> inorganic thin-film dielectrics and nanolaminates. *Advanced Functional Materials* **2007**, 17, (13), 2117-2124.
- [21] Pappas, I.; Fitzgerald, M.; Huang, X. Y.; Li, J.; Pan, L., Thermally Resolved in Situ Dynamic Light Scattering Studies of Zirconium(IV) Complex Formation. *Crystal Growth & Design* **2009**, 9, (12), 5213-5219.
- [22] Oliveri, A. F.; Elliott, E. W.; Carnes, M. E.; Hutchison, J. E.; Johnson, D. W., Elucidating Inorganic Nanoscale Species in Solution: Complementary and Corroborative Approaches. *Chemphyschem* **2013**, 14, (12), 2655-2661.
- [23] Chiavacci, L. A.; Santilli, C. V.; Pulcinelli, S. H.; Craievich, A. F., Thermostimulated sol-gel transition in suspensions of sulfate zirconium oxychloride. *Journal of Applied Crystallography* **1997**, 30, (2), 750-754.
- [24] Hu, Y.-J.; Knope, K. E.; Skanthakumar, S.; Kanatzidis, M. G.; Mitchell, J. F.; Soderholm, L., Understanding the Role of Aqueous Solution Speciation and Its Application to the Directed Syntheses of Complex Oxidic Zr Chlorides and Sulfates. *Journal of the American Chemical Society* **2013**, 135, (38), 14240-14248.
- [25] Dengel, A. C.; Griffith, W. P., Studies on transition metal peroxo complexes. 9. Carboxylato peroxo complexes of niobium (V), tantalum (V), zirconium (IV), and hafnium (IV). *Polyhedron* **1989**, 8, (11), 1371-1377.
- [26] Tarafder, M. T. H.; Miah, M. A. L., Novel peroxo complexes of zirconium containing organic ligands. *Inorganic Chemistry* **1986**, 25, (13), 2265-2268.
- [27] Tarafder, M. T. H.; Bhattacharjee, P.; Sarkar, A. K., Peroxo complexes of chromium(VI), molybdenum(VI), tungsten(VI) and zirconium(IV) ions containing tridentate and quadridentate neutral ligands. *Polyhedron* **1992**, 11, (7), 795-798.
- [28] Piquemal, J. Y.; Briot, E.; Bregeault, J. M., Preparation of materials in the presence of hydrogen peroxide: from discrete or "zero-dimensional" objects to bulk materials. *Dalton Transactions* **2013**, 42, (1), 29-45.

- [29] Malinowski, E. R.; Cox, R. A.; Haldna, U. L., Factor analysis for isolation of the Raman spectra of aqueous sulfuric acid components. *Analytical Chemistry* **1984**, 56, (4), 778-781.
- [30] Rudolph, W. W.; Brooker, M. H.; Tremaine, P. R., Raman spectroscopy of aqueous ZnSO<sub>4</sub> solutions under hydrothermal conditions: Solubility, hydrolysis, and sulfate ion pairing. *Journal of Solution Chemistry* **1999**, 28, (5), 621-630.
- [31] Szilagyi, I.; Konigsberger, E.; May, P. M., Characterization of Chemical Speciation of Titanyl Sulfate Solutions for Production of Titanium Dioxide Precipitates. *Inorganic Chemistry* **2009**, 48, (5), 2200-2204.
- [32] Thompson, R. C., Equilibrium studies and redox kinetics of the peroxo complex of zirconium (IV) in acidic perchlorate solution. *Inorganic Chemistry* **1985**, 24, (22), 3542-3547.
- [33] Vasquez, R. P., XPS core level spectra of some Y compounds *Journal of Electron Spectroscopy and Related Phenomena* **1990**, 50, (1-2), 167-170.
- [34] Colon, J. L.; Thakur, D. S.; Yang, C. Y.; Clearfield, A.; Martin, C. R., X-ray photoelectron spectroscopy and catalytic activity of alpha-zirconium phosphate and zirconium phosphate sulfophenylyphosphonate. *Journal of Catalysis* **1990**, 124, (1), 148-159.
- [35] Barreca, D.; Milanov, A.; Fischer, R. A.; Devi, A.; Tondello, E., Hafnium oxide thin film grown by ALD: An XPS study. *Surface Science Spectra* **2007**, 14, (1), 34-40.
- [36] Shimizu, H.; Sato, T.; Konagai, S.; Ikeda, M.; Takahashi, T.; Nishide, T., Temperature-programmed desorption analyses of sol-gel deposited and crystallized HfO<sub>2</sub> films. *Japanese Journal of Applied Physics Part 1-Regular Papers Brief Communications & Review Papers* **2007**, 46, (7A), 4209-4214.
- [37] Flynn, B.; Kim, D.; Clark, B. L.; Telecky, A.; Arnadottir, L.; Szanyi, J.; Keszler, D. A.; Herman, G. S., In-situ characterization of aqueous-based hafnium oxide hydroxide sulfate thin films. *Surface and Interface Analysis* **2013**.
- [38] Sarma, D. D.; Rao, C. N. R., XPES studies of oxides of second- and third-row transition metals including rare earths. *Journal of Electron Spectroscopy and Related Phenomena* **1980**, 20, (1-2), 25-45.
- [39] Hinsberg, W. D.; Willson, C. G.; Kanazawa, K. K., Measurement of thin-film dissolution kinetics using a quartz crystal microbalance. *Journal of the Electrochemical Society* **1986**, 133, (7), 1448-1451.
- [40] Hinsberg, W.; Houle, F. A.; Lee, S. W.; Ito, H.; Kanazawa, K., Characterization of reactive dissolution and swelling of polymer films using a quartz crystal microbalance and visible and infrared reflectance spectroscopy. *Macromolecules* **2005**, 38, (5), 1882-1898.

## Conclusions

The preceding body of work has explored a small part of the diverse chemistry of hafnium. The focus on aqueous processing of hafnium for the purpose of thin-film applications has been shown to offer a sustainable approach to today's problems. The elucidation of the thermal mechanisms for two precursors and the incorporation of other elements into these systems show there is a nearly endless potential for the continuation of this work. The uses of aqueous processed hafnium based thin films for the applications of preventing rehydration of a dielectric as well as the mechanisms behind the lithographic processes for  $\text{HfSO}_x$  have also been covered.

For continuation of this work the incorporation of pulsed laser annealing or microwave annealing for the dehydration of films from the  $\text{HfNO}_x$  solution is recommended. For the alkaline hafnia precursor, further investigation into purification and film morphology are critical next steps to understanding this material. This work should also be followed up with electrical characterization for investigation as a possible dielectric.

The work on  $\text{HfSO}_x$  should focus primarily on the nature of the peroxide bonding environment and the removal of chlorine as a means to extend the shelf life of the precursor.

For all systems, an understanding of the transition from isolated cluster to continuous film should be studied using pair distribution function (PDF). As this technique is new for thin-film analysis, the large  $Z$  of hafnium would make it a great material for early development of the technique.

**Bibliography**

- [1] Aberg, M.; Glaser, J. *Inorganica Chim. Acta* **1993**, *206*, 53–61.
- [2] Aberg, M., X-ray investigations of some aqueous zirconium (IV) halide, an hafnium (IV) chloride, and some zirconium (IV) perchlorate solutions. *Acta Chemica Scandinavica Series A-Physical and Inorganic Chemistry* **1977**, *31*, (3), 171-181.
- [3] Anderson, J. T.; Wang, W.; Jiang, K.; Gustafsson, T.; Xu, C.; Gafunkel, E. L.; Keszler, D. A. *ACS Sustain. Chem. Eng.* **2015**, *3* (6), 1081–1085.
- [4] Anderson, J.T.; Munsee, C.L.; Hung, C.M.; Phung, T.M.; Herman, G.S., Johnson, D.C.; Wager, J.F.; Keszler, D.A., Solution Processed HafSO<sub>x</sub> and ZircSO<sub>x</sub> Inorganic Thin-Film Dielectrics and Nanolaminates, *Adv. Funct. Mater.* **17**, 2117-2124 (2007).
- [5] Arai, Y.; Sparks, D. L. *J. Colloid Interface Sci.* **2001**, *241* (2), 317–326.
- [6] Ateshian, G. A.; Maas, S.; Weiss, J. A. *J. Biomech.* **2012**, *45* (6), 1023–1027.
- [7] Banger, K. K.; Yamashita, Y.; Mori, K.; Peterson, R. L.; Leedham, T.; Rickard, J.; Siringhaus, H. *Nat. Mater.* **2011**, *10*, 45–50.
- [8] Barreca, D.; Milanov, A.; Fischer, R. A.; Devi, A.; Tondello, E., Hafnium oxide thin film grown by ALD: An XPS study. *Surface Science Spectra* **2007**, *14*, (1), 34-40.
- [9] Bartlett, J.; Woolfrey, J.; Percy, M. *J. Sol-Gel ...* **1994**, *220*, 215–220.
- [10] Breitkopf, C.; Papp, H.; Li, X.; Olindo, R.; Lercher, J. A.; Lloyd, R.; Wrabetz, S.; Jentoft, F. C.; Meinel, K.; Förster, S.; Schindler, K.-M.; Neddermeyer, H.; Widdra, W.; Hofmann, A.; Sauer, J. Activation and isomerization of n-butane on sulfated zirconia model systems – An integrated study across the materials and pressure gaps. *Phys. Chem. Chem. Phys.* **2007**, *9*, 3600–3618.
- [11] Brinker, C. J.; Sherrer, G. W. *Sol-Gel Science*; Academic Press: New York, 1990.
- [12] Broers, A. N.; Hoole, A. C. F.; Ryan, J. M. Electron beam lithography Resolution limits. *Microelectron. Eng.* **1996**, *32*, 131–142.
- [13] Chen, W.; Ahmed, H. Fabrication of 5–7 nm wide etched lines in silicon using 100 keV electron beam lithography and polymethylmethacrylate resist. *Appl. Phys. Lett.* **1993**, *62*, 1499–1501
- [14] Chiavacci, L. A.; Santilli, C. V.; Pulcinelli, S. H.; Craievich, A. F., Thermostimulated sol-gel transition in suspensions of sulfate zirconium oxychloride. *Journal of Applied Crystallography* **1997**, *30*, (2), 750-754.
- [15] Choi, J. H.; Mao, Y.; Chang, J. P. *Mater. Sci. Eng. R Reports* **2011**, *72*, 97–136.
- [16] Colon, J. L.; Thakur, D. S.; Yang, C. Y.; Clearfield, A.; Martin, C. R., X-ray photoelectron spectroscopy and catalytic activity of alpha-zirconium phosphate and zirconium phosphate sulfophenylyphosphonate. *Journal of Catalysis* **1990**, *124*, (1), 148-159.
- [17] Connick, R. E.; McVey, W. H., The Aqueous Chemistry of Zirconium. *Journal of the American Chemical Society* **1949**, *71*, (9), 3182-3191.

- [18] Dai, J. Y.; Chang, S. W.; Hamad, A.; Yang, D.; Felix, N.; Ober, C. K., Molecular glass resists for high-resolution patterning. *Chemistry of Materials* **2006**, 18, (15), 3404-3411.
- [19] Danek, M.; Jensen, K. F.; Murray, C. B.; Bawendi, M. G. *Chem. Mater.* **1996**, 8, 173–180.
- [20] Dengel, A. C.; Griffith, W. P., Studies on transition metal peroxo complexes. 9. Carboxylato peroxo complexes of niobium (V), tantalum (V), zirconium (IV), and hafnium (IV). *Polyhedron* **1989**, 8, (11), 1371-1377.
- [21] Dickman, M. H.; Pope, M. T. Peroxo and Superoxo Complexes of Chromium, Molybdenum, and Tungsten. *Chem. Rev.* **94**, 579-584 (1994).
- [22] Duan, H. G.; Winston, D.; Yang, J. K. W.; Cord, B. M.; Manfrinato, V. R.; Berggren, K. K., Sub-10-nm half-pitch electron-beam lithography by using poly(methyl methacrylate) as a negative resist. *Journal of Vacuum Science & Technology B* **2010**, 28, (6), C6C58-C6C62.
- [23] Ekinci, Y.; Vockenhuber, M.; Terhalle, B.; Hojeij, M.; Wang, L.; Younkin, T. R. Evaluation of resist performance with EUV interference lithography for sub-22 nm patterning. *Proc. SPIE* **8322**, 83220W (2012).
- [24] Ekinci, Y.; Vockenbuder, M.; Hojeij, M.; Wang, L.; Mojarad, N. M. Evaluation of EUV resist performance with interference lithography towards 11 nm half-pitch and beyond. *Proc. SPIE* 2013, 8679, 867910–867910.
- [25] Fairley, K. C.; Merrill, D. R.; Woods, K. N.; Ditto, J.; Xu, C.; Oleksak, R. P.; Gustafsson, T.; Johnson, D. W.; Garfunkel, E. L.; Herman, G. S.; Johnson, D. C.; Page, C. J. *ACS Appl. Mater. Interfaces* **2016**, 8, 667–672.
- [26] Flynn, B.; Kim, D.; Clark, B. L.; Telecky, A.; Arnadottir, L.; Szanyi, J.; Keszler, D. A.; Herman, G. S. In-situ characterization of aqueous-based hafnium oxide hydroxide sulfate thin films. *Surf. Interface Anal.* 2013, DOI: 10.1002/sia.5205.
- [27] Fujita, J.; Ohnishi, Y.; Ochiai, Y.; Matsui, S., Ultrahigh resolution of calixarene negative resist in electron beam lithography. *Applied Physics Letters* **1996**, 68, (9), 1297-1299.
- [28] Gálvez-barboza, S.; González, L. A.; Puente-urbina, B. A.; Saucedo-salazar, E. M.; García-cerda, L. A. **2015**, 643, 62–66.
- [29] Goberna-Ferron, S.; Park, D. H.; Amador, J. M.; Keszler, D. A.; Nyman, M. *Angew. Chemie - Int. Ed.* **2016**, 55, 6221–6224.
- [30] Goodman, A. L.; Bernard, E. T.; Grassian, V. H. *J. Phys. Chem. A* **2001**, 105 (26), 6443–6457.
- [31] Grigorescu, A. E.; Hagen, C. W., Resists for sub-20-nm electron beam lithography with a focus on HSQ: state of the art. *Nanotechnology* **2009**, 20, (29).
- [32] Guha, S.; Yang, J.; Williamson, D. L.; Lubianiker, Y.; Cohen, J. D.; Mahan, a. H. *Appl. Phys. Lett.* **1999**, 74 (13), 1860.
- [33] Hagfeldt, C.; Kessler, V.; Persson, I. *R. Soc. Chem.* **2004**.
- [34] Hale, J.; Johs, B. *CompleteEase*; J. A. Wollam: Lincoln, NE, 2012.
- [35] Haller, I.; Hatzakis, M.; Srinivasan, R. High-resolution positive resists for electron-beam exposure. *IBM J. Res. Dev.* 1968, 12, 251–256.
- [36] He, W.; Zhang, L.; Chan, D. S. H.; Cho, B. J. **2009**, 30, 623–625.

- [37] Henderson, M. A. The interaction of water with solid surfaces: Fundamental aspects revisited. *Surf. Sci. Rep.* 2002, 46, 1–308.
- [38] Heiland, K.; Kaminsky, W. *Makromol. Chem.* **1992**, 193, 601–610.
- [39] Henry, M.; Jolivet, J. P.; Livage, J. *Chem. Spectrosc. Appl. Sol-Gel Glas.* **1992**, 77, 153–206.
- [40] Herman, G. S.; Kim, Y. J.; Chambers, S. A.; Peden, C. H. F. Interaction of D<sub>2</sub>O with CeO<sub>2</sub>(001) investigated by temperature programmed desorption and X-ray photoelectron spectroscopy. *Langmuir* 2009, 15, 3993–3997.
- [41] Hinsberg, W. D.; Willson, C. G.; Kanazawa, K. K., Measurement of thin-film dissolution kinetics using a quartz crystal microbalance. *Journal of the Electrochemical Society* **1986**, 133, (7), 1448-1451.
- [42] Hinsberg, W.; Houle, F. A.; Lee, S. W.; Ito, H.; Kanazawa, K., Characterization of reactive dissolution and swelling of polymer films using a quartz crystal microbalance and visible and infrared reflectance spectroscopy. *Macromolecules* **2005**, 38, (5), 1882-1898.
- [43] Hino, M.; Kurashige, M.; Matsushashi, H.; Arata, K. The surface structure of sulfated zirconia: Studies of XPS and thermal analysis. *Thermochim. Acta* 2006, 441, 35–41.
- [44] Hou, Y.; Fast, D. B.; Ruther, R. E.; Amador, J. M.; Fullmer, L. B.; Decker, S. R.; Zakharov, L. N.; Dolgos, M. R.; Nyman, M. *J. Solid State Chem.* **2015**, 221, 418–425.
- [45] Houssa, M.; Pourtois, G.; Heyns, M. M.; Stesmans, a. *J. Phys. Condens. Matter* **2005**, 17 (21), S2075–S2088.
- [46] Hu, M. Z.-C.; Harris, M. T.; Byers, C. H. *J. Colloid Interface Sci.* **1998**, 198, 87–99.
- [47] Hu, Y.-J.; Knope, K. E.; Skanthakumar, S.; Kanatzidis, M. G.; Mitchell, J. F.; Soderholm, L., Understanding the Role of Aqueous Solution Speciation and Its Application to the Directed Syntheses of Complex Oxidic Zr Chlorides and Sulfates. *Journal of the American Chemical Society* **2013**, 135, (38), 14240-14248.
- [48] Huckaba, C. E.; Keyes, F. G. The Accuracy of Estimation of Hydrogen Peroxide by Potassium Permanagate Titration. *J. Am. Chem. Soc.* **70**, 1640-1644 (1948).
- [49] Ilavsky, J.; Jemian, P. R. *J. Appl. Crystallogr.* **2009**, 42, 347–353.
- [50] Ito, H., Chemical amplification resists for microlithography. In *Microlithography - Molecular Imprinting*, Ito, H.; Marty, J. D.; Mauzak, M., Eds. Springer-Verlag Berlin: Berlin, 2005; Vol. 172, pp 37-245.
- [51] Jeong, W. H.; Kim, D. L.; Kim, H. J. *ACS Appl. Mater. Interfaces* **2013**, 5 (18), 9051–9056.
- [52] Jiang, K.; Anderson, J. T.; Hoshino, K.; Li, D.; Wager, J. F.; Keszler, D. a. *Chem. Mater.* **2011**, 23, 945–952.
- [53] Jiang, K.; Meyers, S. T.; Anderson, M. D.; Johnson, D. C.; Keszler, D. A. *Chem. Mater.* **2013**, 25 (2), 210–214.
- [54] Jun, T.; Song, K.; Jeong, Y.; Woo, K.; Kim, D.; Bae, C.; Moon, J. *J. Mater. Chem.* **2011**, 21 (4), 1102–1108.
- [55] Kakihana, M.; Kobayashi, M.; Tomita, K.; Petrykin, V. *Bull. Chem. Soc. Jpn.*

- 2010**, 83, 1285–1308.
- [56] Kalaji, A.; Soderholm, L. *Chem. Commun. (Camb)*. **2014**, 50, 997–999.
- [57] Kalaji, A.; Soderholm, L. *Inorg. Chem.* **2014**, 53, 11252–11260.
- [58] Kanazhevskii, V. V.; Kotsarenko, N. S.; Kolomiichuk, V. N. **2011**, 52, 80–87.
- [59] Kast, M. G.; Cochran, E. A.; Enman, L. J.; Mitchson, G.; Ditto, J.; Siefe, C.; Plassmeyer, P. N.; Greenaway, A. L.; Johnson, D. C.; Page, C. J.; Boettcher, S. W. *J. Am. Chem. Soc.* **2016**, 138, 16800–16808.
- [60] Kwon, J.; Dai, M.; Halls, M. D.; Langereis, E.; Chabal, Y. J.; Gordon, R. G. *J. Phys. Chem. C* **2009**, 113 (2), 654–660.
- [61] Lakiza, S. M.; Tyschenko, J. S.; Lopato, L. M. *J. Eur. Ceram. Soc.* **2011**, 31, 1285–1291.
- [62] Li, F. M.; Bayer, B. C.; Hofmann, S.; Dutson, J. D.; Wakeham, S. J.; Thwaites, M. J.; Milne, W. I.; Flewitt, A. J.; Li, F. M.; Bayer, B. C.; Hofmann, S.; Dutson, J. D.; Wakeham, S. J.; Thwaites, M. J.; Milne, W. I.; Flewitt, A. J. **2012**, 252903.
- [63] Lin, Y. S.; Puthenkovilakam, R.; Chang, J. P. *Appl. Phys. Lett.* **2002**, 81, 2041–2043.
- [64] Lupina, G.; Kozlowski, G.; Dudek, P.; Dabrowski, J.; Wenger, C.; Lippert, G.; Müssig, H. J. *ULIS 2008 - 9th Int. Conf. Ultim. Integr. Silicon* **2008**, 159–162.
- [65] Lysaght, P. S.; Foran, B.; Bersuker, G.; Peterson, J. J.; Young, C. D.; Majhi, P.; Lee, B. H.; Huff, H. R. *Appl. Phys. Lett.* **2005**, 87, 85–88.
- [66] Lomenzo, P. D.; Zhao, P.; Takmeel, Q.; Moghaddam, S.; Nishida, T.; Nelson, M.; Fancher, C. M.; Grimley, E. D.; Sang, X.; Lebeau, J. M.; Jones, J. L.; Lomenzo, P. D.; Zhao, P.; Takmeel, Q.; Moghaddam, S.; Nelson, M.; Fancher, C. M.; Grimley, E. D.; Sang, X.; Lebeau, J. M.; Jones, J. L. **2016**, 123, 0–8.
- [67] Malinowski, E. R.; Cox, R. A.; Haldna, U. L., Factor analysis for isolation of the Raman spectra of aqueous sulfuric acid components. *Analytical Chemistry* **1984**, 56, (4), 778-781.
- [68] Manfrinato, V. R.; Zhang, L. H.; Su, D.; Duan, H. G.; Hobbs, R. G.; Stach, E. A.; Berggren, K. K., Resolution Limits of Electron-Beam Lithography toward the Atomic Scale. *Nano Letters* **2013**, 13, (4), 1555-1558.
- [69] Manning, W. R. **1978**, 2–7.
- [70] Mansergh, R. H.; Fullmer, L. B.; Park, D. H.; Nyman, M.; Keszler, D. A. *Chem. Mater.* **2016**, 28, 1553–1558.
- [71] Meyers, S. T.; Anderson, J. T.; Hong, D.; Hung, C. M.; Wager, J. F.; Keszler, D. A. *Chem. Mater.* **2007**, 19 (16), 4023–4029.
- [72] Mi, Q.; Ping, Y.; Li, Y.; Cao, B.; Brunschwig, B. S.; Khalifah, P. G.; Galli, G. a; Gray, H. B.; Lewis, N. S. *J. Am. Chem. Soc.* **2012**, 134, 18318–18324.
- [73] Mitzi, D. B. *J. Mater. Chem.* **2004**, 14 (15), 2355–2365.
- [74] Montaudo, G.; Puglisi, C.; Samperi, F. *Polym. Degrad. Stab.* **1993**, 42, 13–28.
- [75] Moreno, T. Moran Lopez, M.A.; Huerta Illera, I.; Piqueras, C.M.; Sanz Arranz, A.; Garcia Serna, J.; Cocero, M.J. Quantitative Raman determination of hydrogen peroxide using the solvent as internal standard: Online application in the direct synthesis of hydrogen peroxide. *Chem. Eng. J.* **166**, 1061-1065 (2011).
- [76] Morris, J. E. **2012**, 1–27.

- [77] Moreau, W. M. *Semiconductor Lithography: Principles, Practices, and Materials*; Plenum Publishing Corp.: semiconductor Lithography: Principles and Materials., 1988.
- [78] Muha, G. M.; Vaughan, P. A., Structure of the Complex Ion in Aqueous Solutions of Zirconyl and Hafnyl Oxyhalides. *The Journal of Chemical Physics* **1960**, 33, (1), 194-199.
- [79] Müller, J.; Schröder, U.; Böske, T. S.; Müller, I.; Böttger, U.; Wilde, L.; Sundqvist, J.; Lemberger, M.; Kücher, P.; Mikolajick, T.; Frey, L. *J. Appl. Phys.* **2011**, 110, 114113.
- [80] Murari, N. M.; Mansergh, R. H.; Huang, Y.; Kast, M. G.; Keszler, D. A.; Conley, J. F. *J. Mater. Res.* **2016**, 31, 3303–3312.
- [81] Nagase, M.; Namatsu, H.; Kurihara, K.; Iwadate, K.; Murase, K.; Makino, T., Nano-scale fluctuations in electron beam resist pattern evaluated by atomic force microscopy. *Microelectronic Engineering* **1996**, 30, (1-4), 419-422.
- [82] Namatsu, H.; Takahashi, Y.; Yamazaki, K.; Yamaguchi, T.; Nagase, M.; Kurihara, K. Three-dimensional siloxane resist for the formation of nanopatterns with minimum linewidth fluctuations. *J. Vac. Sci. Technol., B: Microelectron. Nanometer Struct. Process., Meas., Phenom.* 1998, 16, 69–76.
- [83] Neisser, M.; Cho, K.; Petrillo, K., The Physics of EUV Photoresist and How It Drives Strategies for Improvement. *Journal of Photopolymer Science and Technology* **2012**, 25, (1), 87-94.
- [84] Nishida, T.; Notomi, M.; Iga, R.; Tamamura, T. Quantum wire fabrication by e-beam lithography using high-resolution and high-sensitivity e-beam resist ZEP-520. *Jpn. J. Appl. Phys., Part 1* 1992, 31, 4508–4514.
- [85] Nyman, M.; Burns, P. C. *Chem. Soc. Rev.* **2012**, 41, 7354.
- [86] Okamoto, H.; Ishikawa, A.; Kudo, T. Photoresist characteristics and their reaction mechanism for crystalline peroxopolytungstic acid. *J. Electrochem. Soc.* 1989, 136,
- [87] Oleksak, R. P.; Ruther, R. E.; Luo, F.; Fairley, K. C.; Decker, S. R.; Stickle, W. F.; Johnson, D. W.; Garfunkel, E. L.; Herman, G. S.; Keszler, D. A. *ACS Appl. Mater. Interfaces* **2014**, 6 (4), 2917–2921.
- [88] Oliveri, A. F.; Elliott, E. W.; Carnes, M. E.; Hutchison, J. E.; Johnson, D. W., Elucidating Inorganic Nanoscale Species in Solution: Complementary and Corroborative Approaches. *Chemphyschem* **2013**, 14, (12), 2655-2661.
- [89] Olsen, T.; Schröder, U.; Müller, S.; Krause, a.; Martin, D.; Singh, a.; Müller, J.; Geidel, M.; Mikolajick, T. *Appl. Phys. Lett.* **2012**, 101.
- [90] Pappas, I.; Fitzgerald, M.; Huang, X. Y.; Li, J.; Pan, L., Thermally Resolved in Situ Dynamic Light Scattering Studies of Zirconium(IV) Complex Formation. *Crystal Growth & Design* **2009**, 9, (12), 5213-5219.
- [91] Park, J. H.; Kim, K.; Yoo, Y. B.; Park, S. Y.; Lim, K.-H.; Lee, K. H.; Baik, H. K.; Kim, Y. S. *J. Mater. Chem. C* **2013**, 1 (43), 7166–7174.
- [92] Park, J. S.; Jeong, J. K.; Chung, H. J.; Mo, Y. G.; Kim, H. D. *Appl. Phys. Lett.* **2008**, 92 (7), 34–36.
- [93] Park, S. *Science (80-. )*. **2002**, 297, 65–65
- [94] Pavunny, S. P.; Sharma, Y.; Kooriyattil, S.; Dugu, S.; Katiyar, R. K.; Scott, J. F.;

- Katiyar, R. S. *Appl. Phys. Lett.* **2015**, *106*.
- [95] Piquemal, J. Y.; Briot, E.; Bregeault, J. M., Preparation of materials in the presence of hydrogen peroxide: from discrete or "zero-dimensional" objects to bulk materials. *Dalton Transactions* **2013**, 42, (1), 29-45.
- [96] Pope, M. T.; Müller, A. *Angew. Chem. Int. Ed. Engl.* **1991**, *30*, 34-48.
- [97] Rauwel, P.; Rauwel, E.; Persson, C.; Sunding, M. F.; Galeckas, A.; Rauwel, P.; Rauwel, E.; Persson, C.; Sunding, M. F.; Galeckas, A. **2014**, *104107*.
- [98] Risovanyi, V. D.; Klochkov, E. P.; Varlashova, E. E. *At. Energy* **1996**, *81*, 764-769.
- [99] Robertson, J. *Reports Prog. Phys.* **2006**, *69*, 327-396.
- [100] Rudolph, W. W.; Brooker, M. H.; Tremaine, P. R., Raman spectroscopy of aqueous ZnSO<sub>4</sub> solutions under hydrothermal conditions: Solubility, hydrolysis, and sulfate ion pairing. *Journal of Solution Chemistry* **1999**, *28*, (5), 621-630.
- [101] Sayan, S.; Garfunkel, E.; Nishimura, T.; Schulte, W. H.; Gustafsson, T.; Wilk, G. D. *J. Appl. Phys.* **2003**, *94*, 928.
- [102] Saifullah, M. S. M.; Khan, M. Z. R.; Hasko, D. G.; Leong, E. S. P.; Neo, X. L.; Goh, E. T. L.; Anderson, D.; Jones, G. A. C.; Welland, M. E. Spin-coatable HfO<sub>2</sub> resist for optical and electron beam lithographies. *J. Vac. Sci. Technol., B: Microelectron. Nanometer Struct. Process., Meas., Phenom.* 2010, *28*, 90-95.
- [103] Sarma, D. D.; Rao, C. N. R., XPS studies of oxides of second- and third-row transition metals including rare earths. *Journal of Electron Spectroscopy and Related Phenomena* **1980**, *20*, (1-2), 25-45.
- [104] Schneider, J. M.; Anders, A.; Hjorvarsson, B.; Petrov, I.; Macak, K.; Helmersson, U.; Sundgren, J.-E. *Appl. Phys. Lett.* **1999**, *74* (2), 200-202.
- [105] Shannon, R. D. *Acta Crystallogr. Sect. A* **1976**, *32*, 751-767.
- [106] Shi, N.; Ramprasad, R. *Appl. Phys. Lett.* **2007**, *91*.
- [107] Shimizu, H.; Sato, T.; Konagai, S.; Ikeda, M.; Takahashi, T.; Nishide, T., Temperature-programmed desorption analyses of sol-gel deposited and crystallized HfO<sub>2</sub> films. *Japanese Journal of Applied Physics Part 1-Regular Papers Brief Communications & Review Papers* **2007**, *46*, (7A), 4209-4214.
- [108] Smith, S. W.; Wang, W.; Keszler, D. A.; Conley, J. F. *J. Vac. Sci. Technol. A Vacuum, Surfaces, Film.* **2014**, *32*, 41501.
- [109] Southon, P.; Bartlett, J. *Chem. ...* **2002**, 4313-4319.
- [110] Stowers, J. K.; Telecky, A.; Kocsis, M.; Clark, B. L.; Keszler, D. A.; Grenville, A.; Anderson, C. N.; Naulleau, P. P. In *Directly patterned inorganic hardmask for EUV lithography*, Proc. SPIE 7969, Extreme Ultraviolet (EUV) Lithography II, 2011; 2011; pp 796915-796915.
- [111] Szilagy, I.; Konigsberger, E.; May, P. M., Characterization of Chemical Speciation of Titanyl Sulfate Solutions for Production of Titanium Dioxide Precipitates. *Inorganic Chemistry* **2009**, *48*, (5), 2200-2204.
- [112] Tanenbaum, D. M.; Lo, C. W.; Isaacson, M.; Craighead, H. G.; Rooks, M. J.; Lee, K. Y.; Huang, W. S.; Chang, T. H. P. High resolution electron beam lithography using ZEP520 and KRS resists at low voltage. *J. Vac. Sci. Technol., B: Microelectron. Nanometer Struct. Process. Meas., Phenom.* 1996, *14*, 3829-3833.
- [113] Tang, H.; Xiao, F.; Wang, D. *Adv. Colloid Interface Sci.* **2015**, *226*, 78-85.

- [114] Tang, J.; Fabbri, J.; Robinson, R. *Chem. Mater.* **2004**, 1336–1342.
- [115] Tarafder, M. T. H.; Miah, M. A. L., Novel peroxo complexes of zirconium containing organic ligands. *Inorganic Chemistry* **1986**, 25, (13), 2265-2268.
- [116] Tarafder, M. T. H.; Bhattacharjee, P.; Sarkar, A. K., Peroxo complexes of chromium(VI), molybdenum(VI), tungsten(VI) and zirconium(IV) ions containing tridentate and quadridentate neutral ligands. *Polyhedron* **1992**, 11, (7), 795-798.
- [117] Telecky, A.; Xie, P.; Stowers, J.; Grenville, A.; Smith, B.; Keszler, D.A. Photopatternable Inorganic Hardmask. *J. Vac. Sci. Technol.* **26**, (2010).
- [118] Thrun, X.; Choi, K. H.; Freitag, M.; Grenville, A.; Gutsch, M.; Hohle, C.; Stowers, J. K.; Bartha, J. W. Evaluation of direct patternable inorganic spin-on hard mask materials using electron beam lithography. *Microelectron. Eng.* 2012, 98, 226–229.
- [119] Thompson, R. C., Equilibrium studies and redox kinetics of the peroxo complex of zirconium (IV) in acidic perchlorate solution. *Inorganic Chemistry* **1985**, 24, (22), 3542-3547.
- [120] Trikeriotis, M.; Bae, W. J.; Schwartz, E.; Krysak, M.; Lafferty, N.; Xie, P.; Smith, B.; Zimmerman, P. A.; Ober, C. K.; Giannelis, E. P. Development of an inorganic photoresist for DUV, EUV, and electron beam imaging. *Proc. SPIE* 2010, 7639, 76390E–76390E.
- [121] Trikeriotis, M.; Krysak, M.; Chung, Y. S.; Ouyang, C.; Cardineau, B.; Brainard, R.; Ober, C. K.; Giannelis, E. P.; Cho, K., Nanoparticle Photoresists from HfO<sub>2</sub> and ZrO<sub>2</sub> for EUV Patterning. *Journal of Photopolymer Science and Technology* **2012**, 25, (5), 583-586.
- [122] Vasquez, R. P., XPS core level spectra of some Y compounds *Journal of Electron Spectroscopy and Related Phenomena* **1990**, 50, (1-2), 167-170.
- [123] View, C.; Carcenac, F.; Pepin, A.; Chen, Y.; Mejias, M.; Lebib, A.; Manin-Ferlazzo, L.; Couraud, L.; Launois, H. Electron beam lithography: Resolution limits and applications. *Appl. Surf. Sci.* 2000, 164, 111–117.
- [124] Wang, W.; Liu, W.; Chang, I.-Y.; Wills, L. A.; Zakharov, L. N.; Boettcher, S. W.; Cheong, P. H.-Y.; Fang, C.; Keszler, D. A. *Proc. Natl. Acad. Sci.* **2013**, 110, 18397–18401.
- [125] Wang, W.; Wentz, K.; Hayes, S. *Inorg. ...* **2011**, 13, 9–11.
- [126] Wiemer, C.; Lamagna, L.; Baldovino, S.; Perego, M.; Coulon, P. E.; Salicio, O.; Spiga, S.; Fanciulli, M.; Wiemer, C.; Lamagna, L.; Baldovino, S.; Perego, M. **2015**, 2, 27–30.
- [127] X-Ray and Vibrational Spectra of Sulfate in Earth Materials. *Reviews in Mineralogy and Geochemistry: Sulfate Minerals: Crystallography, Geochemistry, and Environmental Significance*, 1st ed.; The Mineralogical Society of America: Washington, DC, 2000: Vol. 40, pp 113-172.
- [128] Yamaguchi, T.; Namatsu, H.; Nagase, M.; Yamazaki, K.; Kurihara, K., Nanometer-scale linewidth fluctuations caused by polymer aggregates in resist films. *Applied Physics Letters* **1997**, 71, (16), 2388-2390.
- [129] Yasin, S.; Hasko, D. G.; Ahmed, H., Fabrication of < 5 nm width lines in poly(methylmethacrylate) resist using a water : isopropyl alcohol developer and

- ultrasonically-assisted development. *Applied Physics Letters* **2001**, 78, (18), 2760-2762.
- [131] Yoshimura, T.; Shiraishi, H.; Yamamoto, J.; Okazaki, S., Nano edge roughness in polymer resist patterns. *Applied Physics Letters* **1993**, 63, (6), 764-766.
- [132] Yuvaraj, S.; Lin, F. Y.; Chang, T. H.; Yeh, C. T. *J. Phys. Chem. B* **2003**, 107, 1044-1047.
- [133] Zhang, F.; Liu, G.; Liu, A.; Shin, B.; Shan, F. *Ceram. Int.* **2015**, 41, 13218-13223.
- [134] Zhou, G.; Wang, Z.; Zhou, B.; Zhao, Y.; Zhang, G.; Wang, S. *Opt. Mater. (Amst)*. **2013**, 35, 774-777.

## Appendix

### Supporting Information- Chapter 5

#### Aqueous process to limit hydration of thin-film inorganic dielectrics

Cory K. Perkins, Ryan H. Mansergh, Deok-Hie Park, Charith E. Nanayakkara, Juan C.

Ramos, Shawn R. Decker, Yu Huang, Yves J. Chabal, and Douglas A. Keszler\*

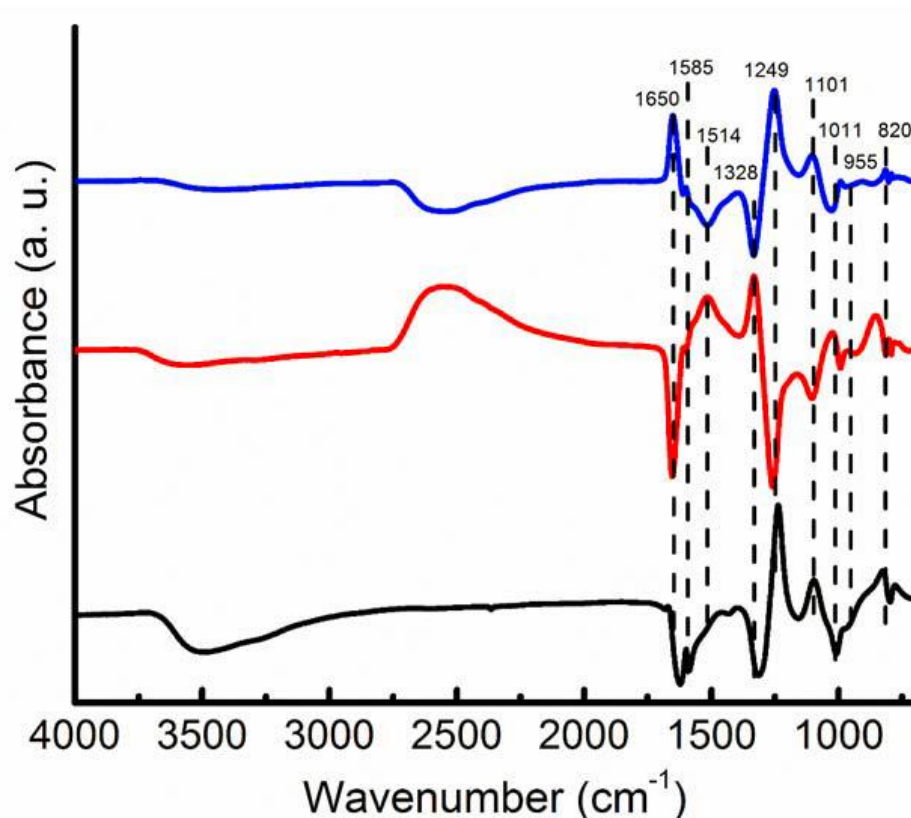


**Figure S1.** FTIR difference spectra obtained for as-synthesized AIPO film after annealing to 150 °C starting from 45 °C (black), after exposed to D<sub>2</sub>O (1.3 Torr × 60 s) (red) and after annealing to 150 °C by referencing to spectra after the previous treatment (blue). The absorbance spectra after 150 °C presented above were obtained by referencing the spectrum collected at 45 °C after annealing to 150 °C to the spectrum collected at 45 °C (before annealing). All the spectra were recorded at 45 °C. The thickness of the film was 42 nm after the *in-situ* treatment sequences of 150 °C anneal, D<sub>2</sub>O exposure, and 150 °C anneal steps.

The effect of having HfO<sub>2</sub> capping layer on water reabsorption for 120 nm AlPO films was highlighted using FTIR (Figure S2). The samples were loaded in an environmental chamber and annealed to 350 °C prior to exposure to heavy water (D<sub>2</sub>O). There was a substantial loss of OH/H<sub>2</sub>O after annealing to 350 °C for the uncapped film in contrast to the capped film (Figure S3). The spectra show no water resorption for the AlPO layer of the capped sample, consistent with the TPD data, as the area under the OD absorption band is smaller than the amount of water found in 20 nm HfO<sub>2</sub> only film. A higher uptake of water for the AlPO only film after the D<sub>2</sub>O exposure right after the 350 °C anneal was also observed, consistent with the TPD data.

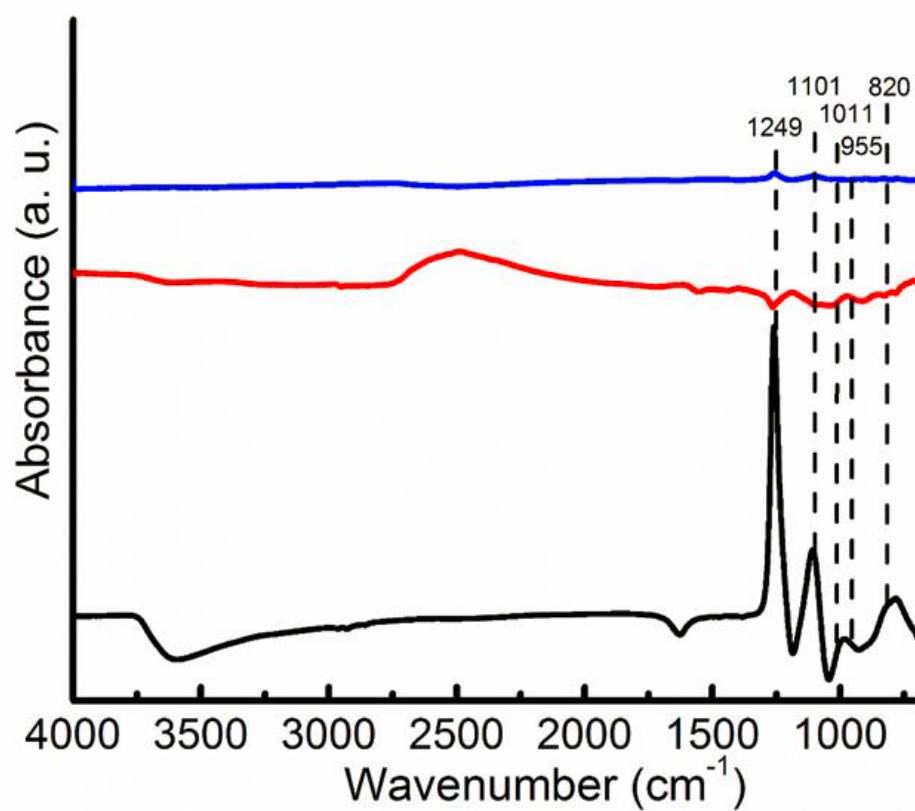


**Figure S2.** FTIR difference spectra obtained for a 120 nm AlPO film, after annealing to 350 °C (black), after exposed to  $\text{D}_2\text{O}$  (1.3 Torr  $\times$  60 s) (red) and after annealing to 150 °C (blue) by referencing to spectra after the previous treatment.

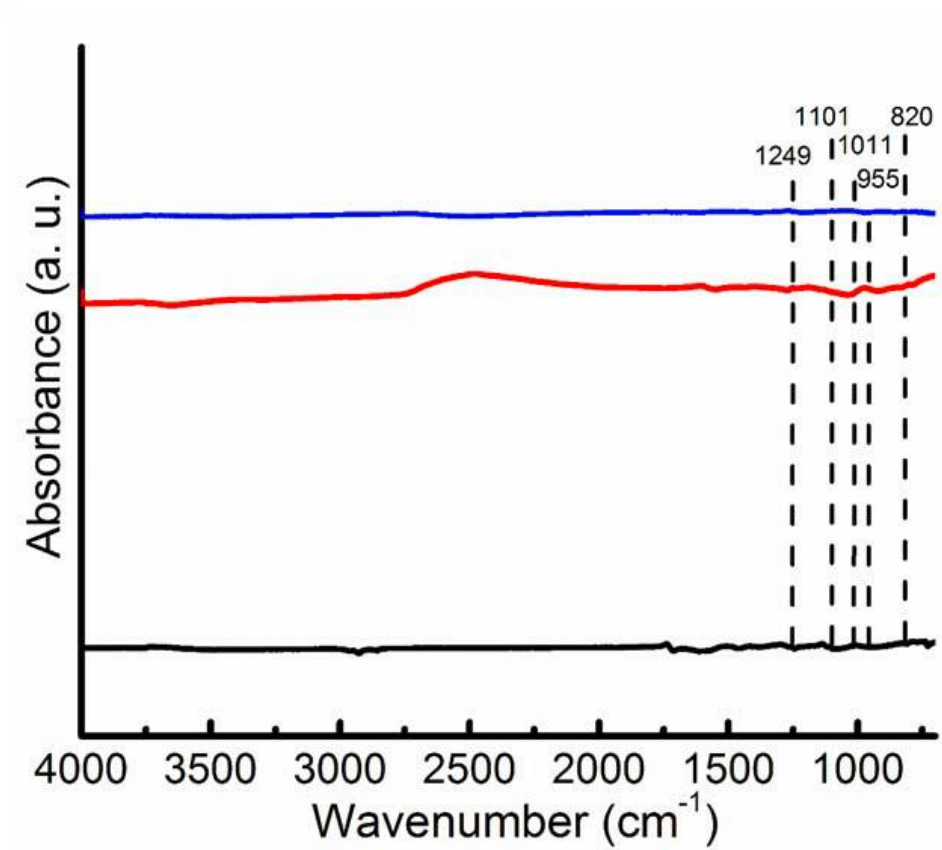


**Figure S3.** FTIR difference spectra obtained for 20 nm HfO<sub>2</sub>-capped 120 nm AlPO film, after annealing to 350 °C (black), after exposed to D<sub>2</sub>O (1.3 Torr × 60 s) (red), and after annealing to 150 °C (blue) by referencing to spectra after the previous treatment. Note: there is little to no structural change in phosphate region for the capped film due to the lack of heavy water resorption.

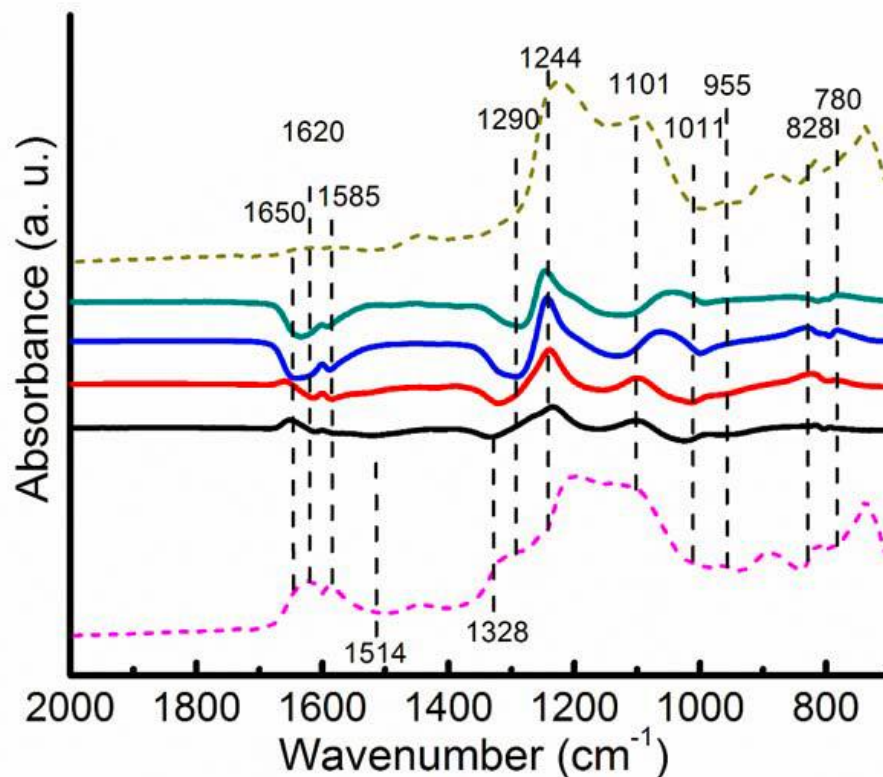


**Figure S4.** FTIR difference spectra of 82 nm AlPO<sub>4</sub>, after stepwise annealing to 350 °C referenced to spectra after the previous treatment. The absorbance spectra after 350 °C presented above is obtained by referencing the spectrum collected at 45 °C (pink dashed) after annealing to 350 °C (gold dashed) to the spectrum collected at 45 °C after annealing to 250 °C. All the spectra were recorded at 45 °C. Spectra were recorded for samples annealed to 80 (black), 150 (red), 250 (blue), and 350 °C (green). The dashed lines represent the absorbance spectra obtained for the film by referencing the spectrum of the film at 45 °C to a clean SiO<sub>2</sub> on Si (100) wafer and the film after annealing to 350 °C to a clean SiO<sub>2</sub> on Si (100) wafer at 80 °C.

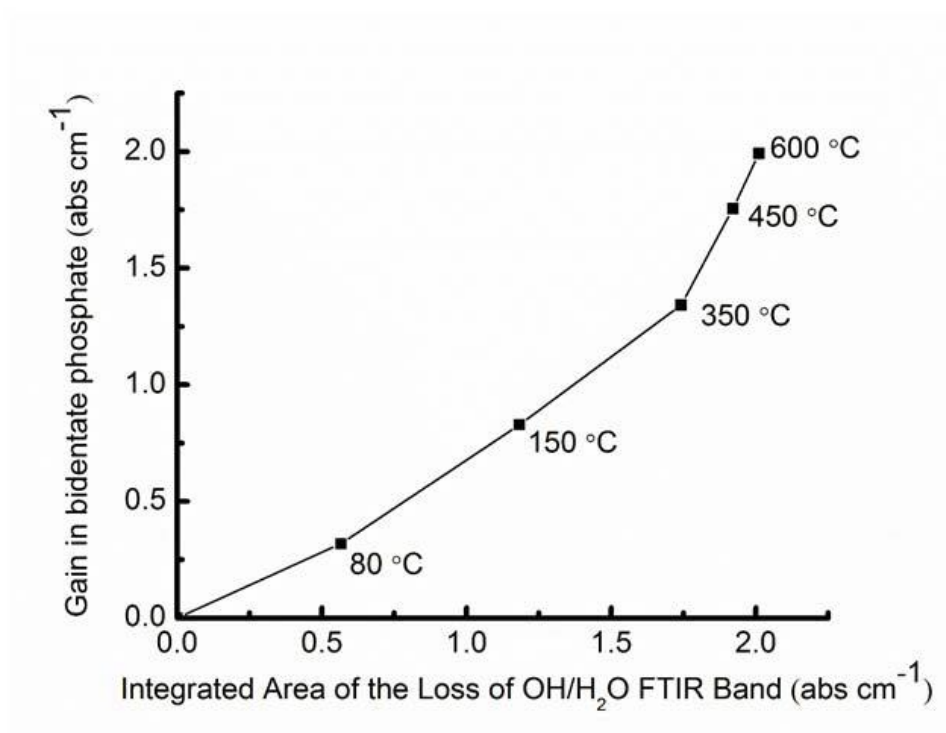


**Figure S5.** Integrated area of bidentate phosphate gain for 82 nm AlPO film as a function of integrated area of OH/H<sub>2</sub>O loss. This spectrum highlights the condensation reaction taking place upon annealing.

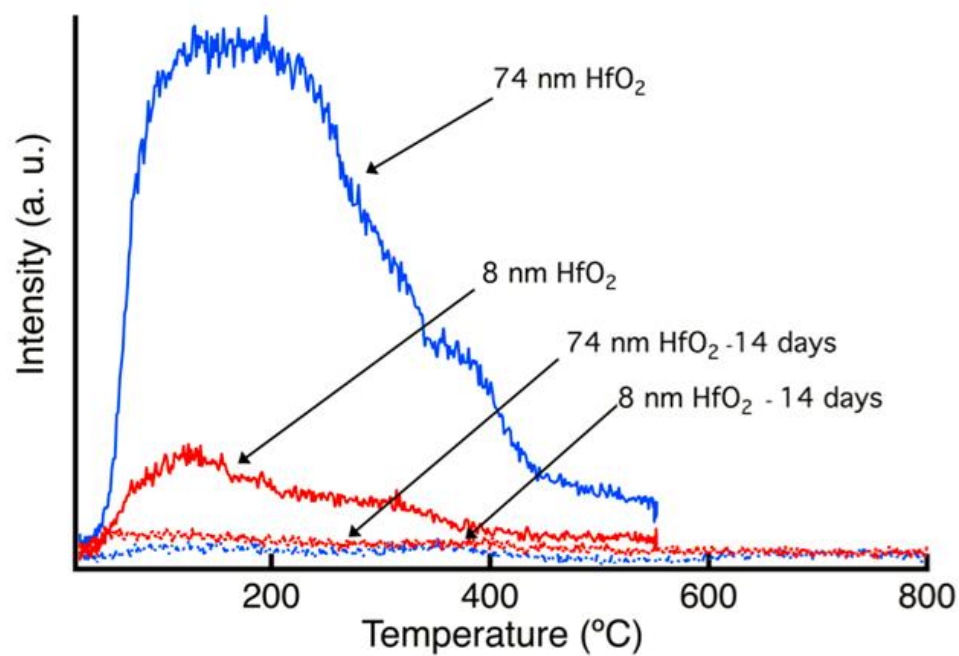


**Figure S6.** TPD spectra for HfO<sub>2</sub> control experiments. Both the thick and thin HfO<sub>2</sub> film did not show signs of resorption after the 14 day period after being heated to 550 °C.

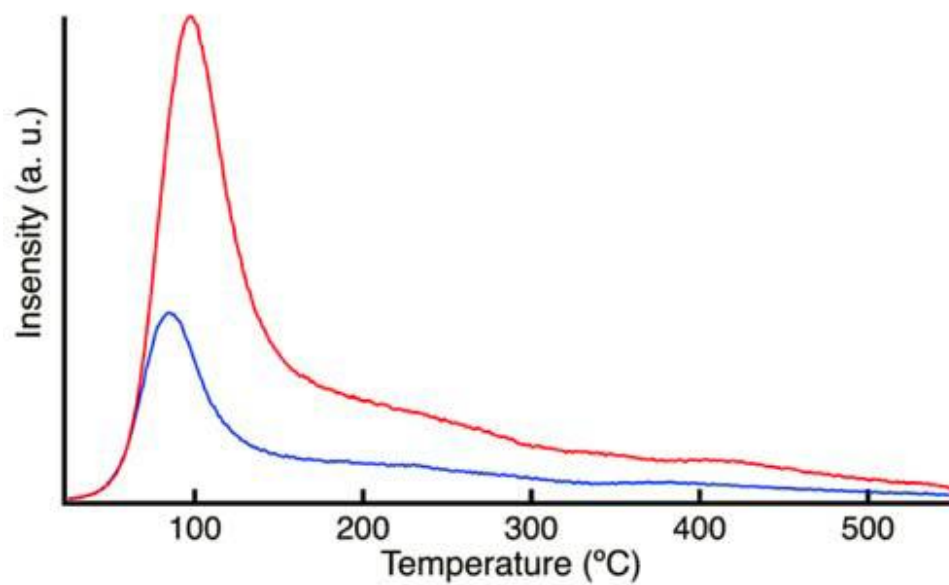


**Figure S7.** TPD data for each of the HfO<sub>2</sub>-capped AlPO films showing the shift to higher temperatures for the maximum water response signal for the 41 nm HfO<sub>2</sub>-capping layer (red) and the 10 nm HfO<sub>2</sub>-capping layer (blue). These results, with the TEM results, suggest that a thicker HfO<sub>2</sub> layer hinders the loss of water.

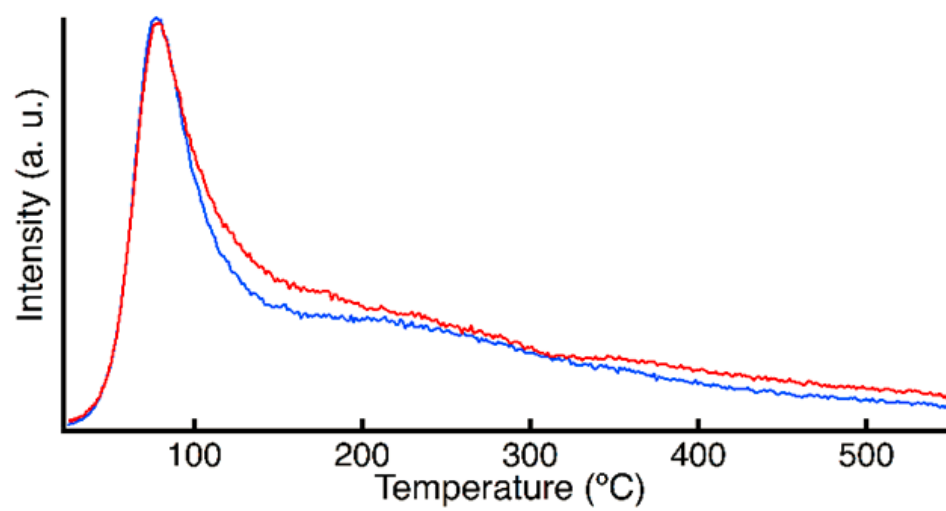


**Figure S8.** TPD data for water loss of AlPO films, 142 (red) and 141 nm (blue) thick films. Data highlight reproducibility of the TPD experiment.